Molecular Studies of Forces at Liquid-Solid Interfaces

by

Kai Huang

A dissertation submitted in partial fulfillment of
the requirement for the degree of

Doctor of Philosophy
(Materials Science and Engineering)

at the

UNIVERSITY OF WISCONSIN-MADISON

2015

Date of final oral examination: 8/17/2015

The dissertation is approved by the following members of the Final Oral Committee:

Izabela Szlufarska, Professor, Materials Science and Engineering
Dane Morgan, Professor, Materials Science and Engineering
Nicholas Abbott, Professor, Chemical and Biological Engineering
Qiang Cui, Professor, Chemistry
Michael Arnold, Associate Professor, Materials Science and Engineering

To my grandparents, parents and Jiaxi Shen

Abstract

We have combined computer simulation and theory to study the forces at liquid-solid (L-S) interfaces, including the friction and solvation forces. We first model the energy dissipation and momentum transfer at vibrating solid-water interfaces with a wide range of wettabilities. We study the effect of L-S slip/friction on the mechanical response of the resonators. A new analytical model is developed to describe mechanical response of the high frequency resonators, which is relevant in applications as biosensors. We find a linear relationship between the slip length and the ratio of the damping rate shift to resonant frequency shift, which provides a new way to obtain information about slip length from experiments. Our molecular dynamics (MD) simulations demonstrate that the slip length is dynamic and depends on frequency.

To overcome the difficulty of measuring L-S slip/friction at experimental relevant time scales, we have developed a Green-Kubo (GK) relation that enables accurate calculations of friction at L-S interfaces directly from equilibrium MD (EMD) simulations. Our GK relation provides a pathway to bypass the time scale limitations of typical non-equilibrium MD simulations. The theory has been validated for a number of different of interfaces and it is demonstrated that the liquid-solid slip is an intrinsic property of an interface. Because of the high numerical efficiency of our method, it can be used in design of interfaces for applications in aqueous environments, such as nano- and micro-fluidics.

Using our GK relation and μs-long large-scale MD simulations, we investigate the near-boundary Brownian motion, a classic hydrodynamic problem of great importance in a variety of fields, from biophysics to micro-/nanofluidics. Due to challenges in experimental measurements of near-boundary dynamics, the asymptotic behavior of the velocity autocorrelation function (VAF) of the near-boundary Brownian particle remains unclear and debated. Our computer experiment unambiguously reveals that the $t^{-3/2}$ long-time decay of the VAF of a Brownian particle in bulk liquid is replaced by a $t^{-5/2}$ decay near a boundary. We discover a general breakdown of traditional no-slip boundary condition at short time scales and we show that this breakdown has a profound impact on the near-boundary Brownian motion. Our results

demonstrate the potential of Brownian-particle based micro-/nano-sonar to probe the local wettability of liquid-solid interfaces.

Motivated by the need to understand phenomena such as hydrophobically driven self-assembly or protein folding, we have also studied the hydrophobic solvation force with a specific focus on the effects of ions. Using β-peptide-inspired nano-rods, we investigate the effects of both free ions (dissolved salts) and proximally immobilized ions on hydrophobic interactions. We find that the free ion effect is correlated with the water density fluctuation near a non-polar molecular surface, showing that such fluctuation can be an indicator of hydrophobic interactions in the case of solution additives. In the case of immobilized ion, our results demonstrate that hydrophobic interactions can be switched on and off by choosing different spatial arrangements of proximal ions on a nano-rod. For globally amphiphilic nano-rods, we find that the magnitude of the interaction can be further tuned using proximal ions with varying ionic sizes. In general, univalent proximal anions are found to weaken hydrophobic interactions. This is in contrast to the effect of free ions, which according to our simulations strengthen hydrophobic interactions. In addition, immobilized anions of increasing ionic size do not follow the same ordering (Hofmeister-like ranking) as free ions when it comes to their impact on hydrophobic interactions. We propose a molecular picture that explains the contrasting effects of immobilized versus free ions.

Published work and work in preparation

1. K. Huang and I. Szlufarska, "Friction and slip at solid/liquid interface in vibrational systems", *Langmuir* **28**, 17302 (2012)
2. K. Huang and I. Szlufarska, "Green-Kubo relation for friction at liquid-solid interfaces", *Physical Review E* **89**, 032119 (2014)
3. K. Huang and I. Szlufarska, "Effect of interfaces on nearby Brownian motion", accepted by *Nature Communications*
4. K. Huang, S. Gast, C. D. Ma, N. Abbott and I. Szlufarska, "Comparison between free and immobilized ion effects on hydrophobic interactions: a molecular dynamics study", Under review
5. K. Huang and I. Szlufarska, "Curvature dependent hydrophobic solvation: water and methanol", In preparation

Acknowledgements

I would like to acknowledge my sincere thanks to my advisor, Professor Izabela Szlufarska for introducing me to the world of computer simulation and being so supportive in my academic life. She has taught me not only how to conduct research, but also how to communicate and present. I still remember that she helped me improve my seminar talk slide-by-slide during a weekend. Without her guidance, encouragement and patience, I could not break through at the hardest time of research and would never be shaped into who I am today. During the process, I enjoyed much the freedom of research she gave me as well as the great opportunities she opened up to collaborate with experimentalists on exciting projects.

I thank Professor Dane Morgan for the giving me many great lectures during my early graduate years, covering simulation, thermodynamics and energy-related topics. Exposure to the suggestions and discussions from Dane in the group meetings is pleasant as he is always very clear and thinking about the big picture. I also would like to thank Professor Nicholas Abbott for a great collaboration on the hydrophobicity project. I have enjoyed every meeting with his group for progress reports and scientific discussions. I am impressed by his strong curiosity about scientific problems and inspirational questions/comments in an always-gentle tone.

I am thankful to Professor Qiang Cui for teaching me electronic structures and allowing me to sit in and learn molecular biophysics from his group meetings. I thank Professor Michael Arnold for taking time out of his busy schedules to serve as my dissertation committee. My acknowledge also goes to Professor Arun Yethiraj, Professor Roderic Lakes and Professor Xudong Wang, who served as my RRE committee. I was highly benefitted from the discussions I had with Professor Yethiraj and people from his group.

There are many former and current students I would like to acknowledge here as well. I especially thank Dr. Yun Liu and Dr. Maneesh Mishra who were great seniors and gave me many brainstorms and technical supports. I also learnt a lot from Dr. Kuang Yu, who was one of my best friends in Madison for four years. I had a really good time with Sebastian

Gast who was not only a great team worker but also a great friend during his one-year visit in Madison. I also thank experimentalists Dr. Derek Ma and Dr. Chenxuan Wang for sharing their experimental insights and great collaborations. Finally, I would like to thank all former and current members of the Computational Materials Group for their continuous support in my graduate study.

Contents

List of Figures

List of Tables

List of Symbols

Symbol	Meaning
σ	width of the LJ potential
ϵ	depth of energy well of LJ potential
γ	hydrodynamic friction coefficient in fluid
δ	penetration length
η	viscosity
$\bar{\eta}$	L-S friction coefficient
χ	susceptibility
ρ	density
μ	mobility
ω	angular frequency
τ	characteristic time
$C(t)$	time correlation function
D_b	bulk diffusion constant
D_w	near-boundary diffusion constant
d	thickness
E	energy
f	frequency
F_{f}	frictional force
F_{s}	solvation force
F_{R}	random force
G	free energy
h	height
k	Boltzmann constant
l	slip length
m	mass
P	pressure
$\mathbf{P}$	projector operator
r	distance
t	time
T	temperature
U	intermolecular potential
v	velocity
V	volume

Abbreviations

Abbreviation	Meaning
AFM	atomic force microscopy
CG	coarse-grained
EMD	equilibrium molecular dynamics
GA	globally amphiphilic
GK	Green-Kubo
GLE	generalized Langevin equation
HP	hydrophobic
iso-GA	non globaly amphiphilic
MD	molecular dynamcis
MEMS	microelectromechanical systems
NEMS	nanoelectromechanical systems
NEMD	non-equilibrium molecular dynamics
L-S	liquid-solid
LJ	Lennard Jones
PMF	potential of mean force
QCM	quartz crystal microbalance
RDF	radial distribution function
VAF	velocity autocorrelation function
WHAM	weighted histogram analyis method

1 Introduction and motivation

1.1 From hydrodynamics to solvation science

Liquid-solid (L-S) interfaces are common in nature and give rise to many interesting phenomena including capillarity, L-S slip, surface wettability and hydrophobic association. Understanding these interfacial phenomena is of great scientific and engineering importance. For example, biological systems typically involve abundant L-S interfaces and the properties and functionalities of such interfaces are essential for life. This fundamental role of biological L-S interfaces in living systems goes all the way down to the molecular level where proteins, the building blocks of life, cannot fold themselves without the driving force of hydrophobic interaction[1–7]. Inspired by nature, amphiphilic molecules have been synthesized to self-assemble in aqueous environment[8–12]. Super-hydrophobic materials have also been designed to make self-cleaning surfaces[13–17]. The miniaturization of devices such as micro-/nano-fluidics[18;19] has further urged the studies of L-S friction as the surface/volume ratio is unavoidably high at small length scales.

Despite its wide existence in daily life and central relevance in novel applications, there are still many open questions regarding L-S interfaces due to the challenges in calculating structure and dynamics of interfacial liquids and measuring these properties in experiments. Some of the mysteries at L-S interface have even been waiting for answers for centuries. For instance, since the early days of classic hydrodynamics, it has been debated whether there can be slip between liquid flow and its solid boundaries[20]. The boundary condition of fluid is necessary to solve the continuum-level Stokes equations. However, such a boundary condition cannot be predicted from hydrodynamic theories, but requires more fundamental molecular theories that are yet to be developed. It has been determined only in the last decade by experiment that slip can happen at L-S interfaces, which means that the classic no-slip boundary condition can break down[21;22]. However, it has remained a difficult problem for experiment to quantitatively

measure the slip. One reason is that it is challenging to directly probe the structure and dynamics of liquid molecules within nanometer distance from a surface[23]. It is also a non-trivial task for experiment to control the roughness of the L-S interface to nanometer or sub-nanometer level. Both the molecular structure and the roughness of surfaces are known to strongly impact the behavior of interfacial liquid and therefore the boundary condition for macroscopic flow. One example of such an impact is the water splash upon the entering of macroscopic solid objects into water. It has been shown that a small change of surface chemistry of the object can significantly affect the size of the water splash[24]. For small objects that perform Brownian motion in liquid, the interfacial chemistry can even determine how the object move or diffuse. For example, a Brownian particle with perfect slip boundary condition diffuses 1.5 times faster than a same sized particle with no-slip boundary condition in liquid[25].

Consider even smaller solutes down to molecular level, the knowledge of how the solutes are solvated by solvent molecules is crucial to understanding the solubility of the solutes and the properties of the solution. The so-called solvation science is a scientific branch that focuses on such questions and it has attracted increasing research interests in recent years[3;26–28]. In water, many factors contribute to the solvation energy of a solute, including the surface chemistry[29], the shape of the solute[30], and the additives such as ions[31;32] in the solution. Non-polar or hydrophobic solutes have high solvation energy in water and tend to segregate. Such hydrophobic attraction is a result of the break or rearrangement of the hydrogen bond network in water. It is well known that adding salts can modify the strength of hydrophobic interaction and such modification is ion-specific. In the seminal work of Hofmeister in 1888[33], he ranked ions based on how they change the solubility of proteins. However, since then the mechanisms beyond the Hofmeister series has been subject to intensive debate. Recent studies have suggested that the Hofmeister effect is not solely determined by the ions but also depends on their interplay with the solutes.[26;30;34] Pioneering attempts[35;36] have also been made to explore the effect of immobilized charged groups on the hydrophobic interaction of the amphiphilic molecules, as in reality molecular surfaces are often heterogeneous in polarity and charge.

The various L-S phenomena introduced above are largely governed by two forces in aqueous environments as schematically shown in Fig. 1.1. The first one is the force parallel to the L-S interface (friction force), which determines the boundary condition of fluids, leading to energy dissipation upon the sliding along the interface. The other is the solvation force that

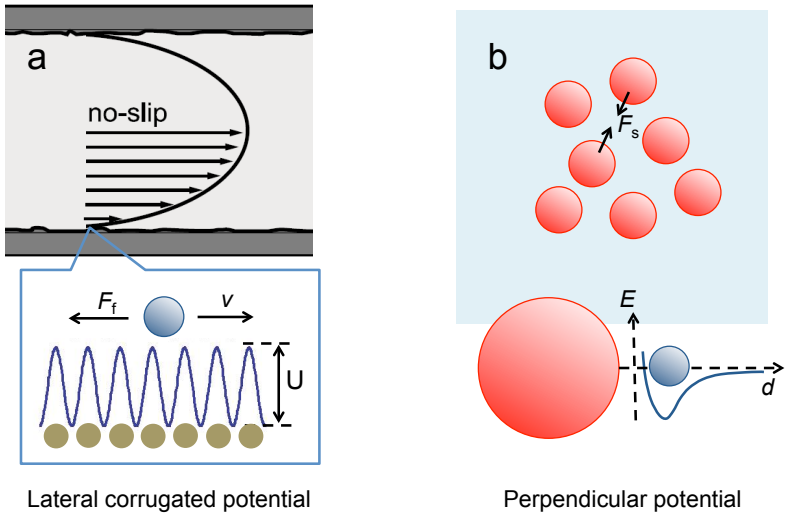

Figure 1.1: Frictional force (F_f) and solvation force (F_s) at L-S interfaces. Left: Macroscopic boundary condition and microscopic L-S friction on single solvent molecule when it is moving parallal to the surface,which has a corrugated potential. Right: solvent-mediated solvation force in solution that drive solutes to self-assemble.

yields the surface tension, driving the wetting/dewetting processes of solid surfaces, or the solvation/desolvation processes of solutes. Both forces are sensitive to the molecular details at the L-S interface. For example, the corrugated potential along the interface plays an important role in the L-S friction. On the other hand, the shape of the potential in the direction normal to the interface can greatly influence the solvation force. These simple ideas are also illustrated in Fig. 1.1.

Molecular dynamics (MD) simulation provides a powerful tool to study the molecular mechanisms underlying the L-S interfacial problems. In MD simulations, the trajectories of atoms are known with the positions and forces being accurately calculated. Correlation functions that characterize the liquid relaxations can also be extracted. With the growth of computing power, MD simulations have now become capable of dealing with some hydrodynamic problems that arise at relatively large length scales and long time scales. The upscaling of MD simulation is often futher facilitated by the coarse-graining technique, which treats groups of atoms as united entities. On the other hand, more powerful computers also allow more realistic and sophisticated force fields to be implemented to increase the accuracy of the simulations. *Ab initio* MD simulations that consider the electronic structures have also been used in recent years to study L-S phenomena. Despite the advances in computations, interfacial problems

are still in general challenging as long-range interactions, polarizations, charge transfer and chemical reactions could all play a role. That means one needs to wisely choose the force field and set up the simulation system to make the computation efficient and physically meaningful.

This thesis combines results of computer simulations and theory developments related to L-S interface. Specifically, it focuses on the molecular mechanisms of the friction and solvation forces at L-S interfaces. Mechanical models and statistical theories have been developed to understand the boundary condition of fluid and its hydrodynamic consequences. MD simulations have been employed to validate our theories and as a means for discovery of new phenomena. For the extensively studied hydrophobic interaction and specific ion effects, we aim to provide novel and complementary insights using our newly designed simulation systems.

1.2 Overview of the thesis

The remainder of the thesis is set up as follows. In Chapter 2, we talk about the methods used in this study, including simulation techniques and theoretical tools. We first briefly introduce the key ideas of the MD technique, including discussions of force fields. Then we introduce theoretical concepts such as correlation function and the Green-Kubo relations. These concepts allow us to use equilibrium MD (EMD) simulations to extract information about transport coefficients for non-equilibrium systems.

In Chapters 3, 4 and 5, we study the L-S friction and boundary condition of fluid. In Chapter 3, we first study the effect of L-S friction in shear-mode vibrating systems of application for biosensors. We show from non-equilibrium MD (NEMD) simulations that the L-S friction is dynamic, which means it depends on the frequency. In such simulations, the frequency and shear rate are much higher than those in experiments. To enable simulations to access the experimental time scales, in Chapter 4 we develop a GK relation that connects the friction coefficient to the interfacial correlation functions. Such statistical theory also provides a tool to understand the relaxation of L-S friction. Chapter 5 shows an example of how a dynamic boundary condition affects the near-by Brownian motion. Using MD simulations we show that long-time tail follows a $t^{-5/2}$ dependence, which functional form has been long debated in literature. We show how the assumption of static no-slip boundary breaks down for unsteady hydrodynamic problems, leading to a suppression of the hydrodynamic tail of near-boundary

Brownian motion.

In Chapters 6, we turn to study the solvation force and focus more on the solvation chemistry. Specifically, we study the effects of ions on the hydrophobic interactions. We compare the effects of free and immobilized ions to gain a more general understanding of Hofmeister series.

Finally in Chapter 7 we summarize our studies and briefly discuss possible future directions.

Bibliography

[1] Chandler, D, "Interfaces and the driving force of hydrophobic assembly," *NATURE*, vol. 437, pp. 640–647, SEP 29 2005.

[2] J. G. Davis, K. P. Gierszal, P. Wang, and D. Ben-Amotz, "Water structural transformation at molecular hydrophobic interfaces," *NATURE*, vol. 491, pp. 582–585, NOV 22 2012.

[3] J. G. Davis, B. M. Rankin, K. P. Gierszal, and D. Ben-Amotz, "On the cooperative formation of non-hydrogen-bonded water at molecular hydrophobic interfaces," *NATURE CHEMISTRY*, vol. 5, pp. 796–802, SEP 2013.

[4] S. N. Jamadagni, R. Godawat, and S. Garde, "Hydrophobicity of Proteins and Interfaces: Insights from Density Fluctuations," in *ANNUAL REVIEW OF CHEMICAL AND BIOMOLECULAR ENGINEERING, VOL 2* (Prausnitz, JM, ed.), vol. 2 of *Annual Review of Chemical and Biomolecular Engineering*, pp. 147–171, 2011.

[5] G. Hummer, S. Garde, A. Garcia, A. Pohorille, and L. Pratt, "An information theory model of hydrophobic interactions," *PROCEEDINGS OF THE NATIONAL ACADEMY OF SCIENCES OF THE UNITED STATES OF AMERICA*, vol. 93, pp. 8951–8955, AUG 20 1996.

[6] L. Pratt and A. Pohorille, "Hydrophobic effects and modeling of biophysical aqueous solution interfaces," *CHEMICAL REVIEWS*, vol. 102, pp. 2671–2691, AUG 2002.

[7] K. Lum, D. Chandler, and J. Weeks, "Hydrophobicity at small and large length scales," *JOURNAL OF PHYSICAL CHEMISTRY B*, vol. 103, pp. 4570–4577, JUN 3 1999.

[8] R. Cheng, S. Gellman, and W. DeGrado, "beta-peptides: From structure to function," *CHEMICAL REVIEWS*, vol. 101, pp. 3219–3232, OCT 2001.

[9] S. Vauthey, S. Santoso, H. Gong, N. Watson, and S. Zhang, "Molecular self-assembly of surfactant-like peptides to form nanotubes and nanovesicles," *PROCEEDINGS OF THE NATIONAL ACADEMY OF SCIENCES OF THE UNITED STATES OF AMERICA*, vol. 99, pp. 5355–5360, APR 16 2002.

[10] N. Seeman, "DNA in a material world," *NATURE*, vol. 421, pp. 427–431, JAN 23 2003.

[11] J. M. Slocik, F. Tam, N. J. Halas, and R. R. Naik, "Peptide-assembled optically responsive nanoparticle complexes," *NANO LETTERS*, vol. 7, pp. 1054–1058, APR 2007.

[12] Q. Chen, S. C. Bae, and S. Granick, "Directed self-assembly of a colloidal kagome lattice," *NATURE*, vol. 469, pp. 381–384, JAN 20 2011.

[13] A. Lafuma and D. Quere, "Superhydrophobic states," *NATURE MATERIALS*, vol. 2, pp. 457–460, JUL 2003.

[14] T. Sun, L. Feng, X. Gao, and L. Jiang, "Bioinspired surfaces with special wettability," *ACCOUNTS OF CHEMICAL RESEARCH*, vol. 38, pp. 644–652, AUG 2005.

[15] K. Lau, J. Bico, K. Teo, M. Chhowalla, G. Amaratunga, W. Milne, G. McKinley, and K. Gleason, "Superhydrophobic carbon nanotube forests," *NANO LETTERS*, vol. 3, pp. 1701–1705, DEC 2003.

[16] X. Feng and L. Jiang, "Design and creation of superwetting/antiwetting surfaces," *ADVANCED MATERIALS*, vol. 18, pp. 3063–3078, DEC 4 2006.

[17] A. Tuteja, W. Choi, M. Ma, J. M. Mabry, S. A. Mazzella, G. C. Rutledge, G. H. McKinley, and R. E. Cohen, "Designing superoleophobic surfaces," *SCIENCE*, vol. 318, pp. 1618–1622, DEC 7 2007.

[18] Whitesides, George M., "The origins and the future of microfluidics," *NATURE*, vol. 442, pp. 368–373, JUL 27 2006.

[19] Bocquet, Lyderic and Charlaix, Elisabeth, "Nanofluidics, from bulk to interfaces," *CHEMICAL SOCIETY REVIEWS*, vol. 39, no. 3, pp. 1073–1095, 2010.

[20] C. L. M. H. Navier, "Memoire sur les lois du mouvement des fluides," *Mémoires de l'Académie des sciences de l'Institut de France*, vol. 6, pp. 389–440, 1823.

[21] Zhu, YX and Granick, S, "Limits of the hydrodynamic no-slip boundary condition," *PHYSICAL REVIEW LETTERS*, vol. 88, MAR 11 2002.

[22] Pit, R and Hervet, H and Leger, L, "Direct experimental evidence of slip in hexadecane: Solid interfaces," *PHYSICAL REVIEW LETTERS*, vol. 85, pp. 980–983, JUL 31 2000.

[23] Neto, C and Evans, DR and Bonaccurso, E and Butt, HJ and Craig, VSJ, "Boundary slip in Newtonian liquids: a review of experimental studies," *REPORTS ON PROGRESS IN PHYSICS*, vol. 68, pp. 2859–2897, DEC 2005.

[24] C. Duez, C. Ybert, C. Clanet, and L. Bocquet, "Making a splash with water repellency," *NATURE PHYSICS*, vol. 3, pp. 180–183, MAR 2007.

[25] J. P. Boon and S. Yip, *Molecular hydrodynamics*. Dover Publications, 2013.

[26] P. Jungwirth and P. S. Cremer, "Beyond Hofmeister," *NATURE CHEMISTRY*, vol. 6, pp. 261–263, APR 2014.

[27] I. T. S. Li and G. C. Walker, "Signature of hydrophobic hydration in a single polymer," *PROCEEDINGS OF THE NATIONAL ACADEMY OF SCIENCES OF THE UNITED STATES OF AMERICA*, vol. 108, pp. 16527–16532, OCT 4 2011.

[28] K.-J. Tielrooij, J. Hunger, R. Buchner, M. Bonn, and H. J. Bakker, "Influence of Concentration and Temperature on the Dynamics of Water in the Hydrophobic Hydration Shell of Tetramethylurea," *JOURNAL OF THE AMERICAN CHEMICAL SOCIETY*, vol. 132, pp. 15671–15678, NOV 10 2010.

[29] H. Acharya, S. Vembanur, S. N. Jamadagni, and S. Garde, "Mapping hydrophobicity at the nanoscale: Applications to heterogeneous surfaces and proteins," *FARADAY DISCUSSIONS*, vol. 146, pp. 353–365, 2010.

[30] P. W. Snyder, M. R. Lockett, D. T. Moustakas, and G. M. Whitesides, "Is it the shape of the cavity, or the shape of the water in the cavity?," *EUROPEAN PHYSICAL JOURNAL-SPECIAL TOPICS*, vol. 223, pp. 853–891, APR 2014.

[31] R. Leberman and A. Soper, "Effect of high-salt concentrations on water-structure," *NATURE*, vol. 378, pp. 364–366, NOV 23 1995.

[32] A. S. Thomas and A. H. Elcock, "Molecular dynamics simulations of hydrophobic associations in aqueous salt solutions indicate a connection between water hydrogen bonding and the Hofmeister effect," *JOURNAL OF THE AMERICAN CHEMICAL SOCIETY*, vol. 129, pp. 14887–14898, DEC 5 2007.

[33] F. Hofmeister, "Concerning regularities in the protein-precipitating effects of salts and the relationship of these effects to the physiological behaviour of salts," *Arch. Exp. Pathol. Pharmakol.*, vol. 24, pp. 247–260, APR 1888.

[34] N. Schwierz, D. Horinek, and R. R. Netz, "Anionic and Cationic Hofmeister Effects on Hydrophobic and Hydrophilic Surfaces," *LANGMUIR*, vol. 29, pp. 2602–2614, FEB 26 2013.

[35] C. Acevedo-Velez, G. Andre, Y. F. Dufrene, S. H. Gellman, and N. L. Abbott, "Single-Molecule Force Spectroscopy of beta-Peptides That Display Well-Defined Three-Dimensional Chemical Patterns," *JOURNAL OF THE AMERICAN CHEMICAL SOCIETY*, vol. 133, pp. 3981–3988, MAR 23 2011.

[36] C. Ma, C. Wang, C. Acevedo-Velez, S. H. Gellman, and N. L. Abbott, "Modulation of the Strength of Hydrophobic Interactions by Proximally Immobilized Ions," *NATURE*, vol. 517, pp. 347–350, JAN 2015 2015.

2 Simulation and theoretical methods

2.1 Molecular dynamics simulations

2.1.1 Introduction to molecular dynamics simulations

The molecular dynamics (MD) technique allows simulation of the motions of atoms and molecules. In such simulations, atoms are usually treated as mass points. The movements of atoms and molecules are simulated by numerically solving the Newton's equation of motion:

$$m_i \frac{\mathrm{d}^2 \vec{r}_i}{\mathrm{d}t^2} = \vec{F}_i + \vec{F}_{\mathrm{ext}} \tag{2.1}$$

for each atom i. Here m_i is the mass of the atom, $\vec{r}_i$ is its position, $\vec{F}_i$ is the intermolecular force on atom i exerted by the surrounding atoms, and $\vec{F}_{\mathrm{ext}}$ is the external force on atom i, if any is present. In MD simulations, the atomic positions are updated at discrete times. The interval of the discrete time is called a timestep Δt. The evolution of the system can be realized by different algorithms. A commonly used one is the velocity-Verlet algorithm which implements the following two equations

$$\vec{r}_i(t + \Delta t) = \vec{r}_i(t) + \vec{v}_i(t)\Delta t + \frac{\vec{F}_i(t)}{2m_i}(\Delta t)^2, \tag{2.2}$$

$$\vec{v}_i(t + \Delta t) = \vec{v}_i(t) + \frac{\vec{F}_i(t) + \vec{F}_i(t + \Delta t)}{2m_i}\Delta t. \tag{2.3}$$

The total force $\vec{F}_i$ or the acceleration on atom i is calculated by Eq. 2.1 and it is used to update the velocity $\vec{v}_i$ of the atom. The choice of the timestep Δt is a trade-off between the expense of the calculation and the stability of the simulation. A large timestep lowers the computational cost, but could increase the risk of introducing artifacts to the simulation.

MD simulations can be valuable in providing insights into statistical problems because they do not require *a priori* assumptions employed in many analytical theories. MD is especially useful in studying liquid systems[1] where the short mean free path of particles (which is comparable to the molecular size) can post fundamental difficulties for analytical theories. Therefore, MD simulation can serve as a powerful tool to test existing theories and inspire the development of new models. On the other hand, it also bridges the molecular details to macroscopic observables of experimental interests, such as structural quantities and transport coefficients. Lastly, one can apply simulations to study the performance of materials at extreme conditions such as high temperature and pressure, which conditions may be hard to reach in experiments.

2.1.2 Types of MD simulations

There are many types of MD simulations. Based on how the forces on the molecules are obtained, MD simulations can be largely classified into two categories. The first one is the so-called *ab initio* MD simulation, in which the atomic force is computed from first principles by solving the Schrödinger equation. Such MD simulation usually does not rely on adjustable parameters. However, due to the cost of such calculation, *ab initio* MD simulations are limited to small length and time scales. Another way to calculate the intermolecular interaction is through intermolecular potentials or force fields. MD simulations based on force fields are often referred as classical MD simulations. Classical MD simulations and have access to larger length and time scales than *ab initio* methods. To combine the advantages from both *ab initio* and classical MD simulations, a hybrid method called QM/MM has been developed[2], which represents the reaction center quantum-mechanically while treating the rest of system classically.

Another classification of MD simulations is based on whether the simulation system is at equilibrium or under non-equilibrium status. Equilibrium MD (EMD) simulations are used to calculate the structural and dynamic properties of equilibrated systems, often as a function of thermodynamic variables such as temperature and pressure. Non-equilibrium MD (NEMD) simulations are useful to study the behavior of systems out of equilibrium, at either steady or non-steady states. A steady non-equilibrium state means that under a constant external perturbation, the system has evolved to a point where its properties are no longer changing with time. Simulation of such systems allows extraction of transport coefficients that describe

how a system responds to external perturbations. For example, the viscosity of liquid can be measured from NEMD simulation in which a constant shear rate is built. The external perturbation can be either introduced from surfaces or boundaries where particles interact with external momentum, or applied through adding an external term in the Hamiltonian that modifies the equation of motion of particles. Lastly, we should point out transport coefficients at the linear response regime of a system can be also calculated from EMD simulations using Green-Kubo relations. One example on this will be given in Chapter 4

2.1.3 Molecular models and force fields

The force $\vec{F}$ in classical MD simulations are derived from intermolecular potential or force field U

$$\vec{F_i} = -\vec{\nabla} U. \tag{2.4}$$

Therefore, the performance of an MD simulation strongly depends on the choice of the force field. The functional forms and parameters of the force fields are often derived from experiments or first principle calculations. The nature of molecular interactions can be generally divided into two categories: bonded and non-bonded interactions. The former potentials are functions of bonds, angles and dihedrals. The non-bonded interactions include Coulomb interaction and dispersion interaction. The Lennard-Jones (LJ) potential is one of the simplest force fields for dispersion interaction and has been widely used in liquid simulations. The common 12-6 form of LJ potential is:

$$U^{LJ}(r) = 4\varepsilon \left[\left(\frac{\sigma}{r}\right)^{12} - \left(\frac{\sigma}{r}\right)^{6} \right], \tag{2.5}$$

where σ characterizes the width of the energy well, ε the depth of energy well. This simple potential has been widely used with reduced units to study the general properties of liquids. To save computational time, the LJ interaction is often truncated at a cutoff distance. For the electrostatic interactions which decay slower with distance, such a cutoff in real space would lead to artifacts in simulations, and therefore other methods are often employed, such as Ewald summation, particle mesh and PPPM methods[3–5].

Depending on the level of molecular details, molecular models can be categorized as all-atom and coarse-grained (CG) models. In the latter, a group of atoms is united and treated as one entity, which makes the computation faster than that in the all-atom representation. Taking

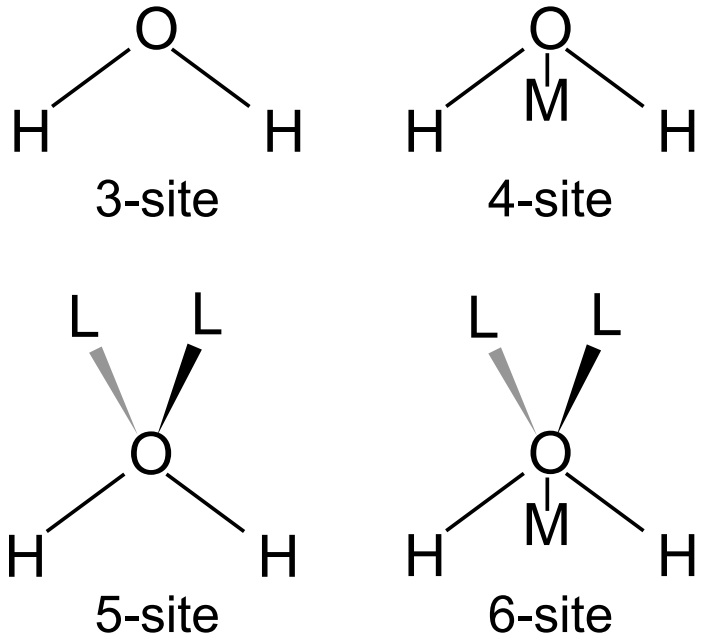

Figure 2.1: All-atom water models with different site numbers. O: oxygen atom; H: hydrogen atom; M: dummy mass; L: lone pair.

water molecule as an example, the need to simulate large solution system has demanded the development of CG water models such as the BMW model[6]. On the other hand, many all-atom models have also been developed to simulate water in situation where atomic representation is necessary. Most of these all-atom models are rigid models with the O-H bonds and H-O-H angle frozen, but they differ in how the partial charges are distributed over the molecule. For example, water models with more than 3 sites[7–9] have been developed where the partial charges are assigned to points outside of the center of mass of atoms as shown in Fig. 2.1. Specifically, negative charges may be assigned to massless dummy sites near the oxygen atom. It is worth pointing out that increasing the number of sites does not necessarily make a better water model[10] while it unavoidably increases the computational cost. Therefore the most commonly used models today are still 3-site models such as TIP3P[11] and SPC/E[12]. Early water models have fixed partial charges on each site and thus are refered as non-polarizable models. In reality, the molecular dipole of water is a variable dependent on its neighboring molecules. For this reason, recently polarizable water models have been developed and are useful in studying non-bulk water behaviors[13–15].

2.1.4 Potential of mean force and umbrella sampling

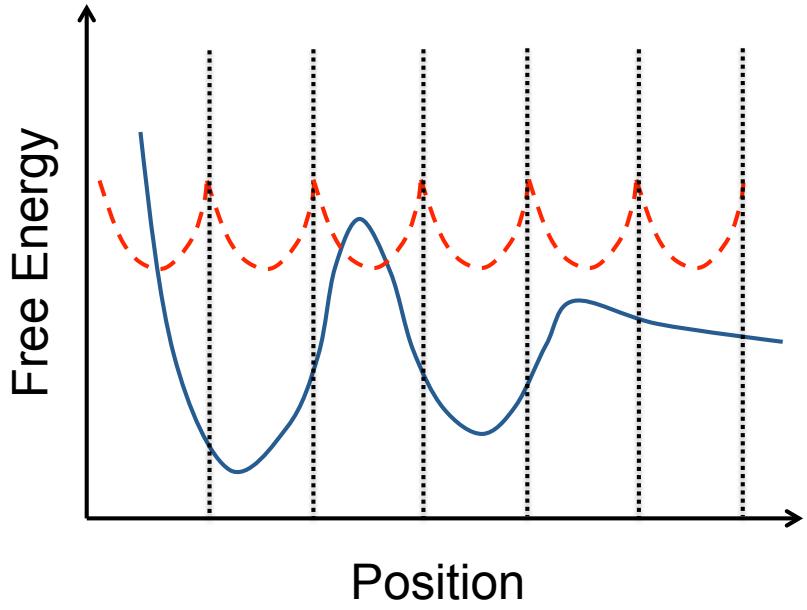

Figure 2.2: Umbrella sampling. The entire sampling region is divided into multiple windows where biasing potentials are applied. Rigid line: free energy landscape; Dashed lines: harmonic biasing potentials.

The potential of mean force (PMF) refers to the free energy of a system as a function of some reaction coordinate, such as the distance between two solutes in liquids. For a solution, this energy function includes both direct interaction between two solutes and the solvent-mediated interaction. Unlike internal energy, free energy cannot be directly calculated in simulations. There are a number of methods to extract free energy from simulations, such as free energy perturbation[16], thermodynamic integration[17], test particle insertion[18] and umbrella sampling[19]. Among these methods, umbrella sampling is commonly used when the reaction coordinates are positions. The basic idea of this method is to apply biasing potentials to improve the sampling of a system where ergodicity is hindered by energy barriers. The bias potential often takes a quadratic form and can be viewed as a harmonic constraint. The entire sampling region is divided into many small windows and for each window a separate calculation is carried out with a biasing (constraining) potential. This procedure is illustrated in Fig. 2.2 where the rigid line represents the free energy landscape with high barriers and the dashed lines are biasing potentials.

As the biasing potentials are known, the enhanced sampling, once finished, can be post-

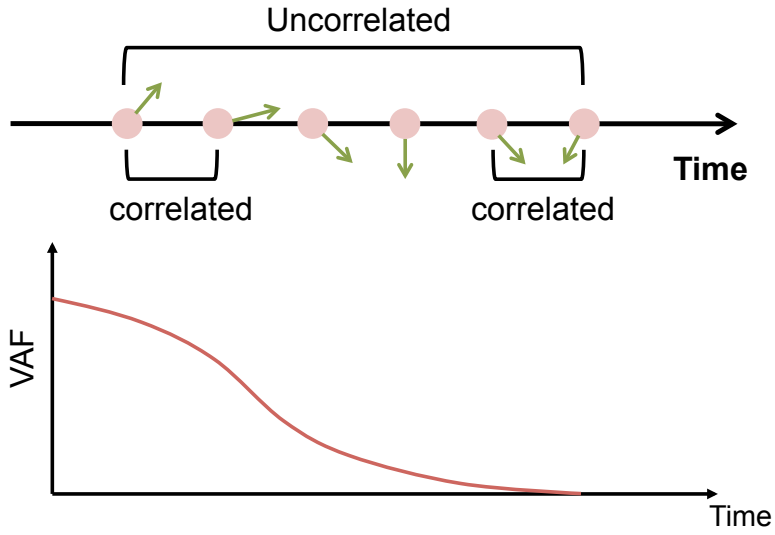

Figure 2.3: A typical velocity autocorrelation function. Arrows: velocities at different points in time.

processed to deduce the intrinsic PMF without any bias. One algorithm to do this is the Weighted Histogram Analysis Method (WHAM)[20]. The performance of PMF calculation or the accuracy of the energy landscape is closely related to the quality of the sampling. Poor sampling often happens at the overlapping region of neighboring sampling windows when the harmonic spring stiffness and the window size are not appropriately chosen. The uncertainty of the PMF can be estimated using the bootstrapping method[21] which is implemented in WHAM.

2.2 Theoretical tools

2.2.1 Correlation functions

A correlation function is a statistical correlation between random variables at two different temporal or special points. Correlation functions of two different random variables are often called cross correlation functions while the so-called autocorrelation functions measure the correlation of the same random variable. Consider the velocity autocorrelation function (VAF) $C(t) = \langle \vec{u}(0)\vec{u}(t) \rangle$ of a diffusing colloidal particle for example. As illustrated in Fig. 2.3, the particle undergoes ballistic motion at short time scales which means it keeps moving along approximately the same direction. This ballistic motion is reflected as highly correlated velocities, leading to a large value of $C(t)$ for small time t. At long time scales, $C(t)$ decays to zero as the velocity becomes uncorrelated.

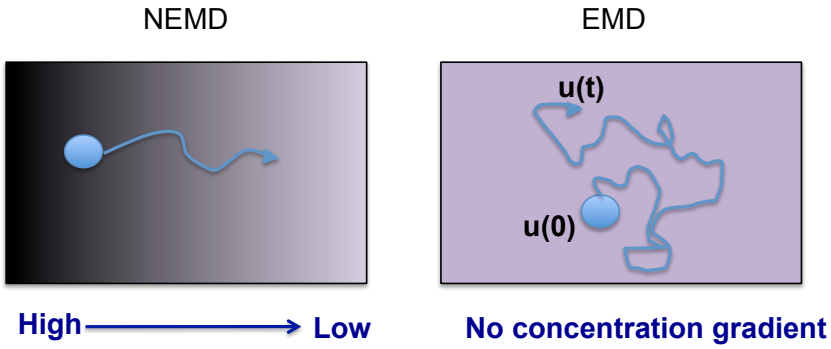

Figure 2.4: Extraction of diffusion constant using different simulation methods. Left: NEMD simulation; Right: EMD simulation.

The correlation functions provide an important language to understand the dynamics of liquids as these functions are theoretically tractable and can be measured from computer simulations and experiments (often measured as Fourier transformed spectra in frequency domain). Moreover, integrals of correlation functions are often related to the macroscopic transport coefficients through Green-Kubo (GK) relations. Such relations allow prediction of the non-equilibrium behavior of a system under an external perturbation based on the thermal fluctuations in the same system at equilibrium state. In the example of the diffusing colloidal particle, the integral of the VAF is equal to the diffusion constant D of the particle:

$$D = \frac{1}{3}\int \langle \vec{u}(0)\vec{u}(t)\rangle \mathrm{d}t. \tag{2.6}$$

As shown in Fig. 2.4, one can measure the VAF of the colloidal particle of interest in EMD simulation to calculate the diffusion constant from Eq. 2.6, instead of introducing a gradient of concentration in NEMD simulation to directly monitor the diffusion. Besides Eq. 2.6, other GK relations have also been developed for the transport coefficients including viscosity and heat conductivity[22]. All the GK relations mentioned above are limited to bulk systems. More recent interests in GK relations lie at the interfaces of phases. In Chapter 4, we develop an interfacial GK relation that connect the L-S friction to the correlation functions involving the friction and velocity of interfacial solvent molecules.

2.2.2 Brownian motion models

Brownian motion is a ubiquitous transport phenomenon in aqueous solutions. It is named after botanist Robert Brown who observed the diffusive motion of pollen grains in water under a

microscope in 1827[23]. The mechanism behind the Brownian motion was not understood until Einstein explained it in 1905 through a random walk model[24]. The model decomposes the total force on the Brownian particle into two parts, a hydrodynamic friction force F_{H} and a random force F_{R}

$$F_{\mathrm{tot}} = F_{\mathrm{H}} + F_{\mathrm{R}}, \tag{2.7}$$

where $F_{\mathrm{H}} = -6\pi\eta r u$ with η being the viscosity of the liquid and r the hydrodynamic radius of the particle, and u the particle velocity. Without the second term on the right hand side, Eq. 2.7 is just the classic Stoke hydrodynamic equation and it states that a free moving particle in liquid will slow down due to the hydrodynamic friction and eventually it will come to rest. However, this zero velocity solution for the final state of the particle violates the fact that, no matter how small, there will be a finite thermal velocity on the particle. The contribution from Einstein to this problem is the introduction of the random force, which supplies thermal energy to the particle. This random force was reasoned to be a result of the collision between the particle and surrounding individual solvent molecules. Considering both the Stokes friction and the random force, one can relate the diffusion constant of the Brownian particle D to the ratio of thermal energy and hydrodynamic friction coefficient

$$D = \frac{kT}{6\pi\eta r}. \tag{2.8}$$

This is the so-called Stokes-Einstein equation. The theoretical model was verified by experimentalist Jean Perrin in 1908[25]. Today, the Brownian motion or random walk model has been used in many fields not limited to physics, and become a powerful tool in statistics and financial analysis.

As assumed by Einstein, the random force is uncorrelated in time, that is $\langle F_{\mathrm{R}}(0)F_{\mathrm{R}}(t)\rangle = 0$ for $t \neq 0$. Therefore, based on the fluctuation-dissipation theorem, the random force satisfies the following relation

$$\langle F_{\mathrm{R}}(0)F_{\mathrm{R}}(t)\rangle = 6\pi\eta r\delta(t). \tag{2.9}$$

Based on the above assumption of random force, Einstein predicted the VAF of Brownian particle to decay exponentially with time. Thus it came as a surprise when computer simulation in the 70s discovered a slow $t^{-3/2}$ decay or the so-called long-time tail in the VAF of solvent molecules. The long-time tail was explained by the vortex flow emitted by the diffusing particle,

an inertia effect of fluid previously ignored by Stokes hydrodynamics. Inspired by the simulation result, modern Brownian motion model was developed incorporating the time-dependent hydrodynamic friction, known as the Basset force:

$$F_{\mathrm{B}}(t) = -\gamma\sqrt{\frac{\tau_f}{\pi}}\int_{-\infty}^{t}\frac{u(t')}{\sqrt{t-t'}}\mathrm{d}t'. \tag{2.10}$$

Here, $\gamma = 6\pi\eta r$ is Stokes friction coefficient and $\tau_f = r^2\rho/\eta$ is the time scale over which the vortex flow grows to the size of the particle. According to the fluctuation-dissipation theorem, a time dependent dissipation corresponds to a random force that has a non-zero autocorrelation function or a so-called memory function. This correlated random force has been captured in recent optical tweezers experiments on Brownian particles in bulk liquid. While the bulk Brownian motion theory has been widely accepted, the effect of a boundary on nearby Brownian motion is still a debated topic. In Chapter 5 we will demonstrate that the friction at L-S interface also has memory and can strongly affect the near-boundary Brownian motion.

2.2.3 Projection operator technique

The hydrodynamic theories for Brownian motion assume that the mass of the particle is extremely heavy compared to solvent molecules and are therefore not applicable to particles with comparable size to solvent molecules or solvent molecules themselves. One can ask if there is a general model that describes the diffusive motions (or Brownian motions but in a more general context) of particles in liquid regardless the particle size. The answer is positive and this general theoretical framework is called the Generalized Langevin Equation (GLE), which is widely used in non-equilibrium statistical mechanics not limited to Brownian motion[26;27]. Here, let us restrict ourselves to the case of Brownian motion and review the specific GLE equation for it. The formula of GLE for diffusion of particle i reads

$$m_i\dot{\vec{u}}_i(t) = -\int_0^t \boldsymbol{\gamma}_i(t-t')\vec{u}_i(t')\,\mathrm{d}t' + \vec{R}_i(t). \tag{2.11}$$

Here $\boldsymbol{\gamma}$ is the memory function and is related to the random force $\vec{R}$ through the generalized fluctuation-dissipation theorem

$$kT\boldsymbol{\gamma}_i(t) = \langle \vec{R}_i(0)\vec{R}_i(t)\rangle, \tag{2.12}$$

where k is the Boltzmann constant and T is the temperature. Compared to Eq. 2.9 which describes a white noise, Eq. 2.12 intrinsically deals with a correlated random force.

Another important note about the GLE is that it can be formally derived from classical mechanics. One way to do that is with the help of the projector operators:

$$\mathbf{P} = |\vec{u}_i\rangle\langle\vec{u}_i|\langle\vec{u}_i\vec{u}_i\rangle^{-1}, \tag{2.13}$$

and $\mathbf{Q} = 1 - \mathbf{P}$, where $|\vec{u}_i\rangle$ is the vector in phase space with the velocity of particle i being $\vec{u}_i$.

The time evolution operator can be decomposed using the above projection operators:

$$\mathrm{e}^{\mathrm{i}\mathbf{L}t} = \mathrm{e}^{\mathrm{i}\mathbf{Q}\mathbf{L}t} + \int_0^t \mathrm{e}^{\mathrm{i}\mathbf{L}(t-t')}\mathrm{i}\mathbf{P}\mathbf{L}\mathrm{e}^{\mathrm{i}\mathbf{Q}\mathbf{L}t'}\,\mathrm{d}t'. \tag{2.14}$$

Appling this decomposition to the acceleration of the particle $\dot{\vec{u}}_i = \mathrm{i}\mathbf{L}\vec{u}_i$, one can arrive

$$\dot{\vec{u}}_i(t) = -\frac{1}{kT}\int_0^t \vec{u}_i(t-t')\langle \mathrm{i}\mathbf{L}\vec{u}_i\mathrm{e}^{\mathrm{i}\mathrm{Q}\mathrm{L}t'}\mathrm{i}\mathbf{L}\vec{u}_i\rangle\mathrm{d}t' + \mathrm{e}^{\mathrm{i}\mathbf{Q}\mathbf{L}t}\mathrm{i}\mathbf{L}\vec{u}_i. \tag{2.15}$$

Compared to Eq. 2.11, we can see that $\vec{R}(t) = \mathrm{e}^{\mathrm{i}\mathbf{Q}\mathbf{L}t}\mathrm{i}\mathbf{L}\vec{u}_i$ is the random force, and $\boldsymbol{\gamma}(t) = \frac{1}{kT}\langle \mathrm{i}\mathbf{L}\vec{u}_i\mathrm{e}^{\mathrm{i}\mathbf{Q}\mathbf{L}t}\mathrm{i}\mathbf{L}\vec{u}_i\rangle$ is the memory function.

Bibliography

[1] M. P. Allen and D. J. Tildesley, *Computer simulation of liquids*. Oxford Science Publications, 1989.

[2] A. Warshel and M. Levitt, "Theoretical studies of enzymic reactions - dielectric, electrostatic and steric stabilization of carbonium-ion in reaction of lysozyme," *JOURNAL OF MOLECULAR BIOLOGY*, vol. 103, no. 2, pp. 227–249, 1976.

[3] P. Ewald, "PDie Berechnung optischer und elektrostatischer Gitterpotentiale," *ANNALEN DER PHYSIK*, vol. 369, pp. 10089–10092, JUN 15 1921.

[4] T. Darden, D. York, and L. Pedersen, "Particle mesh ewald - an n.log(n) method for ewald sums in large systems," *JOURNAL OF CHEMICAL PHYSICS*, vol. 98, pp. 10089–10092, JUN 15 1993.

[5] E. Pollock and J. Glosli, "Comments on P(3)M, FMM, and the Ewald method for large periodic coulombic systems," *COMPUTER PHYSICS COMMUNICATIONS*, vol. 95, pp. 93–110, JUN 1996.

[6] Z. Wu, Q. Cui, and A. Yethiraj, "A New Coarse-Grained Model for Water: The Importance of Electrostatic Interactions," *JOURNAL OF PHYSICAL CHEMISTRY B*, vol. 114, pp. 10524–10529, AUG 19 2010.

[7] J. Abascal and C. Vega, "A general purpose model for the condensed phases of water: TIP4P/2005," *JOURNAL OF CHEMICAL PHYSICS*, vol. 123, DEC 15 2005.

[8] M. Mahoney and W. Jorgensen, "A five-site model for liquid water and the reproduction of the density anomaly by rigid, nonpolarizable potential functions," *JOURNAL OF CHEMICAL PHYSICS*, vol. 112, pp. 8910–8922, MAY 22 2000.

[9] H. Nada and J. van der Eerden, "An intermolecular potential model for the simulation of ice and water near the melting point: A six-site model of H2O," *JOURNAL OF CHEMICAL PHYSICS*, vol. 118, pp. 7401–7413, APR 22 2003.

[10] C. Vega and J. L. F. Abascal, "Simulating water with rigid non-polarizable models: a general perspective," *PHYSICAL CHEMISTRY CHEMICAL PHYSICS*, vol. 13, no. 44, pp. 19663–19688, 2011.

[11] W. Jorgensen, J. Chandrasekhar, J. Madura, R. Impey, and M. Klein, "Comparison of simple potential functions for simulating liquid water," *JOURNAL OF CHEMICAL PHYSICS*, vol. 79, no. 2, pp. 926–935, 1983.

[12] H. Berendsen, J. Grigera, and T. Straatsma, "The missing term in effective pair potentials," *JOURNAL OF PHYSICAL CHEMISTRY*, vol. 91, no. 24, pp. 6269–6271, 1987.

[13] G. Lamoureux, E. Harder, I. Vorobyov, B. Roux, and A. MacKerell, "A polarizable model of water for molecular dynamics simulations of biomolecules," *CHEMICAL PHYSICS LETTERS*, vol. 418, pp. 245–249, JAN 25 2006.

[14] A. Chialvo and P. Cummings, "Engineering a simple polarizable model for the molecular simulation of water applicable over wide ranges of state conditions," *JOURNAL OF CHEMICAL PHYSICS*, vol. 105, pp. 8274–8281, NOV 8 1996.

[15] H. Yu, T. Hansson, and W. van Gunsteren, "Development of a simple, self-consistent polarizable model for liquid water," *JOURNAL OF CHEMICAL PHYSICS*, vol. 118, pp. 221–234, JAN 1 2003.

[16] Z. R, "High temperature equation of state by a perturbation method. I. nonpolar gases," *THE JOURNAL OF CHEMICAL PHYSICS*, vol. 22, no. 44, p. 1420, 1954.

[17] M. Zacharias, T. Straatsma, and J. Mccammon, "Separation-shifted scaling, a new scaling method for lennard-jones interactions in thermodynamic integration," *JOURNAL OF CHEMICAL PHYSICS*, vol. 100, pp. 9025–9031, JUN 15 1994.

[18] M. Fukuda, "Solubilities of small molecules in polyethylene evaluated by a test-particle-insertion method," *JOURNAL OF CHEMICAL PHYSICS*, vol. 112, pp. 478–486, JAN 1 2000.

[19] G. Torrie and J. Valleau, "Non-physical sampling distributions in monte-carlo free-energy estimation - umbrella sampling," *JOURNAL OF COMPUTATIONAL PHYSICS*, vol. 23, no. 2, pp. 187–199, 1977.

[20] S. Kumar, D. Bouzia, R. Swendsen, P. Kollman, and J. Rosenberg, "The weighted histogram analysis method for free-energy calculations on biomolecules .1. The method," *JOURNAL OF COMPUTATIONAL CHEMISTRY*, vol. 13, pp. 1011–1021, OCT 1992.

[21] B. Efron and R. Tibshirani, *An introduction to the bootstrap*. CRC Press, 1993.

[22] J. P. Boon and S. Yip, *Molecular hydrodynamics*. Dover Publications, 2013.

[23] Brown R., "Microscopical observations," *New Phil. J.*, vol. 5, 1828.

[24] Einstein, A., "Uber die von der molekularkinetischen Theorie der Warme geforderte Bewegung von in ruhenden Flussigkeiten suspendierten Teilchen," *Annalen der Physik*, vol. 322, no. 8, pp. 549–560, 1905.

[25] Brown R., "Discontinuous structure of matter," *Nobel Lecture*, 1926.

[26] R. Zwanzig, *Nonequilibrium Statistical Mechanics*. Oxford University Press, 2001.

[27] I. Snook, *The Langevin and Generalised Langevin Approach to the Dynamics of Atomic, Polymeric and Colloidal Systems*. ELSEVIER, 2007.

3 Friction and slip at vibrational liquid-solid interfaces

3.1 Introduction

Friction at solid/liquid interfaces plays an important role in many mechanical devices. An example is quartz crystal microbalance (QCM)[1–6], which in recent years has become a widely used mechanical method for characterization of bio-interfaces. QCM provides also a direct experimental approach to study friction[7–9] since its acoustic shear-wave motion is sensitive to the sliding friction at its surface. Such interfacial friction will result in a shift of the resonant frequency f_0 and in the case quartz crystal with dissipation monitoring (QCM-D), also in a shift of a damping rate D. f_0 and D are defined as

$$f_0 = \frac{1}{2d}\sqrt{\frac{c_q}{\rho_q}} \tag{3.1}$$

$$D = \frac{-\Delta E_n}{2E_n}, \tag{3.2}$$

where d, c_q and ρ_q are the thickness, stiffness, and density of quartz, respectively, and E_n is the mechanical energy stored in quartz during the n^{th} vibrational cycle. Solid/liquid interface is viscous in nature and the corresponding friction force can be written as

$$F = -\overline{\eta}(v_0 - u_0), \tag{3.3}$$

where $\overline{\eta}$ is the friction coefficient and v_0 and u_0 are the shear velocity of liquid and solid at the interface, respectively. The term $v_0 - u_0$ is the slip velocity, defined as the sliding velocity of the liquid adjacent to the solid relatively to the solid surface. For sufficiently large friction

coefficients, the slip velocity becomes negligible, which corresponds to the no-slip boundary condition. With no-slip boundary condition, the mechanical response of QCM can be predicted by solving continuum-level wave equations, without the need to know the value of the friction coefficient. However, the assumption of no-slip boundary condition does not always hold and therefore there is a need to develop theories that will take the existence of slip directly into account. The existence of slip has been first proposed over a century ago by Navier[10], but it has been accepted only in recent years[11–14]. Slip can be quantified either using the slip velocity $v_0 - u_0$ or the slip length l (see Fig. 3.1), where the latter quantity is defined as

$$l = (v_0 - u_0) \left(\frac{\partial v}{\partial z} \right)^{-1}. \tag{3.4}$$

The slip length is proportional to the viscosity η of liquid and to the inverse of the friction coefficient $\overline{\eta}$, that is

$$l = \frac{\eta}{\overline{\eta}}. \tag{3.5}$$

It is now accepted that the slip length can span a wide range of values, from several Angstroms (a molecular diameter scale) to micrometers for super-hydrophobic surfaces[15], and that contributions from slip to dynamics at the solid/liquid interface cannot be neglected. Large slip length is likely to occur when hydrophilic surfaces meet hydrophobic liquids or vice versa, both scenarios frequently encountered in biological systems. Slip is also expected to play an important role in resonators with high resonance frequency in the region of upper MHz (∼100 MHz) and possibly even GHz. This is because at such high frequencies the penetration length of liquid is on the micron scale and generally slip is more important when its length scale becomes comparable to the size of the system of interest. Another example of application where slip plays an important role is the microfluidics[16–19]. In this case a tiny amount of liquid flows through nano-/micro-scale pipes and friction at the pipe wall can significantly affect the flow due to the high surface/volume ratio.

Not surprisingly, understanding of the solid/liquid slip has been argued to be an important challenge in research on solid/liquid interfaces.[20–22] One of the difficulties in investigating slip at solid/liquid interfaces is that the slip length is difficult to measure experimentally. Such measurements require a very high sensitivity of the experimental apparatus to the shear stress of liquid as well as a control of the surface quality, which includes both surface roughness

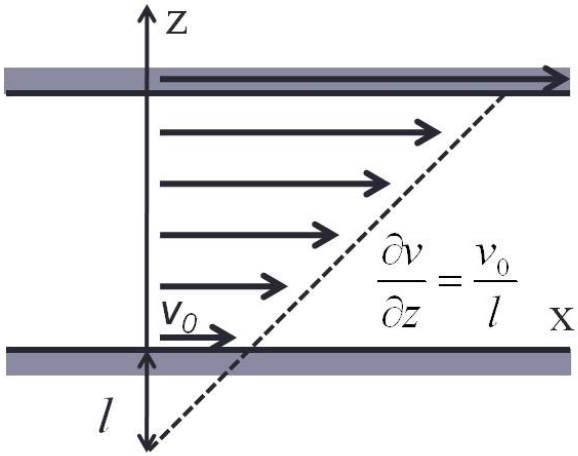

Figure 3.1: Schematic representation of the slip boundary condition with slip length l. Here, the velocity of the solid u_0=0.

and chemistry. Atomistic simulations and in particular molecular dynamics (MD) simulations, provide a powerful tool to complement experiments and to bring insights into slip-related phenomena. The MD technique enables a precise control of such factors as shear rate and vibrational frequency, and makes it possible to analyze fluid velocity gradient close to the solid/liquid interface. In addition, thanks to the ability to model atomically smooth surfaces, in MD simulations it is possible to isolate effects of surface chemistry (e.g., hydrophobicity) from effects of surface roughness. MD simulations have been already employed to determine the dependence of slip on shear rate, chemical bond strength, and surface roughness[23–33]. For example, Barrat *et al.*[23] found that the slip length of water on diamond-like solid surface scales approximately as an inverse of the square of interfacial bond strength ε between the liquid and the solid, that is:

$$l \sim \varepsilon^{-2}. \tag{3.6}$$

In other simulation studies[28;30;34], slip length has been observed to increase with shear rate $\dot{\gamma}$, consistently with the following empirical relation

$$l(\dot{\gamma}) = l_0 \left(1 - \dot{\gamma}/\dot{\gamma}_c\right)^{-0.5}, \tag{3.7}$$

where l_0 is the intrinsic slip length, which corresponds to the limit of zero shear rate, and $\dot{\gamma}_c$ is the maximum shear rate the a given liquid can carry. The aforementioned simulations of slip phenomena typically involve a sliding system in its steady state or, more specifically,

with a constant shear rate built in by confining the liquid between two parallel solid walls. The slip length measured in this way is limited to a non-vibrating (here, referred to as static) system and therefore it cannot provide any dynamic (i.e., related to vibrations) information about the solid/liquid friction. In this study we investigate the effect of slip on mechanical properties of a vibrating system, such as QCM, and therefore it is necessary to first extend the concept of a static slip (l_s) to the dynamic slip (l_d) and to discuss the relationship between these two quantities. The dynamic slip length can generally be a function of both shear rate $\dot{\gamma}$ and frequency ω, and it can be written as $l_d(\dot{\gamma}, \omega)$. In the case of a small amplitude vibration associated with a small shear rate, the dynamic slip length is approximately independent of the shear rate. In this limit, we can simplify the dynamic slip length to be $l_d(\omega)$. Later on, we will focus on the dynamic slip length in the small shear rate limit and the symbol l_d will always refer to this case. Similarly to the behavior of static slip length at low shear rate, the dynamic slip length will also converge to the intrinsic slip length l_0, which is the slip length in the limit $\dot{\gamma} \to 0$, $\omega \to 0$. The intrinsic slip length l_0 depends on the properties of the solid and the liquid and on the interfacial geometry. In our simulations, for simplicity we control the value of l_0 by modifying the bond strength ε between liquid and solid rather than by employing different types of liquid/solid combinations or different interfacial geometries. For mathematical convenience we define

$$\Gamma_s(\varepsilon, \dot{\gamma}) = l_s(\varepsilon, \dot{\gamma})/l_0(\varepsilon), \tag{3.8}$$

$$\Gamma_d(\varepsilon, \omega) = l_d(\varepsilon, \omega)/l_0(\varepsilon), \tag{3.9}$$

Γ_s (Γ_d) is the ratio between the static slip length (the dynamic slip length) and the intrinsic slip length. Γ_s (Γ_d) is expected to be equal to unity when the shear rate (frequency) is zero. As we can control the intrinsic slip length l_0 by changing the strength of interfacial bonds in simulation, we are able to investigate the influence of the slip length on the momentum transfer and energy dissipation at the solid/liquid interface with a particular focus on the transverse-shear model of a vibrating interface. We focus on a Newtonian liquid and a simple (i.e., unpatterned) solid surface, which is of relevance for most QCM applications. For a Newtonian liquid, the damping wave through the liquid can be well described using a single parameter

called penetration length[35], which is defined as

$$\delta = \sqrt{\frac{2\eta}{\omega\rho_l}}, \tag{3.10}$$

where ρ_l is the density of a liquid. The shear velocity amplitude of the damping wave along the z direction (see Fig. 3.2) can be written as $|v(z)| = |v_0|e^{-z/\delta}$, where $v_0 = |v_0|e^{i\omega t}$ is the velocity of the liquid adjacent to the solid surface. The penetration length δ describes how fast the shear wave emitted at the vibrating interface decays when it travels through the liquid. The QCM system can only sense the viscosity of liquid within a distance of a few times the penetration length from the QCM surface as the amplitude of damping wave of liquid at larger distances is low and can be ignored. The relationship between v_0 and the vibrational velocity u_0 of the solid's interface is related to the penetration length through the following equation[36]

$$v_0 = \frac{u_0}{1-(i-1)\frac{l}{\delta}}. \tag{3.11}$$

From the above expression it is clear that when the slip length l is much smaller than the penetration length δ, then $v_0 \approx u_0$, which corresponds to the no-slip boundary condition. If we define a normalized slip length $b = l/\delta$ (b_0, b_s and b_d for the intrinsic, static, and dynamic cases, respectively), we can see that boundary slip becomes important when b is not negligible as compared to 1. In our simulation, a wide range of b values can be accessed by varying the interfacial bond strength (which controls surface hydrophobicity) and the vibrational frequency (which controls the penetration length). The ability to achieve this wide span of normalized slip lengths allows us to determine relationship between QCM's mechanical response and slip. Such relationship is necessary to fully understand the effect of slip boundary condition on solid/liquid interfacial momentum transfer and energy dissipation. In subsequent sections we first review continuum level theories that are currently used to interpret QCM experiments. We begin with theories that assume no-slip boundary conditions, followed by a discussion of how slip boundary conditions have been introduced into these models. As the existing slip boundary models have not been validated in experiments nor in simulations, we will test these theories using MD simulations. We discuss what physical phenomena are not captured in the existing theories and we provide a new model that includes these phenomena.

3.2 Review of continuum-level models

The first continuum-level theory for QCM came from Sauerbrey[37], who provided the relation between the frequency shift of QCM and the mass attached to it. The Sauerbrey relation assumes that the attached mass is a thin rigid (i.e., infinitely stiff) film and therefore no energy dissipation takes place in the attached film. According to the Sauerbrey theory, the shift Δf of frequency can be related to Δm, which is the mass of the attached film per unit area, as follows:

$$\Delta f = \frac{-2f_0^2}{\sqrt{c_q \rho_q}} \Delta m. \tag{3.12}$$

In this expression f_0 stands for the resonant frequency of the unloaded system (without the attached film), and c_q and ρ_q have the same meaning as in Eq. 3.1. When QCM is placed in an aqueous environment, as often required in applications of biosensing, vibrational energy of the QCM is damped into the liquid. This damping occurs as the result of a viscous coupling, or in other words, by transmission of the shear acoustic waves across the solid/liquid interface. For a Newtonian liquid with non-slip conditions at the solid-liquid interface, one can solve the problem of wave propagation analytically to predict the change (ΔD) in the damping factor and the shift (Δf) in the natural frequency of the solid due to the presence of the liquid (referred to as liquid-loading). A mathematical formalism for this problem has been first introduced by Kanazawa and Gordon[38], who solved coupled wave-propagation and the Navier-Stokes equations. The resulting solution predicts that the resonance frequency (damping rate) of the QCM decreases (increases) due to the presence of the liquid with viscosity η and density ρ_l as:

$$\Delta f = -f_0^{3/2} \sqrt{\frac{\rho_l \eta}{\pi \rho_q c_q}}, \tag{3.13}$$

$$\Delta D = -2\pi \frac{\Delta f}{f_0}. \tag{3.14}$$

Martin *et al.*[39] considered the case of a combined loading of a thin rigid film and an infinitely deep Newtonian liquid. The authors proposed that contributions to Δf from the film and the liquid are additive. It has been later found that Martin's additive model overestimates Δf observed experimentally for the combination of a soft film and a liquid, which phenomenon has been called a "missing mass effect". The missing mass effect has been attributed to the presence of viscous coupling between the soft film and the liquid. A model that takes this physics into

account has been developed by Voinova *et al.*[40] Both, the Martin's and Voinova's models assume no-slip boundary conditions. Studies that take into account slip boundary conditions explicitly are much scarcer due to the difficulties discussed in the introduction section. Nevertheless there have been several theoretical studies aimed at incorporating the slip effect into the Kanazawa model[36;41–46]. For example, Ferrante *et al.*[41] introduced a complex interfacial slip parameter α. However, a physical meaning has not been provided for the two fitting parameters (the real and the imaginary parts of α) that appear in the model. Other theoretical approaches to slip boundary conditions include a model by Ellis *et al.*[42], who proposed a relation between the real and imaginary parts of the complex slip parameter and thereby was able to replace the complex slip parameter α with a single parameter, which is the slip length. This new model provided a clear connection between the QCM's response and the slip length and it has been invoked to explain a number of experimental results. For instance, Daikhin *et al.*[43] applied this model in the studies of adsorption of pyridine on gold surfaces and to explain the observed difference between the prediction of no-slip theory and experimental results. McHale *et al.*[44] used loading impedance to analyze similar discrepancy between experimental observations on rough surfaces and the no-slip boundary model and introduced the concept of a negative slip length to explain the discrepancy. Zhuang *et al.*[45] followed classic hydrodynamic theories to derive a mathematical formalism for the slip boundary condition and extended their model to the non-Newtonian regime in order to explain the surprising experimental observation that frequency shift Δf can be positive (no-slip models do not allow the frequency to increase in a Newtonian liquid). A mathematical analysis of a vibrational interface with slip boundary conditions and with a simplified solid (a spring attached to a solid slab) has been also reported by Persson [36]. It is straightforward to show that ignoring the roughness of the surface and the width of the interface (see discussion section), all the one-parameter slip-boundary models from Refs.[36;42–45] can be reduced to the following set of equations:

$$\frac{\Delta f}{f_0} = -\frac{1}{\pi Z}\sqrt{\frac{\rho_l \eta \omega}{2}}\frac{1}{1+2b_0+2b_0^2} \tag{3.15}$$

$$\Delta D = \frac{2}{Z}\sqrt{\frac{\rho_l \eta \omega}{2}}\frac{1+2b_0}{1+2b_0+2b_0^2} \tag{3.16}$$

where $\omega = 2\pi f$ is the angular frequency and $Z = \sqrt{c_q \rho_q}$ is the mechanical impedance of QCM. $b_0 = l_0/\delta$ is the normalized intrinsic slip length we defined in the introduction section. In the

limit of $b_0 \to 0$, Eq. 3.15 and Eq. 3.16 are reduced to the corresponding expressions in the Kanazawa model[38].

3.3 Simulation setup

All MD simulations have been performed using the LAMMPS software package[47]. In our simulations we choose water as a model liquid. We use the TIP4P model[48] for water interactions because it correctly describes mechanical properties of water, such as viscosity. Long-range electrostatic interactions are calculated using the Particle-Particle Particle-Mesh method (PPPM) method[49]. The non-bonded interactions involving hydrogen are not considered and an additional constraining force is applied to hydrogen atoms with the SHAKE[50] algorithm to enable a simulation time step as large as 4.0 fs. Because we are interested in the effects of liquid on the vibrational properties of a solid instead of materials properties of the solid itself, we choose a model solid in which atoms interact via Lenard-Jones (LJ) force field:

$$U(r) = 4\varepsilon \left[\left(\frac{\sigma}{r}\right)^{12} - \left(\frac{\sigma}{r}\right)^{6} \right]. \tag{3.17}$$

Table 3.1: Parameters of the Lennard-Jones potential. * symbol refers to all atom types other than H

Atom types	ε (kcal/mol)	σ(Å)
H-*	0.0	0.0
O-O	0.16275	3.16435
O-solid	0.05-1.0	2.8
solid-solid	8.0	3.368

Parameters ε and σ for the LJ force field used in our simulations can be found in Tab. 6.1. The cut-off for interactions is taken to be 12 Å. The solid has face-centered-cubic (fcc) structure with the (100) surface being in contact with the liquid. The value of $\varepsilon = 8.0$ kcal/mol is sufficient to make the solid sufficiently rigid in our simulations. The properties of the solid wall could affect the slip at the solid/liquid interface[29;51]. We choose the flexible wall model (solid atoms are allowed to vibrate) over the rigid wall model (solid atoms are held at their lattice sites). However, in our case the difference in the slip between the two wall models, if any such difference exists, is not expected to be large, since the atomic mass of our solid is about 2 orders

of magnitude larger than the molecular mass of water and therefore the vibrational amplitude of atoms in the solid is significantly smaller than of the liquid molecules. Heavy solid atoms are required to make the resonator in our simulation computationally inexpensive and stable during high frequency vibration. The control of interfacial bond strength is realized by choosing the value of ε for the oxygen-solid interaction. For no-slip boundary condition simulations, the value of ε is chosen to be 1.0 kcal/mol, which is strong enough to eliminate the slip velocity between solid and liquid. For slip boundary condition simulations, the value of ε changes from 0.05 to 0.6 kcal/mol, which presents a wide range of slip lengths that are typically found in simple solid/liquid interfaces. We choose the x axis to coincide with the direction of shear velocity and the gradient of velocity to lie along the z axis. Nose-Hover thermostat is coupled to the y and z components of the velocity so that the vibrational mechanical energy in x direction is not affected by the thermostat. We have confirmed that this method of temperature control leads to an exponential decay of the amplitude of free oscillations with time, as expected from theory. We have also performed simulations without any thermostat in the liquid (thermostat is only coupled to atoms in the solid), similarly as was done in MD simulations of the Couette flow reported in Refs.[52;53]. We found that the main effect of removing the thermostat from the liquid region is a decrease in water viscosity by about 10% and that this procedure does not affect the slip length and the slip model we propose in subsequent sections. For consistency, all results presented in this paper have been obtained using 2D thermostat applied to both the solid and the liquid regions. In our simulations the system is first relaxed at 300K and 1 atmosphere using NPT ensemble with coupling constants τ_T=100 fs for temperature and τ_p=1000 fs for pressure. Simulations of QCM vibrations are performed in NVT ensemble.

We perform three types of MD simulations. Measurement of water viscosity is carried out using the Reversed Non-Equilibrium Molecular Dynamics (RNEMD) method[54;55]. The RNEMD method constrains the velocity of water molecules to achieve a steady state shear rate through the thickness of the liquid. The second simulation type involves a static shearing system to measure the static slip length directly based on Eq. 3.4. In this setup two parallel solid slabs slide with respect to each other to produce a velocity gradient through the liquid confined between the two slabs. Each of the two solid slabs has dimension of 32Å×32Å×8Å (288 atoms) and the slabs are placed in a simulation box with dimensions of 32Å×32Å×81Å. There are 2000 water molecules placed between the solids, which corresponds to the water thickness of 63Å. This thickness is large enough to avoid nano-scale confinement effects reported in

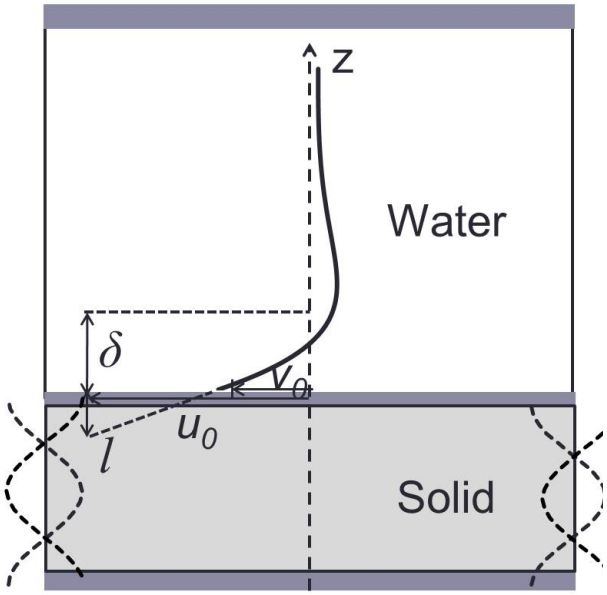

Figure 3.2: Illustration of the acoustic shear wave simulation system with slip length l. u_0 and v_0 are the velocities of solid and liquid at the interface, respectively. δ is the penetration length of water, which characterizes the damping wave.

literature[56]. The third type of simulation involves modeling a vibrational system and measuring its mechanical response to applied force, such as frequency shift and damping rate shift. In this system a thicker box of water is placed above a vibrating solid. One-atom thick solid wall is placed above the water to prevent it from evaporating. The water region has dimensions of 32Å×32Å×251Å and contains 8000 water molecules. The corresponding water density is 0.99 g/cm^3. Furthermore, we have considered two types of vibrational systems. The first one is a shear-wave QCM resonator (see Fig. 3.2). We impose acoustic shear wave by initially deforming the resonator using a cosine wave function through the thickness of the QCM (along the z direction) and then removing the constraint and allowing free oscillation of the system. This acoustic shear wave in the QCM resonator forms a standing wave while in the liquid it becomes a damping wave with the source at the solid/liquid interface. The shear modulus of the solid crystal in our simulation is 32.2 GPa. With this system setup we can only study vibrational frequencies above 30 GHz. In order to study a wider frequency range, we simplify the QCM model to a spring model, in which a solid slab is attached to a spring (each atom is constrained with a spring force that pulls it to its initial position), since it enables a shorter computational time for the same vibrational period. Although the properties of water above the vibrating solids are the same for the two types of motions, the mathematical descriptions of

the mechanical response of the two resonators are different. In Tab. 3.2, we provide expressions for the equivalent properties in the shear wave and the spring models, which properties include impendence Z, resonant frequency f_0, relative change in the frequency $\Delta f/f_0$ in the presence of liquid, and damping shift ΔD due to the presence of liquid.

Table 3.2: Mechanical properties of the two types of resonators discussed in the text. Z is impendence (units of $\mathrm{N}\cdot\ \mathrm{kg}\cdot\ \mathrm{m}^{-5})^{0.5}$), f_0 is resonant frequency, Δf is frequency shift, ΔD is damping rate, c_q is shear modulus of quartz, ρ_q is density of quartz, η_l is viscosity of liquid, ρ_l is density of liquid, k is spring constant per unit, M is mass of solid per unit, and ω is angular frequency

Shear wave model	Spring model
$Z=\sqrt{c_q\rho_q}$	$Z=\sqrt{kM}$
$f_0=\frac{1}{2d}\sqrt{\frac{c_q}{\rho_q}}$	$f_0=\frac{1}{2\pi}\sqrt{\frac{k}{M}}$
$\frac{\Delta f}{f_0}=-\frac{1}{\pi Z}\sqrt{\frac{\rho_l\eta_l\omega}{2}}$	$\frac{\Delta f}{f_0}=-\frac{1}{2Z}\sqrt{\frac{\rho_l\eta_l\omega}{2}}$
$\Delta D=-2\pi\frac{\Delta f}{f_0}$	$\Delta D=-2\pi\frac{\Delta f}{f_0}$

In the spring model, we control the spring constant k and atomic mass M per unit area, and thereby we vary the resonant frequency while keeping the mechanical impedance Z constant and equal to 4.93×10^7 $(\mathrm{N}\cdot\ \mathrm{kg}\cdot\ \mathrm{m}^{-5})^{0.5}$. The frequency in our simulations varies from 4.07 GHz to 65.1 GHz (the shortest period about 15 ps is still 3 orders of magnitude longer than the 4.0 fs time step). The typical resonant frequency of QCM in experiment is on the order of 10 MHz, and the highest frequency of acoustic shear wave devices can currently reach 1GHz, which is on the same order of magnitude as the lower end of frequency range attained in our simulations. The thickness of water in the vibrating system is 251Å and it is much larger than the penetration lengths δ, which is found to range from 15Å to 76Å. The simulation therefore provide a good approximation of an infinitely thick liquid, since the QCM can only sense the liquid within a distance from its surface equal to a few times the penetration length (see the introduction section). The penetration length is measured by computing and analyzing the vibrational amplitude along the direction of wave propagation. In our study we will first demonstrate that both, the QCM shear-wave model and the spring solid model, capture correctly behavior of resonators in the limit of no-slip. We will then use the spring solid model to investigate and provide insights into the slip behavior.

3.4 Results

3.4.1 No-slip interface

Mechanical response of QCM with a simple loading (e.g., rigid thin film) and a no-slip boundary condition has been studied extensively. The corresponding continuum-level theories summarized in the review section have been verified by experiments. Before investigating the effect of slip on mechanical properties of a QCM resonator, we first need to show that our MD model of QCM reproduces the correct mechanical behavior with the no-slip boundary condition. The non-loaded damping rate D_0 is about 0.001. Separate sets of simulations are performed for loading QCM with a rigid thin film (where we measure the resulting change Δf in resonant frequency) and for loading QCM with water (where we measure the change ΔD in the damping rate). We control the rigid loading by attaching different numbers of atoms to the QCM surface or by modifying the atomic mass of the attachment. The two approaches yield consistent results. In the liquid loading test, we vary the crystal thickness to induce different resonant frequencies. The results of tests performed for a rigid film loading and a liquid loading are shown in Fig. 3.3(a) and (b), respectively. An excellent agreement is found between our MD simulations and the Sauerbrey relation (Eq. 3.12) and Kanazawa model (Eq. 3.14), for the two types of loadings, respectively. Similarly good agreement was found for the simple spring model as shown in Fig. 3.4. In summary, both the shear-wave model and the spring model capture correctly the behavior of resonators in the limit of no-slip boundary conditions. The results of the simulations agree with the Sauerbrey and Kanazawa relations for dry and aqueous conditions, respectively.

3.4.2 Static slip interface

The next step towards the development of a model with a dynamic slip is to measure the intrinsic slip length l_0 defined in Eq. 3.9. l_0 does not depend on frequency and can be regarded as the dynamic slip length in the limit of zero frequency. However, because simulations with low frequencies are computationally too expensive, we measure l_0 using Eq. 3.8, that is in the static slip simulations in the limit of shear rate approaching zero. In our approach we use different sliding velocities to determine the static slip lengths l_s as a function of shear rate $\dot{\gamma}$ and we estimate l_0 by extrapolating l_s to the limit of $\dot{\gamma} \to 0$ using Eq. 3.7. In Fig. 3.5 (a),

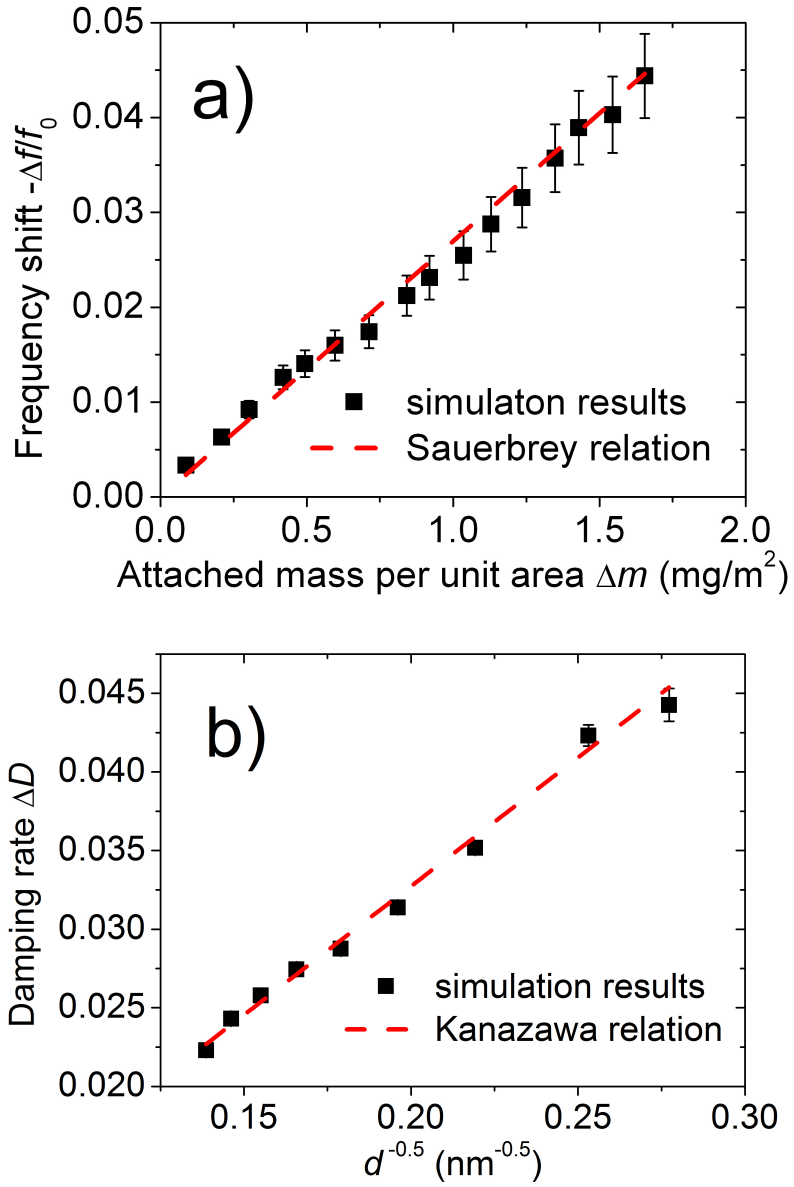

Figure 3.3: Test of QCM model with no-slip boundary condition. a) Simulation results of rigid solid loading (squares) compared to Sauerbrey's prediction (dashed line see Eq. 3.12); b) Simulation results of water loading (squares) compared to Kanazawa's prediction (dashed line see Eq. 3.14)

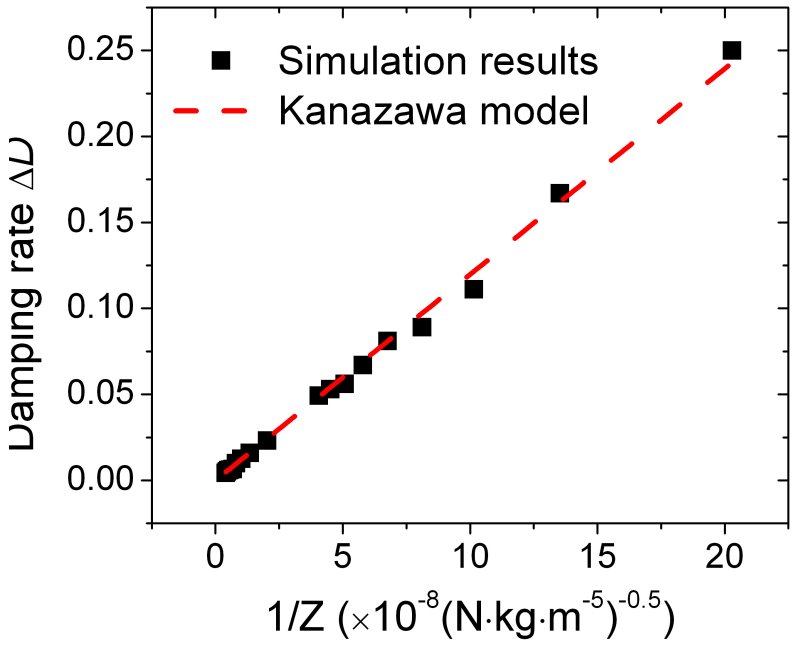

Figure 3.4: Test of spring model with no-slip boundary condition. Simulation results of water loading (squares) compared to Kanazawa's prediction (dashed line see Eq. 3.14, $Z = \sqrt{c_q \rho_q}$)

we show the plot of l_s as a function of $\dot{\gamma}$ for the case of bond strength $\varepsilon_{int} = 0.2$ kcal/mol. Data obtained from MD simulations is well approximated by the empirical relationship given in Eq. 3.7. This relationship is used to find the intrinsic slip length l_0 for different bond strengths ε_{int}, as shown in Fig. 3.5 (b). We find that the dependence of l_0 on ε_{int} is approximately exponential for $\varepsilon_{int} < 0.35$ kcal/mol (solid line in Fig. 3.5 (b)). The empirical relationship given by Barrat *et al.*[23] (Eq. 3.6) provides a good fit to the data for $\varepsilon_{int} > 0.2$ kcal/mol (dashed line in Fig. 3.5 (b)).

3.4.3 Dynamic slip interface

As pointed out in the review section, the slip length that enters existing continuum-level slip models is treated as a single real number and no frequency dependency is considered. This treatment implicitly assumes that intrinsic slip length can be used in the dynamic friction problem on the vibrating solid/liquid interface with small amplitude, as described in Eq. 3.15 and Eq. 3.16. We test this assumption in our MD simulations by measuring the QCM's mechanical response as a function of the intrinsic slip lengths at different frequencies, and comparing to the prediction of Eq. 3.15 and Eq. 3.16. All simulations are performed using the spring model

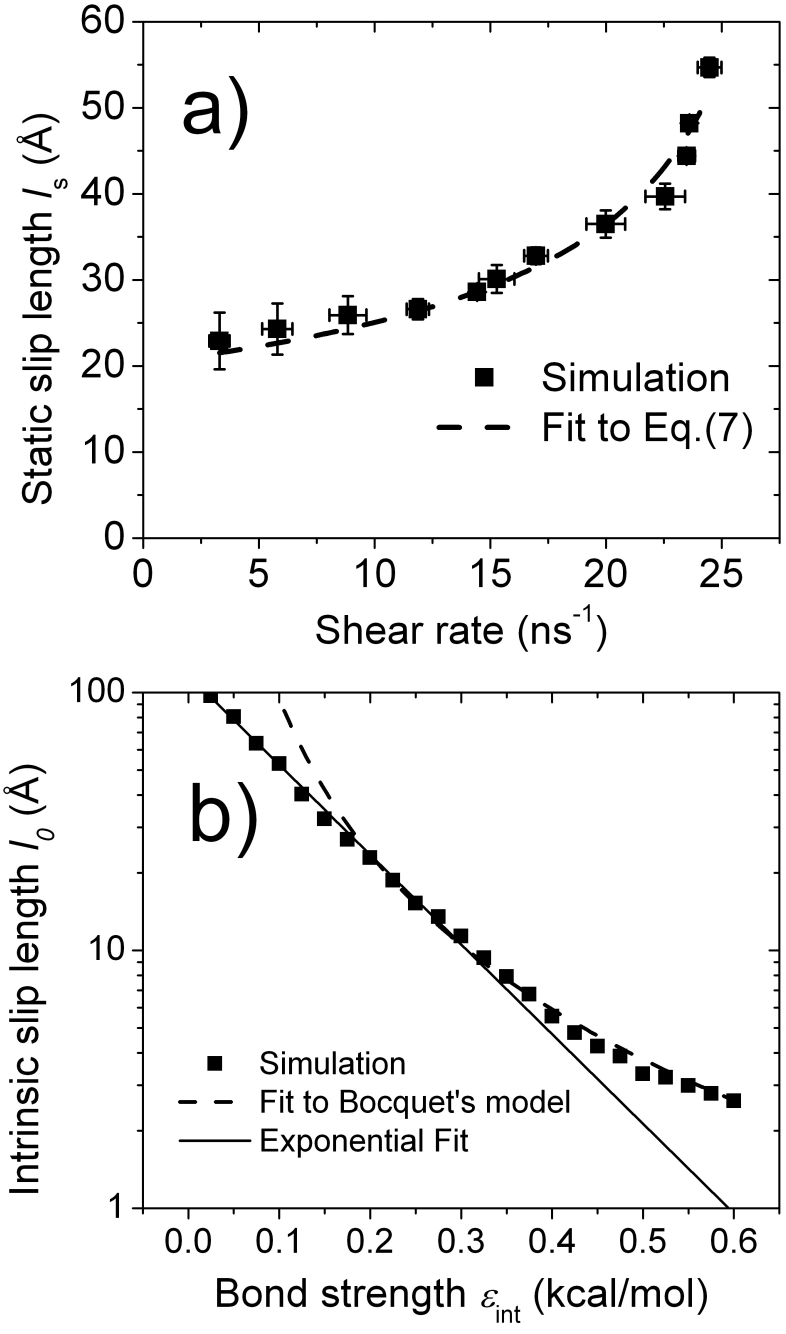

Figure 3.5: Static slip length measured from simulations. a) Static slip length of 0.2 kcal/mol bond strength at different shear rates, fitted to Eq. 3.7. b) Static slip length as a function of bond strength. Squares correspond to the estimated intrinsic slip lengths.

of QCM as the source of the resonance. As shown in Fig. 3.6, the theoretical predictions for both frequency shifts and damping rate shifts (dashed lines) significantly overestimate the corresponding quantities measured directly in MD simulations (symbols).

Our goal here is to identify the physical phenomena that underlie the observed deviations in the dependence of frequency shift and damping rate on slip length (Fig. 3.6) and to develop a theory that includes these phenomena. We hypothesize the following reasons for the breakdown of the existing theories when applied to high-frequency resonators: a) viscosity of water depends on frequency; b) slip length depends on frequency; c) inertia of the liquid layer near the interface has a non-negligible contribution to friction force. These hypotheses are tested and discussed in the remainder of this section.

We first consider the viscosity of water and determine if the assumption that the viscosity is a real constant number holds at high frequency. Based on continuum fluid mechanics, the liquid viscosity is generally dependent on shear rate and vibrational frequency. Taking the frequency dependence explicitly into account, the viscosity can be written as $\eta(\omega) = \eta'(\omega) - i\eta''(\omega)$. For a Newtonian liquid, $\eta'(\omega) \gg \eta''(\omega)$, from which it follows that the velocity profile of the damping wave can be described as[35]

$$v(z) = v_0 e^{\frac{-1-i}{\delta}z}, \tag{3.18}$$

where v is the shear velocity and δ is the penetration length defined in Eq. 3.10. By analyzing the velocity profile of the water damping wave in our simulations, we found that Eq. 3.18 describes the amplitude and the phase of the damping wave very well. This finding implies that the imaginary part of viscosity $\eta''(\omega)$ can be ignored and we can calculate the viscosity based on the measurement of the penetration length at different frequencies, using Eq. 3.10 (see the supporting information). The same equation can be used to determine viscosity as a function of shear rate (if δ is measured as a function of $\dot{\gamma}$). The dependence of viscosity on both the vibrational frequency and the shear rate is shown in Fig. 3.7a. We can see that the viscosity decreases at high frequencies and/or high shear rates and it converges to $\sim 7.3 \times 10^{-7}$ m^2/s in the low frequency (or low shear rate) limit. It is interesting to point out that our data is consistent with the empirical Cox-Merz rule, which states that $\eta(\dot{\gamma}) \approx |\eta(\omega)|$, if $\dot{\gamma} = \omega$. In summary, the water viscosity observed in our high frequency simulation can be treated as a real number, which decreases with increasing frequency, although not very strongly (it remains on the same order of magnitude). Because of this dependence on frequency, in our analysis we

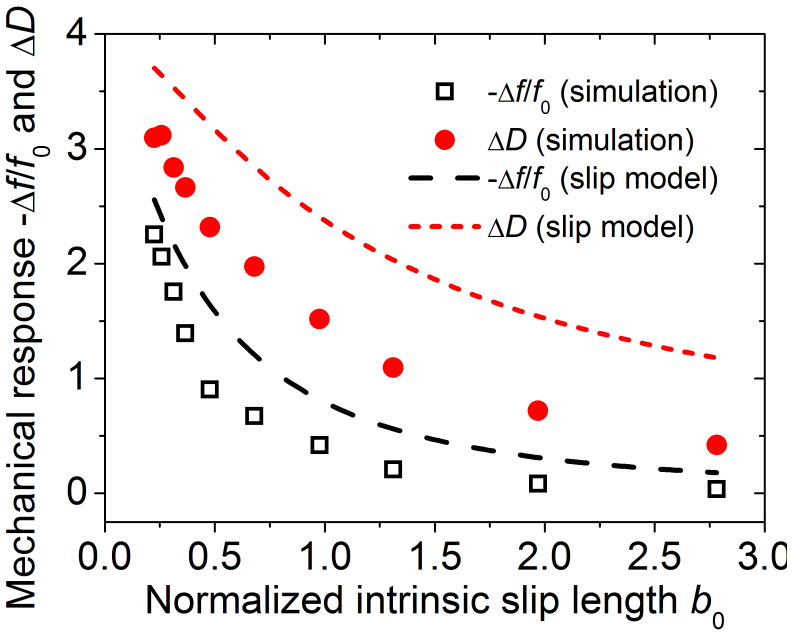

Figure 3.6: Comparison between existing models and MD results. Predictions from continuum-level slip models are given by Eq. 3.15 and Eq. 3.16.

will use $\eta(\omega)$ as measured directly in our simulations instead of using the value estimated in the low-frequency limit.

The second assumption that may break down at high vibrational frequencies is that the slip length is independent of frequency. We test this assumption by calculating the ratio between the dynamic and the intrinsic slip lengths and comparing it to 1. While the intrinsic slip length l_0 can be directly measured in simulations (see Fig. 3.5 (b)), the dynamic slip length l_d cannot be measured directly. Instead, we measure the slip velocity $u_0 - v_0$ and the velocity of the liquid adjacent to the solid surface v_0. According to Eq. 3.11, the normalized dynamic slip length can be related to these two velocities as follows

$$b_d = \frac{|u_0 - v_0|}{\sqrt{2}|v_0|}. \tag{3.19}$$

With this model, we can determine the normalized dynamic slip length indirectly by measuring the right hand side of Eq. 3.19. The limits of applicability of Eq. 3.19 will be discussed later. If the dynamic slip length is independent of frequency, the ratio Γ_d defined in Eq. 3.9 should be equal to 1. In Fig. 3.7 (b) we plot Γ_d measured as a function of bond strengths for different vibrational frequencies. The ratio Γ_d increases with increasing frequency and for the lowest frequency considered in our study (16.3 GHz) it is approximately equal to 1.5

(averaged over systems with different bond strengths). This result demonstrates that the intrinsic slip length needs to be replaced by a frequency dependent dynamic slip length to reproduce the correct physics in models of high-frequency resonators. Finally, we consider the effect of the inertia of the first water layer on the solid surface on mechanical properties of QCM. In particular, it is possible that the inertia of the first water layer can noticeably contribute to the momentum/energy transfer at the liquid/solid interface at high frequency. The equation of motion of the first water layer can be written as follow:

$$\overline{\eta}(u_0 - v_a) = -\eta \frac{\partial v}{\partial z}\Big|_{z=0} + n_a m \frac{\partial v_a}{\partial t}, \tag{3.20}$$

where m is the mass of a single water molecule, n_a is the surface number density of the first layer of water, and v_a is the averaged velocity of first layer of water. The contribution from the first water layer to the mechanical response of the QCM is described by the second term on the right hand side of Eq. 3.20. This term scales linearly with both the surface number density n_a and the frequency. In our static sliding system, as there is no acceleration, the second term on the right hand side of Eq. 3.20 is rigorously equal to zero. In order to determine n_a, we count the number of water molecules in the first layer, where the extent of this layer is determined from a density profile shown in Fig. 3.7 (c). To make the units consistent with the slip length and the penetration length, we introduce an inertia length l_a and a normalized inertia length, which are, respectively, defined as

$$l_a = n_a/n, \tag{3.21}$$

$$a(\omega) = l_a/\delta(\omega). \tag{3.22}$$

In the above equations, n is the number density of bulk water molecules and by writing $a(\omega)$ we explicitly indicate that inertia length depends on frequency. We find from simulations that $l_a \sim 4$Å and that this value is not sensitive to the bond strength. Specifically, in our simulations changing the bond strength does not affect the position of the first peak in water density profile, but it affects the height and width of the peak (more hydrophilic surfaces have a higher and a narrower peak). The velocity amplitude $|v_a|$ of the first water layer is expected to be smaller than the velocity amplitude $|u_0|$ of the solid and larger than the velocity amplitude $|v_0|$ of the next water layer in the bulk liquid. As we did not observe any jump in the shear

velocity of water, we assume $v_a \approx v_0$. Although this assumption is not as intuitive as $v_a \approx u_0$, which means a rigid adsorption, it is applicable for a wider range of interfacial bond strengths. For strong bonding (hydrophilic surfaces), $v_a \approx v_0 \approx u_0$, since the slip length and therefore the slip velocity $(u_0 - v_0)$ are small. However, for weaker bonding (hydrophobic surfaces), the liquid-liquid attraction is larger than the liquid-solid attraction, making v_a closer to v_0. Therefore, $v_a \approx v_0$ is a good approximation for all the bond strengths. The inertia term in Eq. 3.20 can be regarded as an additional friction force on the surface, whose contributions to the total friction scales with a. The value of a increases with frequency. The largest a found in our simulations is about 0.27, and it cannot be ignored in the analysis. We have modified the relationship between the dynamic slip velocity and the slip velocity (Eq. 3.19) to include the inertia effect of the first water layer. The new relationship has the following form (details in supporting information)

$$b_d = \frac{1}{\sqrt{2 + 4a + 4a^2}} \left| \frac{u_0 - v_0}{v_0} \right|. \tag{3.23}$$

We will later use Eq. 3.23 to estimate the dynamic slip length in our simulations.

In summary, we found three physical phenomena that have not been included in existing models for mechanical dissipation of resonators and that are important at high frequencies. These are: viscosity of liquid depends on frequency, slip length depends on frequency, and inertia of the first layer of liquid contributes to the friction force. We now propose a new model that takes these phenomena into account. We begin by writing the equation of motion for a spring-model of a solid vibrating along the x direction

$$M\omega^2 x = M\omega_0^2 x + F_f, \tag{3.24}$$

where F_f is the friction force (equal to the left hand side of Eq. 3.20), x is the displacement of the solid, and M is the mass of the solid. ω_0 is the resonance frequency without friction and ω is the new frequency with friction. By solving the above equation for ω and defining $\Delta\omega = \omega - \omega_0$, we obtain

$$\Delta\omega = \omega - \omega_0 = \frac{F_f}{2M\omega_0 x}. \tag{3.25}$$

The frequency shift Δf and the damping rate shift ΔD can be calculated as the real and

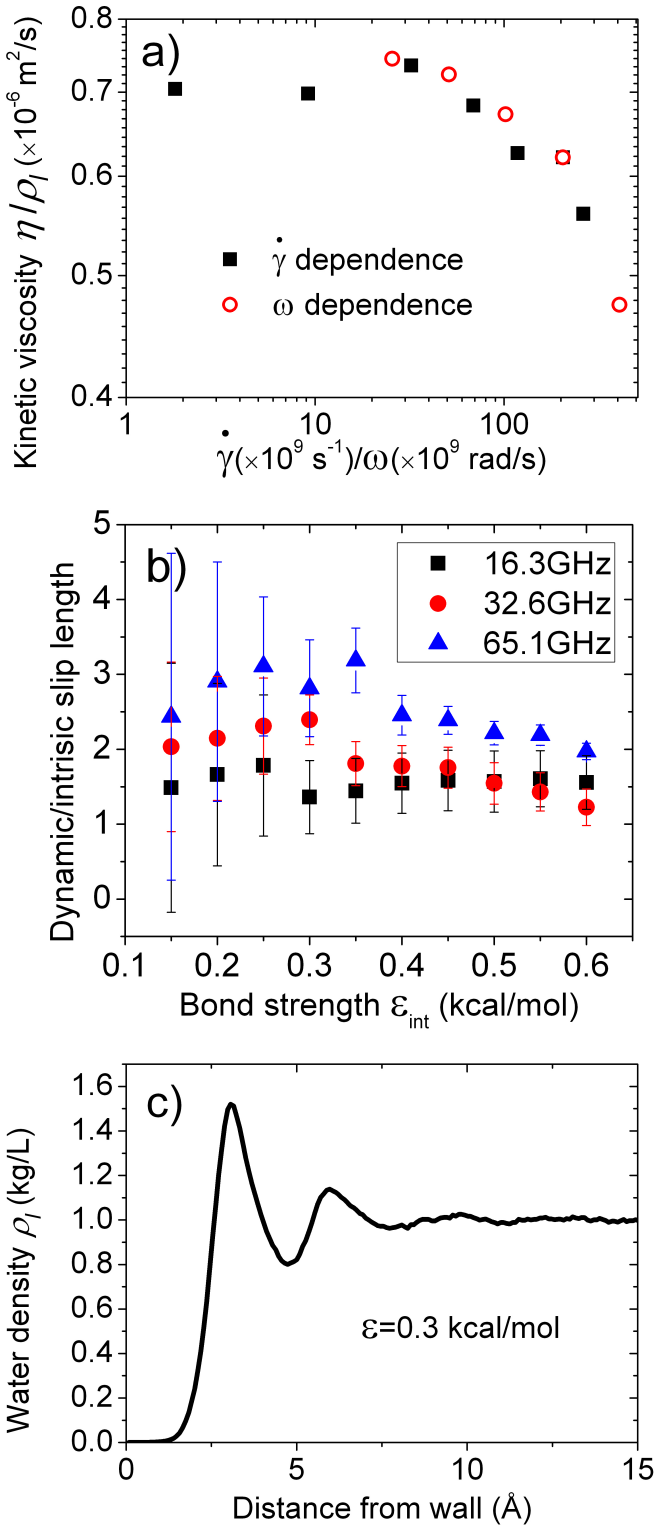

Figure 3.7: Effects needed to consider in a slip model. a) Frequency dependency of water viscosity; b) Frequency dependency of slip length: ratio of dynamic length and static slip length ; c) Water density profile near the interface

imaginary part of $\Delta\omega$, that is

$$\Delta f = \frac{\mathrm{Im}(\Delta\omega)}{2\pi}, \tag{3.26}$$

$$\Delta D = \frac{\mathrm{Re}(\Delta\omega)}{f_0}. \tag{3.27}$$

A slip boundary condition Eq. 3.20, which takes into account the inertia of the first liquid layer, is then used to complete the set of equations for the new slip model and to make the equations solvable. One can derive (details in supporting information) the following relations between the mechanical response of QCM (frequency and damping shifts) and the normalized dynamic slip length b_d:

$$\frac{\Delta f}{f_0} = -\frac{1}{2Z}\sqrt{\frac{\rho_l \eta_d \omega}{2}}\frac{1+2a}{1+2b_d+[(1+2a)^2+1]b_d^2}, \tag{3.28}$$

$$\frac{\Delta D}{2\pi} = \frac{1}{2Z}\sqrt{\frac{\rho_l \eta_d \omega}{2}}\frac{1+[(1+2a)^2+1]b_d}{1+2b_d+[(1+2a)^2+1]b_d^2}. \tag{3.29}$$

To test applicability of the new model, in Fig. 3.8 we plot the frequency response $\left|\frac{\Delta f}{f_0}\right|$ (or $-\frac{\Delta f}{f_0}$ as frequency always decreases in our case) and the damping response $\frac{\Delta D}{2\pi}$ as a function of the normalized slip length for five different frequencies. These plots demonstrate that slip has dramatic consequences on both frequency shift and energy dissipation in our high frequency resonator, especially when the slip length is comparable to the penetration length of liquid. Both the absolute value of frequency shift and the damping rate shift decrease with slip length. In Fig. 3.8 at the same normalized slip length, the absolute values of frequency shift and damping rate shift are generally larger when the resonant frequency is higher. Both the trends and the quantitative data obtained in MD simulations (symbols in Fig. 3.8) are well described by our model (dashed lines). In order to predict the frequency shift and damping rate shift using our model, we need to know the surface density of the first water layer or the inertia length l_a. A simple estimation of the surface number density n_a and inertia length l_a in Eq. 3.21 is $n_a{=}n^{\frac{2}{3}}$ and $l_a{=}n^{-\frac{1}{3}}{=}3.1$ Å, where n is the number density of bulk water. The exact values of n_a and l_a depend on chemistry and structure of the interface. We found, however, that this dependence is not strong and in our simulations, an inertia length of 3.8±0.3 Å fits well the mechanical response of QCM ($\frac{\Delta f}{f_0}$ and ΔD) at all frequencies and bond strengths. The reader

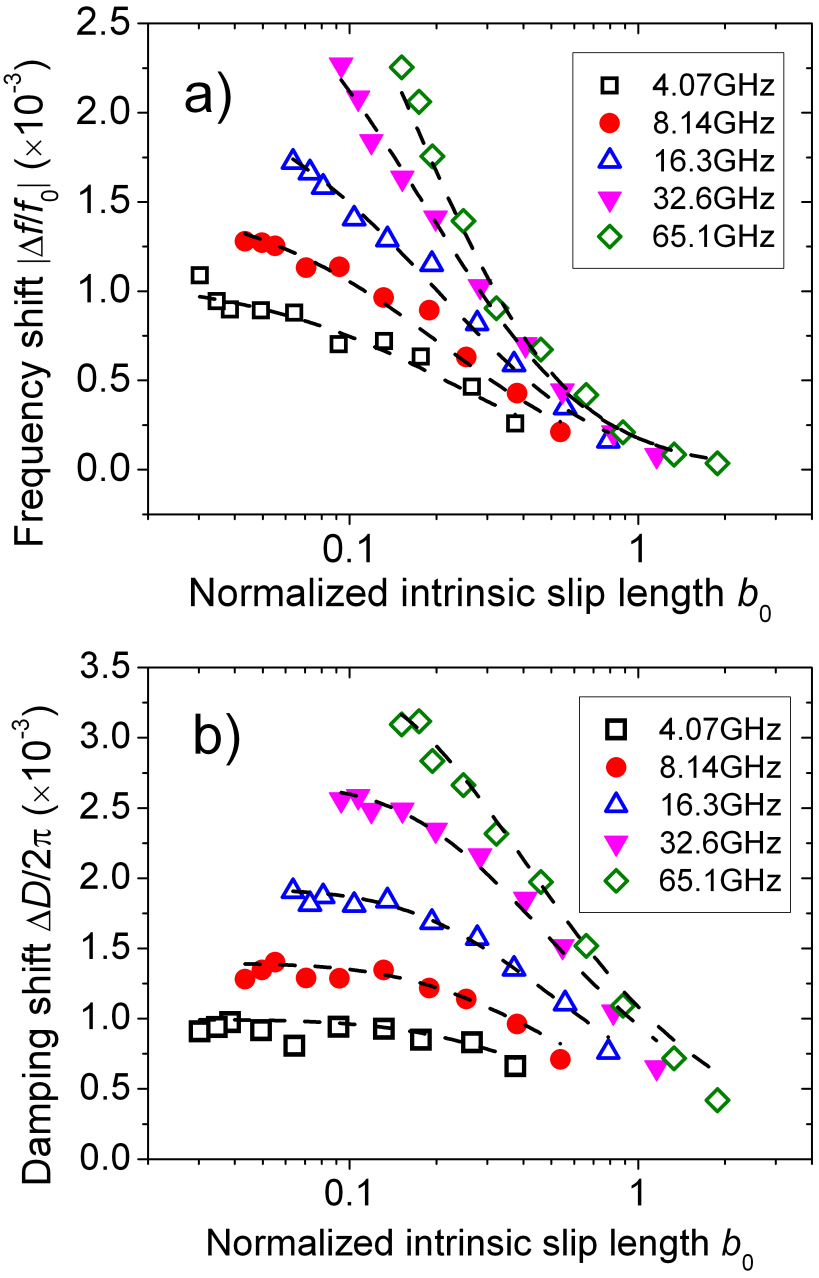

Figure 3.8: Results of MD simulations (symbols) for a) frequency shift and b) damping shift as a function of reduced slip length b_0. Dashed lines represent the predictions from our analytical model described in the text.

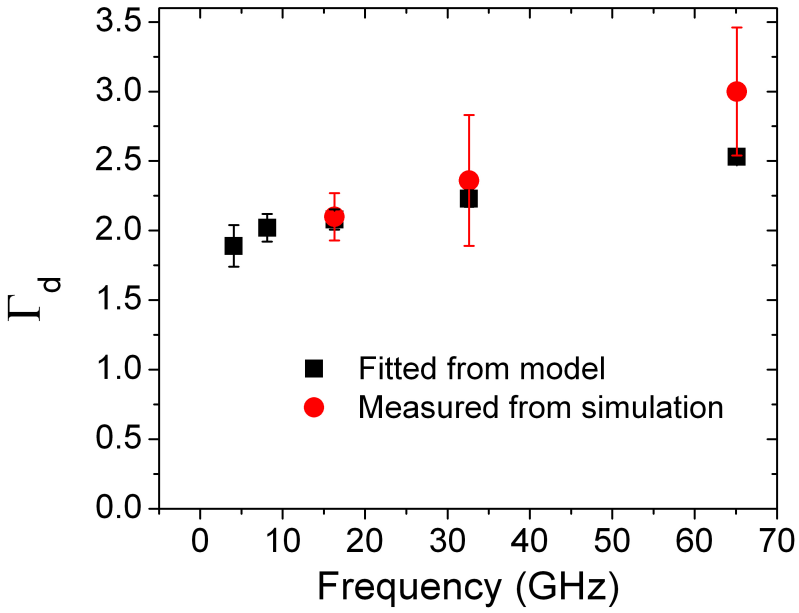

Figure 3.9: Dependence of the ratio between dynamic and intrinsic slip length on frequency.

should note that in Fig. 3.8 we plotted the results against the intrinsic slip length l_0, since it is a physical quantity that is typically measured in slip experiments and often studied in computer simulations. Our data can be easily converted to be a function of the dynamic slip length using the scaling factor Γ_d, as defined in Eq. 3.9. This factor represents the ratio of the dynamic and the static slip lengths. Γ_d can be either determined by measuring the dynamic slip length using Eq. 3.23 (as was done in our simulations) or by fitting the measured mechanical response (Δf or ΔD) to the equations of our model. We plot the values of Γ_d obtained using the two methods as a function of frequency in Fig. 3.9 and we find a good agreement between the estimates within the error bar of calculations.

As will be demonstrated below, it is useful to rewrite Eq. 3.28 and Eq. 3.29 as the ratio and the difference of the damping shift $\frac{\Delta D}{2\pi}$ and the absolute value of frequency shift $\left|\frac{\Delta f}{f_0}\right|$, namely,

$$\frac{\Delta D/2\pi}{|\Delta f/f_0|} = \frac{1+[(1+2a)^2+1]b_d}{1+2a}, \tag{3.30}$$

$$\frac{\Delta D}{2\pi} - \left|\frac{\Delta f}{f_0}\right| = \frac{1}{\pi Z}\sqrt{\frac{\rho_l \eta_d \omega}{2}}\frac{[(1+2a)^2+1]b_d - 2a}{1+2b_d+[(1+2a)^2+1]b_d^2}. \tag{3.31}$$

In Fig. 3.10 (a) we plot the ratio in Fig. 3.30 as a function of b_d for data calculated from

MD simulations. Irrespectively of the frequency, all simulation data falls on the same line. This linear dependence can be understood by considering that a is usually smaller than 1 (the largest a in our simulation is about 0.27), which means that $l_a < \delta$. With that in mind, we can simplify the expression for the ratio between damping rate and frequency shift (Fig. 3.30) to the 1^{st} order of a as follows

$$\frac{\Delta D/2\pi}{|\Delta f/f_0|} \approx 2b_d + 1 - 2a. \tag{3.32}$$

The above expression can be furthermore simplified to the 0^{th} order of a and the right hand side of Eq. 3.32 is approximately equal to $2b_d + 1$. This relationship is plotted as a dashed line in Fig. 3.10 (a) and it shows a good agreement with the MD data. The one-to-one correspondence between the normalized dynamic slip length and the ratio in Eq. 3.30 provides an easy way of estimating the slip length from QCM measurements. This estimation is generally more accurate when the ratio is large so that the contributions to the ratio from any source (e.g., interfacial inertia) other than slip can be neglected. In other words, if the normalized slip length is too small (as compared to 1), one cannot determine its value from Eq. 3.32. For small slip lengths, the relationship $\frac{\Delta D/2\pi}{|\Delta f/f_0|} \approx 2b_d + 1$ is not a good approximation. According to our model, in this limit it is possible to obtain some qualitative information about the slip length and more specifically one can determine if the normalized slip length b_d is smaller, larger, or comparable to the normalized inertia length a, where the latter quantity is a measure of the width of the interface. This comparison can be accomplished by analyzing the difference $\frac{\Delta D}{2\pi}$ and $\left|\frac{\Delta f}{f_0}\right|$, because the sign of the expression in Eq. 3.31 is well approximated by the sign of $b_d - a$, that is

$$sign\left[\frac{\Delta D}{2\pi} - \left|\frac{\Delta f}{f_0}\right|\right] = sign\left\{[(1+2a)^2 + 1]b_d - 2a\right\} \approx sign(b_d - a), \tag{3.33}$$

which means when the normalized dynamic slip length b_d is smaller than the normalized inertia length a, the frequency shift is larger than the damping rate shift and vice versa. A negative value of the difference in Eq. 3.31 is not predicted by either the no-slip model (Kanazawa model[38]) or by earlier slip models[36;42–45] that ignore the inertia of the interfacial liquid. We plot the difference in Eq. 3.31 in Eq. 3.10 (b) as a function of frequency for various bond strengths (slip lengths). As shown by our MD data (symbols), the expression given by Eq. 3.31 can become negative in the no-slip limit or when the normalized slip length is smaller than

normalized inertia length. This finding from simulation is again consistent with our analytical model (Eq. 3.33) and provides a possible explanation to the origin of the negative difference in Eq. 3.31 observed in some QCM experiments[44]. Additionally, from the curves in Fig. 3.10 (b) we can see that independently of whether the difference is positive or negative, the absolute value of this difference generally increases with increasing frequency, which is consistent with trends observed in experiments[46].

3.5 Discussion and conclusion

It is yet instructive to discuss possible limits of applicability of our model and under what conditions this model becomes necessary and outperforms earlier low-frequency models. First of all, although the model has been tested against simulations performed at high frequencies, it is expected to apply also in the limit of low frequencies. It is because there is no discontinuous change in viscosity, slip length, and interfacial inertia as a function of frequency and the dependence of these quantities on frequency is monotonic (see Fig. 3.7). Contributions from the three phenomena identified in this paper (viscosity and slip length dependence on frequency and interfacial inertia) are present at low frequencies, but these contributions will be negligible in the zero frequency limit. In fact, as shown in supporting information, in the zero frequency limit our generalized model will be reduced to the previously developed models summarized in Eq. 3.15 and Eq. 3.16 and therefore our model can be thought of as a generalized approach. Frequency enters into the slip model in many different ways. First of all, penetration length that characterizes the dimensions of the liquid wave is dependent on frequency. From Eq. 3.15 and Eq. 3.16 one can see that it is the normalized slip length that governs the change of frequency shift and damping shift. The smaller the normalization factor (penetration length), the bigger the normalized slip length. Since the slip length is typically in the nm regime, models assuming no-slip boundary condition that work very well for macroscopic systems will begin to fail with the penetration length being reduced to the nm length scales. Taking QCM as an example, a fundamental frequency of about 5 MHz will lead to a penetration length of about 250 nm for water. Assuming the slip length is 10 nm, slip will cause a decrease of 7.7% in the absolute value of the frequency shift and 0.3% in the damping rate shift, as compared to the no-slip condition. Consequently, ignoring the slip will lead to 7.7% and 0.3% errors in frequency shift and damping rate shift, respectively, which effect is not dramatic. However, if the operating

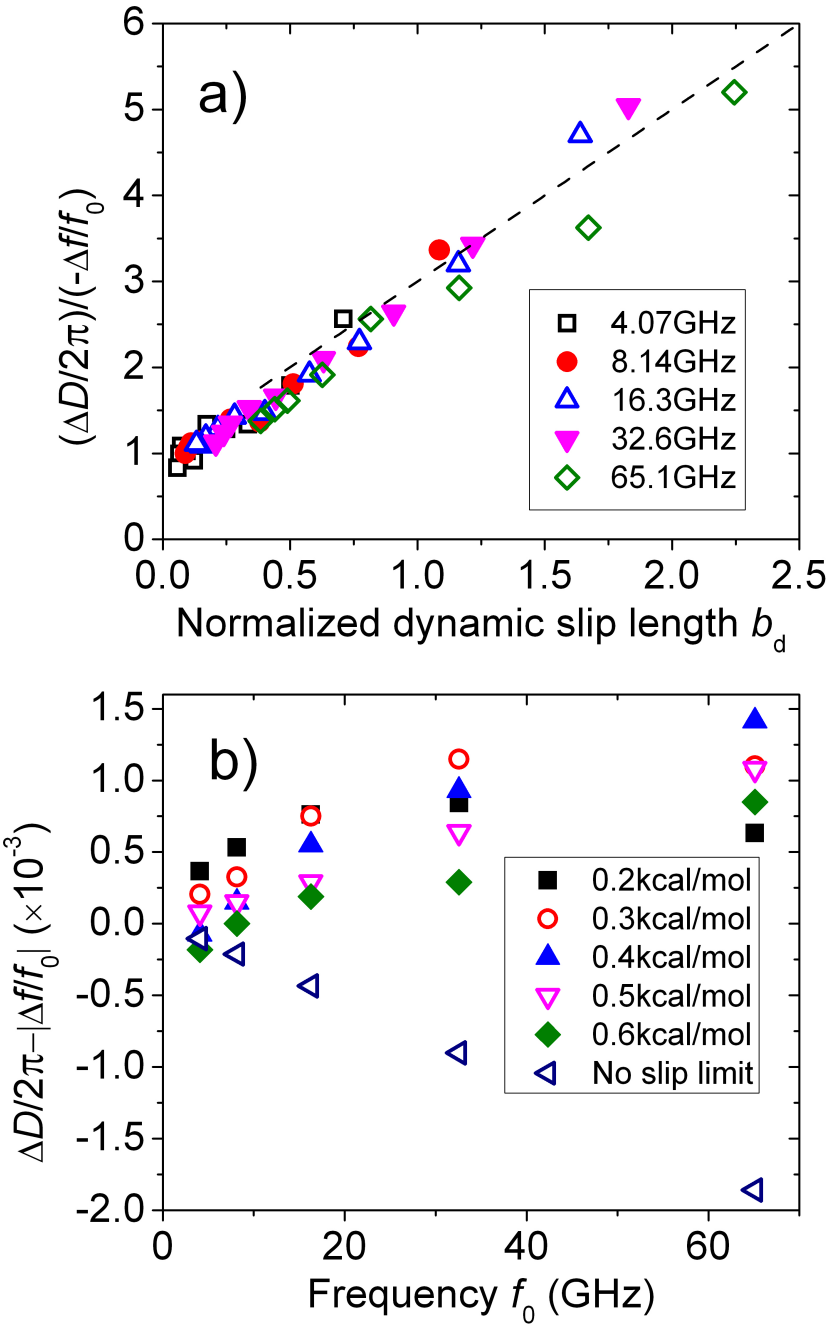

Figure 3.10: Comparison between frequency shift and damping rate shift. a) The ratio between damping rate shift and frequency shift (symbols) as a function of the reduced dynamic slip length. (dash line is a universal linear relationship $y = 2x + 1$). b) The sum of damping rate shift and frequency shift (or the difference of their magnitudes) plotted as a function of frequency for different interfacial bond strength ε_{int}.

frequency of QCM is increased to 500 MHz (which corresponds to a 25 nm penetration length for water), the same amount of slip will result in 53% and 15% errors in frequency shift and damping rate shift, respectively. In this case, it is necessary to use a slip model to predict mechanical behavior of QCM. As shown by our simulations on water, when the frequency is as high as a few hundred MHz or higher, the slip length may be quite different from that measured in the static shearing experiments or simulations. This is a somewhat surprising phenomenon that has not been previously reported in literature. We expect this phenomenon to occur in a broad range of liquids, since most liquids have a longer relaxation time than water. Thus our results suggest that in typical QCM experiments with polymeric liquids, one should use the concept of a dynamic slip length and a generalized slip model that considers frequency effects. The identified frequency dependence of slip length also suggests that the liquid/solid friction coefficient may need to be treated as interfacial viscosity. Mechanical analog models, similar to those already developed for liquid viscosity, may be useful in describing solid/liquid friction and in identifying underlying physics. In fact, simple mechanical analog models of solid/liquid friction have been already proposed to shed light on certain experimental observations[41;57]. On the other hand, molecular-level understanding of frequency dependence of slip length is still missing and providing such understanding is beyond the scope of this paper. Another phenomenon that enters our generalized model is the inertia of the first liquid layer. One should be aware of the difference between this interfacial inertia and the adsorption on surface, although both these effects lead to an increase in the magnitude of frequency shift. Adsorption requires a much stronger interaction between the solid and the liquid molecules and if adsorption takes place, the liquid density profile near the solid surface is expected to have a much sharper peak than that observed in our simulations (see Fig. 3.7 (c)). Velocity of the adsorbed layer should be equal to the velocity of the solid wall and consequently the slip can only take place between the adsorbed liquid layer and the liquid above it. For atomically smooth surfaces, slip between the adsorbed layer and the liquid is not likely to happen. The inertia effect from the interfacial liquid is more general than adsorption, as it is not limited to the case of strong interactions between liquid and solid. Our treatment on the first layer water is a simple way to include effects from the interfacial region, where the properties of liquid, such as density and viscosity, differ from those in the bulk liquid. This approach is more accurate than the sharp interface condition that assumes the width of interfacial region to be zero. For water on our atomically smooth surface, we found the interfacial layer to be about one monolayer thick,

however this thickness may vary depending on the surface conditions. In general, the width of the interfacial region is expected to be on the order of a few molecular diameters. Since in currently used QCM technology, typical surfaces are not atomically smooth, it is interesting to ask about the effects of surface roughness on solid/liquid friction. This topic is an active area of research[25;44;58–60] and many insights have been brought through MD simulations[25]. In most cases, roughness was shown to reduce the slip length. Roughness have been also postulated to be responsible for the negative value of the difference between the damping rate shift and the magnitude of the frequency shift (Eq. 3.31) observed in in some QCM experiments[46]. This negative value is not predicted by previous slip-boundary models. To explain this phenomenon, McHale *et al.*[44] introduced the concept of a negative slip length, which was assumed to be the consequence of surface roughness. Our model provides a possible alternative explanation of the experimental observation without the need to invoke a negative slip length. It is likely that roughness affects both the slip length and the inertia length (or the width of the interfacial region). A reduced (although still positive) slip length and an increased inertia length in our model will result in a negative value of the difference given by Eq. 3.31 and therefore this model may explain the experimentally observed effects of roughness. The effects of roughness are expected to be much less important when the size of shear-wave acoustic resonators is reduced, such as in the case of MEMS and NEMS devices.

In summary, the effects of slip boundary condition have been investigated by MD simulation. We discovered new phenomena that emerge at high vibrational frequencies. For example, we have shown that slip length is frequency dependent and to account for this dependence explicitly, we introduce a concept of a dynamic slip length. We have also shown that the interface between solid and liquid cannot be treated as sharp and that the inertia of water near the interface contributes to friction. A generalized slip model that includes newly discovered high-frequency phenomena is developed to connect the slip length and mechanical response of high frequency acoustic resonators. The model shows excellent agreement with MD simulations. A linear relationship between the ratio of measured mechanical properties and the slip length is discovered. This relationship provides a means for determining slip length experimentally, which had been an outstanding challenge in the field.

Bibliography

[1] R. Lucklum and P. Hauptmann, "The quartz crystal microbalance: mass sensitivity, viscoelasticity and acoustic amplification," *SENSORS AND ACTUATORS B-CHEMICAL*, vol. 70, pp. 30–36, NOV 1 2000.

[2] J. Grate, "Acoustic wave microsensor arrays for vapor sensing," *CHEMICAL REVIEWS*, vol. 100, pp. 2627–2647, JUL 2000.

[3] M. Rodahl and B. Kasemo, "On the measurement of thin liquid overlayers with the quartz-crystal microbalance," *SENSORS AND ACTUATORS A-PHYSICAL*, vol. 54, pp. 448–456, JUN 1996.

[4] R. Lucklum, C. Behling, R. Cernosek, and S. Martin, "Determination of complex shear modulus with thickness shear mode resonators," *JOURNAL OF PHYSICS D-APPLIED PHYSICS*, vol. 30, pp. 346–356, FEB 7 1997.

[5] K. Zhang, S.-H. Choy, L. Zhao, H. Luo, H. L.-W. Chan, and Y. Wang, "Shear-mode PMN-PT piezoelectric single crystal resonator for microfluidic applications," *MICROELECTRONIC ENGINEERING*, vol. 88, pp. 1028–1032, JUN 2011.

[6] K. Zhang, L. Zhao, S. Guo, B. Shi, Y. Chen, H. L. W. Chan, and Y. Wang, "A microfluidic system with embedded acoustic wave sensor for in situ detection of dynamic fluidic properties," *MICROELECTRONIC ENGINEERING*, vol. 87, pp. 658–662, APR 2010.

[7] J. Krim, D. Solina, and R. Chiarello, "Nanotribology of a Kr monolayer - a quartz-crystal microbalance study of atomic-scale friction," *PHYSICAL REVIEW LETTERS*, vol. 66, no. 2, pp. 181–184, 1991.

[8] A. Dayo, W. Alnasrallah, and J. Krim, "Superconductivity-dependent sliding friction," *PHYSICAL REVIEW LETTERS*, vol. 80, pp. 1690–1693, FEB 23 1998.

[9] M. Robbins and J. Krim, "Energy dissipation in interfacial friction," *MRS BULLETIN*, vol. 23, pp. 23–26, JUN 1998.

[10] C. L. M. H. Navier, "Memoire sur les lois du mouvement des fluides," *Mémoires de l'Académie des sciences de l'Institut de France*, vol. 6, pp. 389–440, 1823.

[11] Y. Zhu and S. Granick, "Limits of the hydrodynamic no-slip boundary condition," *PHYSICAL REVIEW LETTERS*, vol. 88, MAR 11 2002.

[12] T. Schmatko, H. Hervet, and L. Leger, "Friction and slip at simple fluid-solid interfaces: The roles of the molecular shape and the solid-liquid interaction," *PHYSICAL REVIEW LETTERS*, vol. 94, JUN 24 2005.

[13] R. Pit, H. Hervet, and L. Leger, "Direct experimental evidence of slip in hexadecane: Solid interfaces," *PHYSICAL REVIEW LETTERS*, vol. 85, pp. 980–983, JUL 31 2000.

[14] C. L. Henry and V. S. J. Craig, "Measurement of no-slip and slip boundary conditions in confined Newtonian fluids using atomic force microscopy," *PHYSICAL CHEMISTRY CHEMICAL PHYSICS*, vol. 11, no. 41, pp. 9514–9521, 2009.

[15] P. Roach, G. McHale, C. R. Evans, N. J. Shirtcliffe, and M. I. Newton, "Decoupling of the liquid response of a superhydrophobic quartz crystal microbalance," *LANGMUIR*, vol. 23, pp. 9823–9830, SEP 11 2007.

[16] M. Gad-el Hak, "The fluid mechanics of microdevices - The Freeman Scholar Lecture," *JOURNAL OF FLUIDS ENGINEERING-TRANSACTIONS OF THE ASME*, vol. 121, pp. 5–33, MAR 1999.

[17] G. M. Whitesides, "The origins and the future of microfluidics," *NATURE*, vol. 442, pp. 368–373, JUL 27 2006.

[18] J. Friend and L. Y. Yeo, "Microscale acoustofluidics: Microfluidics driven via acoustics and ultrasonics," *REVIEWS OF MODERN PHYSICS*, vol. 83, pp. 647–704, JUN 20 2011.

[19] D. M. Karabacak, V. Yakhot, and K. L. Ekinci, "High-frequency nanofluidics: An experimental study using nanomechanical resonators," *PHYSICAL REVIEW LETTERS*, vol. 98, JUN 22 2007.

[20] C. Neto, D. Evans, E. Bonaccurso, H. Butt, and V. Craig, "Boundary slip in Newtonian liquids: a review of experimental studies," *REPORTS ON PROGRESS IN PHYSICS*, vol. 68, pp. 2859–2897, DEC 2005.

[21] B.-Y. Cao, J. Sun, M. Chen, and Z.-Y. Guo, "Molecular Momentum Transport at Fluid-Solid Interfaces in MEMS/NEMS: A Review," *INTERNATIONAL JOURNAL OF MOLECULAR SCIENCES*, vol. 10, pp. 4638–4706, NOV 2009.

[22] J. Ellis and M. Thompson, "Slip and coupling phenomena at the liquid-solid interface," *PHYSICAL CHEMISTRY CHEMICAL PHYSICS*, vol. 6, no. 21, pp. 4928–4938, 2004.

[23] J. Barrat and L. Bocquet, "Influence of wetting properties on hydrodynamic boundary conditions at a fluid/solid interface," *FARADAY DISCUSSIONS*, vol. 112, pp. 119–127, 1999.

[24] L. Bocquet and E. Charlaix, "Nanofluidics, from bulk to interfaces," *CHEMICAL SOCIETY REVIEWS*, vol. 39, no. 3, pp. 1073–1095, 2010.

[25] C. Sendner, D. Horinek, L. Bocquet, and R. R. Netz, "Interfacial Water at Hydrophobic and Hydrophilic Surfaces: Slip, Viscosity, and Diffusion," *LANGMUIR*, vol. 25, pp. 10768–10781, SEP 15 2009.

[26] D. M. Huang, C. Sendner, D. Horinek, R. R. Netz, and L. Bocquet, "Water Slippage versus Contact Angle: A Quasiuniversal Relationship," *PHYSICAL REVIEW LETTERS*, vol. 101, NOV 28 2008.

[27] R. Voronov, D. Papavassiliou, and L. Lee, "Boundary slip and wetting properties of interfaces: Correlation of the contact angle with the slip length," *JOURNAL OF CHEMICAL PHYSICS*, vol. 124, MAY 28 2006.

[28] N. Priezjev and S. Troian, "Molecular origin and dynamic behavior of slip in sheared polymer films," *PHYSICAL REVIEW LETTERS*, vol. 92, JAN 9 2004.

[29] A. Martini, H.-Y. Hsu, N. A. Patankar, and S. Lichter, "Slip at high shear rates," *PHYSICAL REVIEW LETTERS*, vol. 100, MAY 23 2008.

[30] N. V. Priezjev, "Rate-dependent slip boundary conditions for simple fluids," *PHYSICAL REVIEW E*, vol. 75, MAY 2007.

[31] N. V. Priezjev, "Shear rate threshold for the boundary slip in dense polymer films," *PHYSICAL REVIEW E*, vol. 80, SEP 2009.

[32] Z. Zhang, H. Zhang, and H. Ye, "Pressure-driven flow in parallel-plate nanochannels," *APPLIED PHYSICS LETTERS*, vol. 95, OCT 12 2009.

[33] H. Zhang, Z. Zhang, Y. Zheng, and H. Ye, "Corrected second-order slip boundary condition for fluid flows in nanochannels," *PHYSICAL REVIEW E*, vol. 81, JUN 8 2010.

[34] P. Thompson and S. Troian, "A general boundary condition for liquid flow at solid surfaces," *NATURE*, vol. 389, pp. 360–362, SEP 25 1997.

[35] R. B. Bird, R. C. Armstrong, and O. Hassager, *Dynamics of polymeric liquids.* Wiley-Interscience, second ed., 1987.

[36] B. Persson, *Sliding friction.* Springer, second ed., 2000.

[37] G. Sauerbrey, "Verwendung von Schwingquarzen zur WÃ¤gung dÃ¼nner Schichten und zur MikrowÃ¤gung," *Z. Phys*, vol. 155, no. 2, pp. 206–222, 1959.

[38] K. K. Kanazawa and G. J. Gordon, "Frequency of a quartz microbalance in contact with liquid," *ANALYTICAL CHEMISTRY*, vol. 57, no. 8, pp. 1770–1771, 1985.

[39] J. S. Martin, E. V. Granstaff, and C. G. Frye, "Characterization of a quartz crystal microbalance with simultaneous mass and liquid loading," *ANALYTICAL CHEMISTRY*, vol. 63, no. 20, pp. 2272–2281, 1991.

[40] M. Voinova, M. Jonson, and B. Kasemo, "'Missing mass' effect in biosensor's QCM applications," *BIOSENSORS & BIOELECTRONICS*, vol. 17, pp. 835–841, OCT 2002.

[41] F. Ferrante, A. L. Kipling, and M. Thompson, "Molecular slip at the solid-liquid interface of an acoustic-wave sensor," *JOURNAL OF APPLIED PHYSICS*, vol. 76, pp. 3448–3462, SEP 15 1994.

[42] J. Ellis and G. Hayward, "Interfacial slip on a transverse-shear mode acoustic wave device," *JOURNAL OF APPLIED PHYSICS*, vol. 94, pp. 7856–7867, DEC 15 2003.

[43] L. Daikhin, E. Gileadi, V. Tsionsky, M. Urbakh, and G. Zilberman, "Slippage at adsorbate-electrolyte interface. Response of electrochemical quartz crystal microbalance to adsorption," *ELECTROCHIMICA ACTA*, vol. 45, no. 22-23, pp. 3615–3621, 2000.

[44] G. McHale and M. Newton, "Surface roughness and interfacial slip boundary condition for quartz crystal microbalances," *JOURNAL OF APPLIED PHYSICS*, vol. 95, pp. 373–380, JAN 1 2004.

[45] H. Zhuang, P. Lu, S. P. Lim, and H. P. Lee, "Effects of interface slip and viscoelasticity on the dynamic response of droplet quartz crystal microbalances," *ANALYTICAL CHEMISTRY*, vol. 80, pp. 7347–7353, OCT 1 2008.

[46] B. Du, E. Goubaidoulline, and D. Johannsmann, "Effects of laterally heterogeneous slip on the resonance properties of quartz crystals immersed in liquids," *LANGMUIR*, vol. 20, pp. 10617–10624, NOV 23 2004.

[47] http://lammps.sandia.gov/.

[48] W. Jorgensen, J. Chandrasekhar, J. Madura, R. Impey, and M. Klein, "Comparison of simple potential functions for simulating liquid water," *JOURNAL OF CHEMICAL PHYSICS*, vol. 79, no. 2, pp. 926–935, 1983.

[49] E. Pollock and J. Glosli, "Comments on P(3)M, FMM, and the Ewald method for large periodic coulombic systems," *COMPUTER PHYSICS COMMUNICATIONS*, vol. 95, pp. 93–110, JUN 1996.

[50] J. Ryckaert, G. CiccottiI, and H. Berendsen, "Numerical-integration of cartesian equations of motion of a system with constraints - molecular-dynamics of n-alkanes," *JOURNAL OF COMPUTATIONAL PHYSICS*, vol. 23, no. 3, pp. 327–341, 1977.

[51] A. A. Pahlavan and J. B. Freund, "Effect of solid properties on slip at a fluid-solid interface," *PHYSICAL REVIEW E*, vol. 83, FEB 7 2011.

[52] R. Khare, J. dePablo, and A. Yethiraj, "Molecular simulation and continuum mechanics study of simple fluids in non-isothermal planar couette flows," *JOURNAL OF CHEMICAL PHYSICS*, vol. 107, pp. 2589–2596, AUG 15 1997.

[53] R. Khare, P. Keblinski, and A. Yethiraj, "Molecular dynamics simulations of heat and momentum transfer at a solid-fluid interface: Relationship between thermal and velocity slip," *INTERNATIONAL JOURNAL OF HEAT AND MASS TRANSFER*, vol. 49, pp. 3401–3407, SEP 2006.

[54] F. Muller-Plathe, "Reversing the perturbation in nonequilibrium molecular dynamics: An easy way to calculate the shear viscosity of fluids," *PHYSICAL REVIEW E*, vol. 59, pp. 4894–4898, MAY 1999.

[55] M. S. Kelkar, J. L. Rafferty, E. J. Maginn, and J. I. Siepmann, "Prediction of viscosities and vapor-liquid equilibria for five polyhydric alcohols by molecular simulation," *FLUID PHASE EQUILIBRIA*, vol. 260, pp. 218–231, NOV 1 2007.

[56] H. Hu, G. Carson, and S. Granick, "Relaxation-time of confined liquids under shear," *PHYSICAL REVIEW LETTERS*, vol. 66, pp. 2758–2761, MAY 27 1991.

[57] F. Lu, H. Lee, and S. Lim, "Mechanical description of interfacial slips for quartz crystal microbalances with viscoelastic liquid loading," *SMART MATERIALS & STRUCTURES*, vol. 12, pp. 881–888, DEC 2003.

[58] C. Kunert and J. Harting, "Roughness induced boundary slip in microchannel flows," *PHYSICAL REVIEW LETTERS*, vol. 99, OCT 26 2007.

[59] L. Macakova, E. Blomberg, and P. M. Claesson, "Effect of adsorbed layer surface roughness on the QCM-D response: Focus on trapped water," *LANGMUIR*, vol. 23, pp. 12436–12444, NOV 20 2007.

[60] K. Rechendorff, M. B. Hovgaard, M. Foss, and F. Besenbacher, "Influence of surface roughness on quartz crystal microbalance measurements in liquids," *JOURNAL OF APPLIED PHYSICS*, vol. 101, JUN 1 2007.

4 Green-Kubo relation for liquid-solid friction

4.1 Introduction

The nature of the liquid-solid (L-S) boundary conditions have been a subject of an intense scientific debate for over a century[1–3]. It is only recently that the existence of a slip at such interfaces has been accepted[4–7]. The urgency of understanding slip and related phenomena has increased further with the miniaturization of devices. In particular, in micro- and nano-fluidics[8–10] the presence or absence of slip and the magnitude of friction at the L-S interface will have a large effect on the flow rate of the fluid. L-S slip is often characterized by a slip length l or a friction coefficient

$$\bar{\eta} = \eta/l, \tag{4.1}$$

where η is the viscosity of the liquid. Slip length is defined as the extrapolated distance where the velocity of the liquid matches the velocity of the solid wall, as shown in Fig. 3.1. One of the major challenges in this field is the ability to measure or predict the slip length, or alternatively the coefficient of friction at the L-S interface. While experimental measurements are plagued with their own limitations (see for instance Ref.[11], here we focus on the challenges associated with predicting the friction coefficient from atomistic simulations. In particular, non-equilibrium molecular dynamics (NEMD) simulations, which can be invaluable in providing insights into relations between interfacial properties and friction[12–15], are limited (with few exceptions, see for instance Ref.[16] to sliding velocities and shear rates that are orders of magnitude higher than in typical experiments. In the case of L-S friction, such simulations often trigger a non-linear behavior, leading to qualitative deviations from experiments. More

explicitly, for the viscous friction law

$$F = -\bar{\eta}u, \tag{4.2}$$

where F is the friction force per unit area, u is the slip velocity, the non-linear behavior means that at large enough u, $\bar{\eta}$ is not constant but it depends on u. Here, we use the linear response theory and the Generalized Langevin Equation (GLE) to derive a new relationship for predicting friction from equilibrium molecular dynamics (EMD) simulations. Because friction is calculated from equilibrium properties of the system, by nature this approach overcomes the time scale limitations of traditional NEMD techniques. Our new theory is validated by comparing results of EMD simulations with NEMD results extrapolated to the limit of low sliding velocities.

A pioneering attempt to predict friction for L-S interfaces from EMD simulations was reported by Bocquet and Barrat (BB)[17]. It was proposed that the coefficient of friction $\bar{\eta}$ can be calculated from the integral of the time correlation function of the total friction force F_{tot} between the solid and the liquid layer adjacent to the solid

$$\bar{\eta} = \frac{1}{SkT}\int_0^\infty \langle F_{\text{tot}}(0)F_{\text{tot}}(t)\rangle_{\text{EC}}\,\mathrm{d}t. \tag{4.3}$$

In the above expression, S is the surface area, k is the Boltzmann constant, T is temperature and $\langle ...\rangle_{\text{EC}}$ denotes ensemble averages at equilibrium condition. Application of the above theory led to two numerical issues, recognized by the authors themselves[17]: 1) Eq. 4.3 vanishes for finite systems and a cut-off time in the upper limit of the integral is necessary to predict the integral in the thermodynamic limit. 2) Predictions of Eq. 4.3 do not agree quantitatively with the fitted parameters based on the transverse momentum density autocorrelation function. In addition, a number of criticisms have been raised in literature, questioning whether $\bar{\eta}$ in Eq. 4.3 corresponds to the intrinsic properties of the interface[18–20]. BB responded to these criticisms in another paper[21] and explained that results from simulations could be spurious if the limit of the fluid particles going to infinity (the thermodynamic limit) and the limit of time going to infinity are not taken in the proper order. In this debate one critical issue was ignored, which is that friction coefficient is not a bulk property. Therefore, a large volume of the liquid is not necessary for friction to arise at the L-S interface. For example, L-S friction is present in a nanotube[22–24]

where the number of liquid molecules is highly constrained and in such confined systems[4;25] one is not allowed to take the thermodynamic limit of the system size. Furthermore, L-S friction is local, which means that for an inhomogeneous solid surface[26], friction coefficient can be different from one domain to another, and for a mixture of liquid[27], friction coefficient can be different from one kind of liquid particle to another. It is straightforward to see that due to its mathematical structure, expressions like Eq. 4.3 cannot capture the potential inhomogeneity of L-S friction.

In this paper, we first develop a formal GK relation for L-S friction that overcomes the limitations of previous models and allows high efficient numerical evaluation of friction. Subsequently, we validate our GK relation numerically by demonstrating a very good agreement between the predictions from our GK relation for the L-S friction coefficient and the measurements from NEMD simulations. Finally, for completeness we compare performance of the newly developed GK relation and that proposed previously by BB.

4.2 Theoretical model

4.2.1 General strategy for the derivation of a GK relation for L-S friction

Having recognized that L-S friction is local and shall not be described by a bulk-like transport coefficient that vanishes with finite system size, we shall construct the GK relation from the dynamics of individual liquid particles near the solid wall. Our approach to deriving a GK relation therefore differs from the standard one summarized by McQuarrie[28], which starts from the Fourier transform of the diffusion-like partial differential equation

$$\frac{\partial \phi}{\partial t} = D\nabla^2\phi, \tag{4.4}$$

where ϕ is the field of interest and D is the corresponding transport coefficient. This difference in the derivation strategies arises from the difference between the L-S friction coefficient and thermal transport coefficients, such as viscosity and thermal conductivity. Due to the discontinuity at the L-S interface, the L-S friction described by Eq. 4.2 does not have a form of a partial differential equation in Eq. 4.4 that describes thermal processes at the macroscale. In fact, L-S friction is in general a mechanical process rather than a thermal one, although sometimes it can

be strongly coupled to thermal processes in the system[24;29–31]. The mechanical nature of L-S friction makes it possible for us to construct a mechanical external Hamiltonian and apply the linear response theory. Here, in order to directly take into account the microscopic details of the L-S interface, we choose to apply the external perturbation to an individual liquid particle at the L-S interface. The linear response theory then allows us to find out the expression for $\bar{\eta}_i$, which is the friction coefficient of an individual liquid particle i near the solid interface. Finally, we can sum the contributions from all the interfacial particles to obtain the total friction coefficient

$$\bar{\eta} = \frac{1}{C}\sum_i \eta_i, \tag{4.5}$$

where C is the normalization factor. For a flat surface, C can be chosen as the unit surface area. The specific choice of C is not as important. What is most important is that Eq. 4.5 demonstrates the additive property of L-S friction, which allows for modeling of inhomogeneous L-S interfaces.

4.2.2 Application of linear response theory

As we will apply the linear response theory twice in our derivation of the GK relation, we shall first briefly review the linear response technique. When a system at thermal equilibrium is slightly perturbed by an external force f, the response of the system can be predicted from the time correlation function of its thermal fluctuations at the equilibrium state. For any physical observable B of interest, its thermal average at the perturbed non-equilibrium state can be expressed as the convolution of the external force and the generalized susceptibility χ_{AB}, as follows

$$\Delta\langle B(t)\rangle = \int_{-\infty}^{\infty} \chi_{AB}(t-t')f(t')\mathrm{d}t'. \tag{4.6}$$

Here, A is the internal variable that is conjugate to f. $\Delta\langle B(t)\rangle = \langle B(t)\rangle_{\mathrm{NE}} - \langle B\rangle_{\mathrm{EC}}$, where $\langle ...\rangle_{\mathrm{NE}}$ and $\langle ...\rangle_{\mathrm{EC}}$ denote ensemble averages at non-equilibrium and equilibrium conditions, respectively. Due to the causality, χ_{AB} is non-zero only at finite times (the application of the external force f begins at time zero). The relation between the susceptibility χ_{AB} and the

corresponding time correlation of δA and δB at equilibrium is as follows

$$\chi_{AB}(t) = \begin{cases} -\frac{1}{kT}\frac{d}{dt}\langle \delta A(0)\delta B(t)\rangle_{\mathrm{EC}}, & t \geq 0 \\ 0, & t < 0 \end{cases} \tag{4.7}$$

where $\delta A = A - \langle A\rangle_{\mathrm{EC}}$ and $\delta B = B - \langle B\rangle_{\mathrm{EC}}$ are thermal fluctuations in variables A and B, respectively.

For the L-S interface, we choose the perturbation Hamiltonian to be $\Delta H = -xf\mathrm{e}^{\mathrm{i}\omega t}$, where $f\mathrm{e}^{\mathrm{i}\omega t}$ is the external drag force, x is the particle's displacement along the direction parallel to the solid wall, ω is frequency, and t is time. One can thus obtain the Fourier transformed frequency dependent susceptibility by applying the periodic external force. Under the perturbation of ΔH, the liquid particle will respond with drift velocity, the magnitude of which is determined by the balance between the external drag force, the friction force exerted by the solid wall, and the friction force exerted by the surrounding liquid. We first choose $A = x_i$ and the physical observable of interest $B = u_i$, where u_i is the drift velocity of the interfacial particle i within a plane parallel to the solid wall. By substituting Eq. 4.7 into Eq. 4.6 and taking a Fourier transform, one can show that u_i is proportional to the velocity autocorrelation function (or the mobility μ) determined in the equilibrium system

$$\langle u_i\rangle_\omega(t) = \frac{f\mathrm{e}^{\mathrm{i}\omega t}}{kT}\int_0^\infty \langle u_i(0)u_i(t)\rangle_{\mathrm{EC}}\mathrm{e}^{-\mathrm{i}\omega t}\,\mathrm{d}t, \tag{4.8}$$

$$\mu_i(\omega) = \frac{1}{kT}\int_0^\infty \langle u_i(0)u_i(t)\rangle_{\mathrm{EC}}\mathrm{e}^{-\mathrm{i}\omega t}\,\mathrm{d}t. \tag{4.9}$$

In the next step, we choose B to be the friction force F_i exerted by the solid wall on a single interfacial particle i while retaining $A = x_i$. One can then show that F_i is related to the correlation between the particle's velocity and the friction force experienced by the particle at equilibrium

$$\langle F_i\rangle_\omega(t) = \frac{f\mathrm{e}^{\mathrm{i}\omega t}}{kT}\int_0^\infty \langle u_i(0)F_i(t)\rangle_{\mathrm{EC}}\mathrm{e}^{-\mathrm{i}\omega t}\,\mathrm{d}t. \tag{4.10}$$

By definition, the friction coefficient $\bar{\eta}_i$ is equal to the ratio between the friction force and the

slip velocity. Using Eq. 4.8 and Eq. 4.10 we can write

$$\bar{\eta}_i(\omega) \equiv -\frac{\langle F_i \rangle_\omega(t)}{\langle u_i \rangle_\omega(t)} = -\frac{\int_0^\infty \langle u_i(0) F_i(t) \rangle_{\mathrm{EC}} \mathrm{e}^{-\mathrm{i}\omega t}\, \mathrm{d}t}{\int_0^\infty \langle u_i(0) u_i(t) \rangle_{\mathrm{EC}} \mathrm{e}^{-\mathrm{i}\omega t}\, \mathrm{d}t}. \tag{4.11}$$

We can now sum up the microscopic friction coefficients $\bar{\eta}_i$ in Eq. 4.11 and normalize the sum by the area S of the interface to obtain the macroscopic friction coefficient

$$\bar{\eta}(\omega) = -\frac{1}{SkT\mu_i(\omega)} \sum_i \int_0^\infty \langle u_i(0) F_i(t) \rangle_{\mathrm{EC}} \mathrm{e}^{-\mathrm{i}\omega t}\, \mathrm{d}t. \tag{4.12}$$

The order of the sum and the integral can be switched without affecting the results. It should be noted here that the sum in Eq. 4.12 can be taken over all the liquid particles since the liquid particles away from the interfacial region have no contribution to the integral due to the short-range nature of friction force ($F_i = 0$). The friction force between the liquid and the solid is either intrinsically short-range (as in the case of hydrogen or covalent bonding) or it is screened by water (for electrostatic interactions). So far we assumed that there is only one type of particle in the liquid. It is straightforward to generalize Eq. 4.12 to a mixture of liquids, $\mathrm{A}, \mathrm{B}, \mathrm{C}, ...$, based on the additive property of the friction coefficient shown in Eq. 4.5. One can simply use the same method to evalute the friction coefficient for different types of particles seperately and then sum them up to get $\bar{\eta} = \bar{\eta}_\mathrm{A} + \bar{\eta}_\mathrm{B} + \bar{\eta}_\mathrm{C} + ...$ For instance, to calculate the friction coefficient for particles of type A, one first needs to determine mobility μ_A using Eq. 4.9, plug it into Eq. 4.12 and take the summation in Eq. 4.12 over all liquid particles of type A ($\sum_{i \in \mathrm{A}}$).

4.2.3 Reformulation using the Generalized Langevin Equation

Equation 4.12 shows that the friction coefficient is inversely proportional to the liquid interfacial mobility μ. However, unfortunately this equation is not particularly practical for simulations because μ needs to be calculated for particles at the L-S interface. Liquid particles are free to diffuse away from the interface and it turns out that the finite amount of time a particle spends near the interface is not necessarily sufficient to obtain a well-converged estimate for μ. In addition, the evaluation of the interfacial mobility could be sensitive to the definition of the interfacial region. The uncertainty in the width of the interface will be transfered to the uncertainty in $\bar{\eta}$. Lastly, to obtain a reliable $\bar{\eta}$, one will need to repeat the calculation

for various interfacial widths to find a best fit or average. To avoid the above issue, we will rewrite Eq. 4.12 using the Generalized Langevin Equation (GLE) formalism[32;33]. The GLE generalizes the Brownian motion by taking into account the memory of the particle, which means that the friction force experienced by a liquid particle depends on the history of the particle's motion[34;35]. Because we are interested in calculating the L-S friction force F_i, in our formulation of GLE F_i is represented explicitly instead of being adsorbed into the random force R_i and/or the memory kernel γ_i. Thus, the extended new GLE reads

$$m_i \dot{u}_i(t) = -\int_0^t \gamma_i(t-t')u_i(t')\,\mathrm{d}t' + R_i(t) + F_i(t), \tag{4.13}$$

where m_i is the mass of the particle i, γ_i stands for the memory kernel and R_i represents the random force. We assume the following three properties that are associated with the GLE

$$\langle u(0)R(t)\rangle_i = 0,\ t > 0, \tag{4.14}$$

$$\langle F(0)R(t)\rangle_i = 0,\ t > 0, \tag{4.15}$$

$$\langle R(0)R(t)\rangle_i = kT\gamma_i(t),\ t > 0. \tag{4.16}$$

Because u and F are antisymmetric and symmetric, respectively, under time reversal, the correlation between them is antisymmetric under time reversal, which leads to $\langle u(0)F(t)\rangle_i = -\langle F(0)u(t)\rangle_i$.

Now we can use the GLE to derive a relation between different time correlation functions. It is straightforward to show that any two of the three properties of the GLE above (Eqs. 4.14-4.16) can lead to the third one. Here, we start with the GLE (Eq. 4.13 and Eqs. 4.14 and 4.15. For simplicity of the expression, we introduce the following abbreviation

$$\langle AB\rangle(\omega) \equiv \int_0^\infty \langle A(0)B(t)\rangle_{\mathrm{EC}} \mathrm{e}^{-\mathrm{i}\omega t}\,\mathrm{d}t. \tag{4.17}$$

By applying $\langle A...\rangle$ with A being $u, R, F, \dot{u}$ to both the left-hand-side (LHS) and the right-hand-side (RHS) of the GLE (Eq. 4.13), we obtain the following four equations, respectively

$$\langle uF\rangle_i(\omega) = [\mathrm{i}\omega m_i + \gamma_i(\omega)]\langle uu\rangle_i(\omega) - kT, \tag{4.18}$$

$$[\mathrm{i}\omega m_i + \gamma_i(\omega)]\langle Ru\rangle_i(\omega) = \langle RR\rangle_i(\omega) + \langle RF\rangle_i(\omega), \tag{4.19}$$

$$\langle FF\rangle_i(\omega) = [\mathrm{i}\omega m_i + \gamma_i(\omega)]\langle Fu\rangle_i(\omega), \tag{4.20}$$

$$\begin{aligned} m_i\langle \dot{u}\dot{u}\rangle_i(\omega) = \gamma_i(\omega)\langle u\dot{u}\rangle_i(\omega) + \langle RR\rangle_i(\omega) \\ +\langle FR\rangle_i(\omega) - \mathrm{i}\omega\langle uF\rangle_i(\omega). \end{aligned} \tag{4.21}$$

To derive the above equations, we used $\langle \dot{u}u\rangle_i(\omega) = -\langle u\dot{u}\rangle_i(\omega) = \langle u^2\rangle_i - \mathrm{i}\omega\langle uu\rangle_i(\omega)$, $\langle \dot{u}\dot{u}\rangle_i(\omega) = \mathrm{i}\omega\langle \dot{u}u\rangle_i(\omega)$ and $\langle \dot{u}F\rangle_i(\omega) = -\mathrm{i}\omega\langle uF\rangle_i(\omega)$. With Eqs. 4.18-4.21 and $\langle u(0)F(t)\rangle_i = -\langle F(0)u(t)\rangle_i$, one can show the following

$$\langle Fu\rangle_i(\omega) = kT - [\mathrm{i}\omega m_i + \gamma_i(\omega)]\langle uu\rangle_i(\omega), \tag{4.22}$$

$$\langle RR\rangle_i(\omega) = m_i\gamma_i(\omega)\langle u^2\rangle_i = kT\gamma_i(\omega), \tag{4.23}$$

$$\langle Ru\rangle_i(\omega) = \gamma_i(\omega)\langle uu\rangle_i(\omega), \tag{4.24}$$

$$\langle RF\rangle_i(\omega) = \gamma_i(\omega)\langle uF\rangle_i(\omega). \tag{4.25}$$

Having derived a close set of the relations between various time correlation functions, we will briefly comment on some of them. First of all, Eq. 4.24 can be rewritten as $\gamma_i(\omega) = \langle Ru\rangle_i(\omega)/\langle uu\rangle_i(\omega)$. This expression is a counterpart of Eq. 4.11, which described the friction coefficient of particle i, where friction originates from the surrounding liquid. Equation 4.22 can be rewritten as $kT/\langle uu\rangle_i(\omega) = \mathrm{i}\omega m_i + \bar{\eta}_i(\omega) + \gamma_i(\omega)$, which simply means that the total friction coefficient (LHS of the above equation) is the sum of inertia (first term on the RHS of the above equation), the L-S friction coefficient (second term on the RHS of the above equation)

and the liquid/liquid (L/L) friction coefficient (third term on the RHS). Typically, for the case of slip boundary conditions, we expect $|\bar{\eta}_i(\omega)| \ll |\gamma_i(\omega)|$. Finally, one should note that Eq. 4.23 is just the Fourier transform of Eq. 4.16 and Eq. 4.23 shows that the fluctuation-dissipation relation is the result of the lack of correlation of the random force R (Eqs. 4.14,4.15) to the velocity and friction force.

We are now ready to derive the final expression for $\bar{\eta}_i$ and $\bar{\eta}$. As Eq. 4.18 relates the L-S friction force-velocity correlation to the mobility of the liquid particle and Eq. 4.20 connects the L-S friction force autocorrelation function to the L-S friction force-velocity correlation, we can rewrite Eq. 4.11 and Eq. 4.12 as

$$\bar{\eta}_i(\omega) = \frac{\langle FF \rangle_i(\omega)}{kT - \langle Fu \rangle_i(\omega)}, \tag{4.26}$$

$$\bar{\eta}(\omega) = \frac{\sum_i \langle FF \rangle_i(\omega)}{SkT(1 - \alpha(\omega))}, \tag{4.27}$$

where $\alpha(\omega) \equiv \langle Fu \rangle_i(\omega)/kT$. At zero frequency $\omega = 0$, one can show from Eq. 4.22 that $\bar{\eta}_i(0)/\gamma_i(0) = \alpha(0)/(1 - \alpha(0))$. For slip boundary conditions, this ratio is expected to be very small, leading to $\alpha(0) \ll 1$, which will be shown later to be true in our simulations. Equation 4.27 is the new Green-Kubo (GK) relation for the macroscopic coefficient of friction coefficient that does not require calculation of the interfacial mobility and can be directly evaluated from EMD simulations. To numerically evaluate Eq. 4.27 at $\omega = 0$, the only parameter one needs to choose by hand is the number density n of interfacial liquid particles, as there is no clear boundary of the L-S interface. Since n enters Eq. 4.27 only through $\alpha(0) = \sum_i \langle Fu \rangle_i(0)/kTSn$, the uncertainty in Eq. 4.27 from n will be suppressed by the fact that $\alpha \ll 1$ or $\bar{\eta}_i \ll \gamma_i$ for a slip boundary condition.

$\bar{\eta}_i$ and $\bar{\eta}$ are in general complex numbers for a finite frequency ω and they become real numbers for $\omega = 0$. It is worth pointing out the macroscopic friction coefficient obtained in this way is not limited to a certain geometry (e.g., the curvature of area S is not required to be zero) since it is not calculated from macroscopic correlation defined on the area S, but from the microscopic correlation that are not dependent on the global geometry. This property allows our method to be applicable to curved interfaces, such as surfaces of nanotubes or even nanoparticles[36].

The GLE formalism, used to derive Eq. 4.27, merits a few additional comments. First of all, the

GLE written in the form of Eq. 4.13 has many applications. For example, it has been utilized to explain the diffusion of impurities and defects in crystals[37], the superionic conductance[38] and the fluctuations of the Josephson supercurrent through a tunneling junction[39;40]. Similar GLE has also been implemented in the Brownian dynamics simulations[41]. The physical meaning of the last term of Eq. 4.13, $F(t)$ varies from case to case. It is important to note that in most of the applications, the memory function $\gamma(t)$ is approximated as a delta function $\gamma\delta(t-t')$, where γ is a constant, not a function of time anymore. Such treatment of coarse graining the memory function constitutes a compromise between a mathematical rigor and practicality of the applications (which requires simple form of the memory function for computational efficiency), because the exact form of the memory function is often difficult or impossible to obtain. Nevertheless, in our case one does not need to know the exact form of the memory function in order to be able to reformulate Eq. 4.11 into Eq. 4.26. Therefore, irrespectively of the exact form the memory function, our GK relation for the coefficient of friction expressed in Eq. 4.27 is formal and exact as long as the GLE given in Eq. 4.13 can formally describe the motion of an interfacial liquid particle. In fact, one can formally construct Eq. 4.13 for $\vec{F} = -\nabla U(\vec{r}$ (where U is an arbitrary external potential) using the projection operator approach[32;33;42]. Proof of this statement is given in the Appendix B. In the derivation of the extended GLE, we found that the memory kernel and the friction coefficient are in general two dimensional tensors. This is not surprising, since due to the perturbation of the solid wall, the memory and the transport coefficient of the interfacial particles could be anisotropic[43–45]. As a result, Eq. 4.13 is generalized as

$$m_i\dot{\vec{u}}_i(t) = -\int_0^t \boldsymbol{\gamma}_i(t-t')\vec{u}_i(t')\,\mathrm{d}t' + \vec{R}_i(t) + \vec{F}_i(t), \tag{4.28}$$

where $\dot{\vec{u}}_i, \vec{u}_i, \vec{R}_i$ and $\vec{F}_i$ are two dimensional vectors that lie parallel to the solid wall and $\boldsymbol{\gamma}_i$ is the tensorial memory function with the generalized fluctuation-dissipation relation $kT\boldsymbol{\gamma}_i(t) = \langle\vec{R}_i(0)\vec{R}_i(t)\rangle$. In the same spirit, Eqs. 4.14, 4.15 are generalized to $\langle\vec{u}_i(0)\vec{R}_i(t)\rangle = \langle\vec{F}_i(0)\vec{R}_i(t)\rangle = 0$ at a finite time t. Consequently, the friction coefficient becomes a tensor and the reformulation of GK relation reads

$$\begin{aligned}\bar{\boldsymbol{\eta}}_i(\omega) &= [kT\boldsymbol{\mu}_i(\omega)]^{-1}\langle\vec{F}\vec{u}\rangle_i(\omega) \\ &= \langle\vec{F}\vec{F}\rangle_i(\omega)[kT\mathbf{I} - \langle\vec{F}\vec{u}\rangle_i(\omega)]^{-1},\end{aligned} \tag{4.29}$$

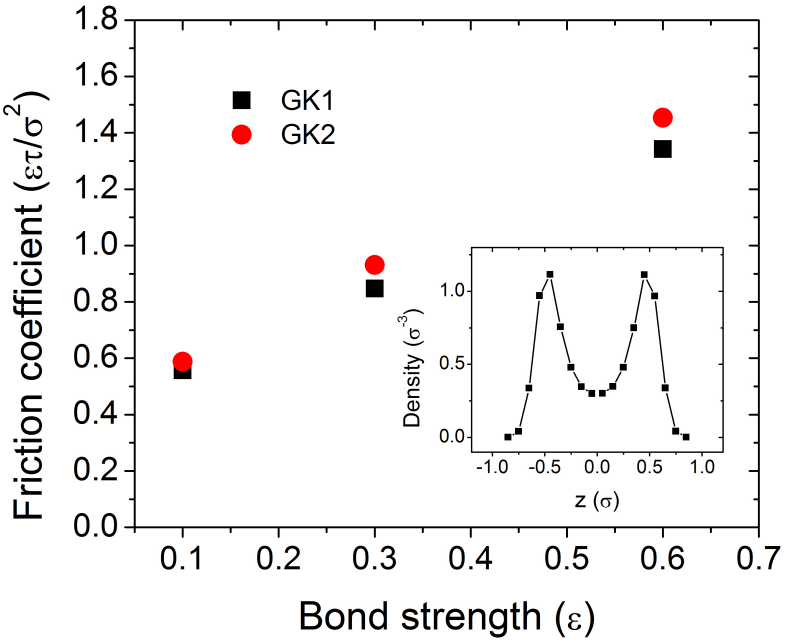

Figure 4.1: Friction coefficients calculated from Eq. 4.12 (the GK relation, GK1) and Eq. 4.27 (the reformulated GK relation by GLE, GK2) calculated as a function of bond strength between liquid and solid atoms. σ is a reduced unit of length, as explained in the main text. Inset: Density profile of a hard-sphere liquid confined between two solid walls located at $z = \pm 1.2\sigma$.

where $\boldsymbol{\mu}_i(\omega) = \langle \vec{u}\vec{u} \rangle_i(\omega)/kT$ is the tensorial mobility. If the x and y axes parallel to the solid wall are chosen to align with the crystallographic symmetry axes of the solid surface, then $\boldsymbol{\gamma}_i$ and $\bar{\boldsymbol{\eta}}_i$ could be diagonalized. For simplicity, we will limit the discussion in the simulation section to such a situation because we choose to adapt this particular alignment. In addition to the formal proof in the Appendix B, the validity of the GLE equation will be further tested against results of MD simulation in the next section.

4.3 MD simulation results and discussions

4.3.1 Simulation test of the Generalized Langevin Equation for interfacial liquid particles

We carried out MD simulations to numerically validate our GK relation. First, in order to test if the extended GLE with the assumption $\langle F(0)R(t) \rangle_i = 0$ captures the physics of interfacial liquid particles or not, we compare predictions of the friction coefficient from Eq. 4.12 and Eq. 4.27. One of the challenges of using Eq. 4.12 was the calculation of local liquid mobility

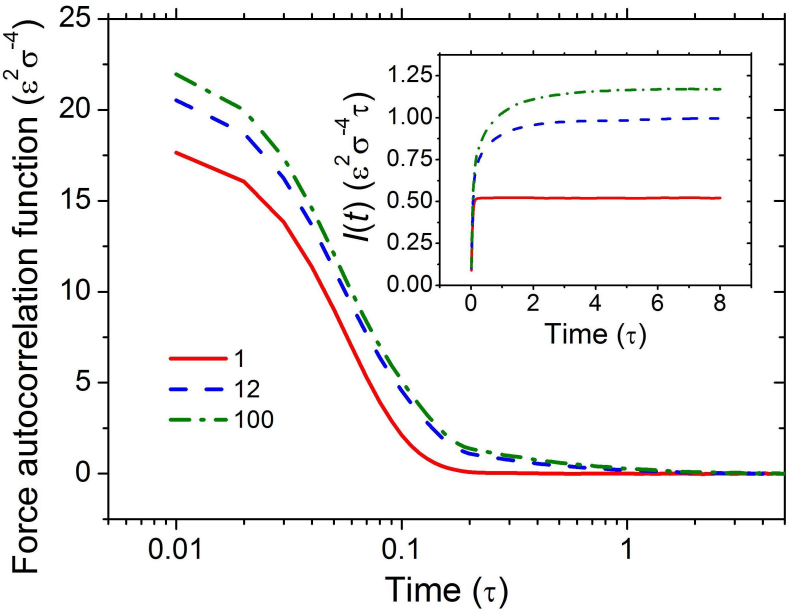

Figure 4.2: L-S frictional force autocorrelation function (FAF) and its time integral $I(t)$ (inset). Solid, dashed, and dotted-dashed lines (red, blue, and green colors online) correspond to the hard-sphere, 12-bead polymer, and 100-bead polymer liquids, respectively. Here the bond strength between liquid particles and the solid is 0.3ϵ.

at the L-S interface. To overcome this challenge, we designed a simulation system, where the liquid is confined between the two solid walls to the extent that almost the entire body of the liquid becomes interfacial (see the inset of Fig. 4.1). The solid walls are face-centered cubic crystals with a constant surface area of $48\sigma \times 48\sigma$, where σ is the unit of length in reduced Lennard Jones (LJ) units. There are 8000 hard-sphere liquid particles confined between the walls. Using this setup, we calculated the friction coefficient from both Eq. 4.12 and Eq. 4.27 and the results are shown in Fig. 4.1. The excellent agreement between the two ways to calculate friction coefficient numerically justified our application of the extended GLE with the form of Eq. 4.13.

4.3.2 Agreement between EMD and NEMD results

The next and most important examination of our proposed GK model is to see if it can predict the friction coefficient measured in a direct way, which in our case is the NEMD method. Explicitly, we calculate the friction coefficient $\bar{\eta}(\omega)$ from the EMD simulations combined with Eq. 4.27 and from NEMD simulations in the limit of low sliding velocities. The simulated

system consists of a liquid confined between two solid walls. The simulation boxes for EMD and NEMD are identical except in EMD the solid walls are stationary, while in NEMD the walls are sliding against each other to build a shear rate in the confined liquid. To ensure that our conclusions are general, we use both, a hard-sphere liquid and a spring-bead polymer melt (for polymer liquid, index i in Eq. 4.27 runs over the beads). We also choose two different lengths of the polymer liquid with the short one being 12 beads and the long one 100 beads per particle. The number of liquid particles in each simulation is 48000, which means 4000 molecules for the 12-bead polymer melts and 480 molecules for the 100-bead polymer melts. The solid walls are again face-centered cubic crystals with a constant surface area of $48\sigma \times 48\sigma$. The distance between the two walls is kept around 20σ, varying with the liquid type to keep zero-pressure conditions. Periodic boundary conditions are applied within the plane of the solid wall. To explore a range of slip boundaries, we choose three different bond strengths $(0.1\epsilon, 0.3\epsilon, 0.6\epsilon)$ between the solid wall and liquid particles, where ϵ is the unit of energy in LJ units. Temperature is kept at 1.1 (in LJ units) during the production run. Temperature is controlled with the Nose-Hoover thermostat coupled only to one direction, which lies within the plane of the solid surface and is perpendicular to the direction of sliding. The time step is set to be 0.002τ, where $\tau = (m\sigma^2/\epsilon)^{1/2}$ and m is mass of the liquid particle in LJ units. For EMD simulation, the production simulation is 5000 time steps long (10τ) while the production simulation of NEMD simulation is as long as 10^6 time steps (2000τ).

It is found in simulations that α in Eq. 4.27 is generally small compared to 1, which, as discussed earlier, is expected in the case of slip boundary conditions. As a result, the autocorrelation of the L-S friction force ($\sum_i \langle F(0)F(t)\rangle_i$) is the dominant contribution to the friction coefficient $\bar{\eta}$. In Fig. 4.2, we show the behavior of this force autocorrelation function (FAF) and its time integral ($I(t) = \frac{1}{S}\int_0^t \sum_i \langle F_i(0)F_i(t')\rangle_{\mathrm{EC}}\,\mathrm{d}t'$) as a function of time. The latter is important for the evaluation of friction coefficient at zero frequency limit, which is of most interest and can be compared directly to our NEMD results. For both, hard-sphere and polymeric liquids the FAF decays dramatically at short time scales and exhibits a hydrodynamic tail at longer time scales. The short time decay largely determines the growth of the time integral $I(t)$ and the hydrodynamic long tail barely contributes to the friction coefficient. One important consequence of this fast decay of FAF and the corresponding fast convergence of its time integral is that calculations of the L-S friction coefficient in EMD are two orders of magnitude faster than the NEMD calculations of the friction coefficient at a single value of the sliding velocity

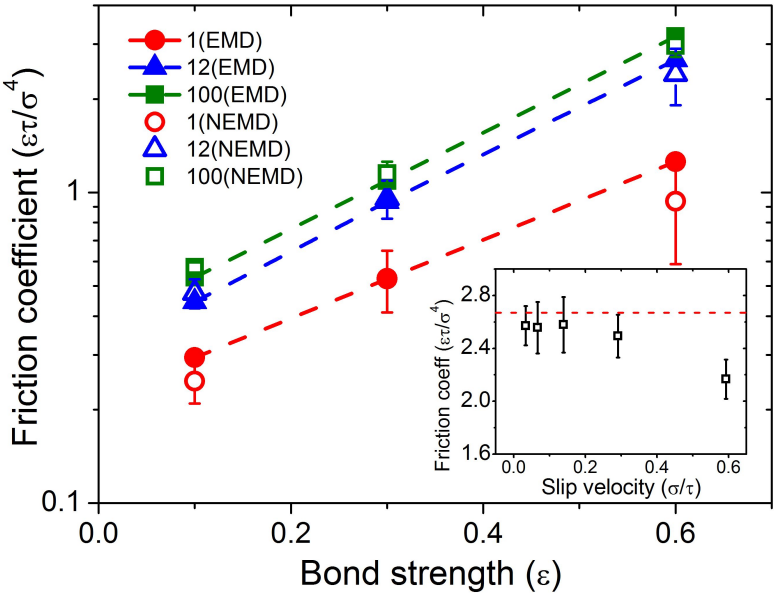

Figure 4.3: Comparison between friction coefficients at zero frequency calculated from EMD (filled symbols) and NEMD (open symbols) simulations as a function of the bond strength between the liquid particles and solid atoms. Circles, triangles, and squared (red, blue, and green colors online) in the main figure correspond to the hard-sphere, 12-bead, and 100-bead liquids, respectively. Data in the inset is calculated for interfacial bond strength of 0.6ϵ for 12-bead polymer melts. The dashed horizontal line in the inset corresponds to the friction coefficient calculated from EMD simulations.

(simulations with multiple values of sliding velocities are needed to determine the low-velocity limit). In general, the convergence of $I(t)$ slows down as the molecular weight of the polymeric liquid increases.

In Fig. 6.7, a comparison is made between the results from EMD and NEMD simulations. Excellent agreement is found between the friction coefficient predicted by our GK relation from EMD results and the friction coefficient calculated from NEMD in the limit of low sliding velocities (shear rates). Convergence of the NEMD simulations to the low velocity limit is illustrated in the inset of the figure. The agreement between EMD and NEMD results is found for all types of liquids considered in our study and for a range of interfacial bond strengths, which indicates that our relationship is universal. We did not show the error bars of the EMD results in Fig. 6.7 as they are smaller than the symbol size. The high efficiency and accuracy of the EMD method based on our GK relation enables a comprehensive exploration of the fundamentals of L-S friction, such as the dependence of the friction coefficient on pressure, wettability, surface morphology[46], liquid confinement[4;25], etc. Here, as an example, we only

briefly discuss the dependence of the friction coefficient on the bond strength between liquid and solid molecules/atoms and on the properties of the liquid. From Fig. 6.7 we can see that $\bar{\eta}$ increases roughly exponentially with the bond strength for a relatively wide range of liquids we tested. For all types of liquid we found that $\bar{\eta}$ in general increases nonlinearly with the length of the polymer chain that the liquid is made of. Interestingly, for the 12-bead and 100-bead polymer melts, the difference in $\bar{\eta}$ is very small. This trend is in consistent with the finding in Ref.[13] that beyond chain lengths of about 10 beads, the molecular weight dependence of the slip length l is dominated by the bulk viscosity η (see Eq. 4.1 for the relation between $\bar{\eta}$, l and η).

Once the friction coefficient $\bar{\eta}$ is known, one can use it to calculate the lateral (i.e., in the plane of the solid wall) mobility μ of the interfacial liquid using Eq. 4.12. We found in our hard-sphere simulation that the μ/μ_0 values for L-S bond strengths of 0.1ϵ, 0.3ϵ, 0.6ϵ are 1.72, 1.38 and 0.86, respectively, where μ_0 stands for the bulk liquid mobility, which is calculated using Eq. 4.9 in a simulation system consisting of liquid only. The observed trend of decreasing interfacial mobility with increasing L-S bond strength is not surprising, but the ability to evaluate this interfacial property can be valuable to a number of other studies, such as those focused on understanding the fundamental nature of hydrophobic interactions[47–49].

4.3.3 Frequency dependent L-S friction coefficient

For any GK relation, one shall be able to get the dynamic transport coefficient from the Fourier transform of the corresponding memory function. Here we demonstrate that our new GK relation provides access to information about dynamic properties of the L-S friction. Knowing the frequency dependent friction coefficient and mobility is of particular importance in high frequency resonators, such as those based on quartz crystal microbalance[50;51]. It is because at high frequencies transport coefficients can significantly deviate from their static (zero frequency) values[52]. From Eq. 4.27 one can extract the frequency dependent friction coefficient by Fourier transforming the time correlation of the friction force. This coefficient connects the frequency dependent L-S friction and the slip velocity, explicitly, $F(\omega) = -\bar{\eta}(\omega)u(\omega)$. At finite frequency, $\bar{\eta}(\omega)$ is in general a complex number, meaning that there exists a phase difference between the friction and slip velocity. Figure 4.4 shows the details of the frequency dependence of the complex friction coefficient $\bar{\eta}(\omega)$. While the real part (solid lines) decreases monotoni-

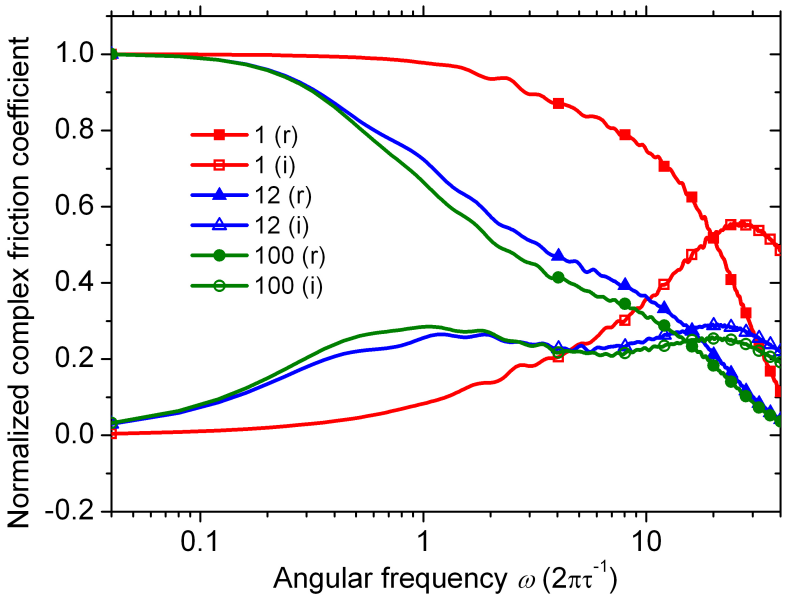

Figure 4.4: Complex friction coefficient $\bar{\eta}(\omega)$ normalized by the zero-frequency value $\bar{\eta}(0)$ as a function of frequency. Solid and dashed lines correspond to the real (r) and imaginary (i) parts of the friction coefficients. Red, blue and green colors represent hard-sphere, 12-bead, and 100-bead liquids, respectively.

cally, two peaks are found in the imaginary part (dashed lines). These peaks correspond to the relaxation times of the two regimes of exponential decays visible in Fig. 4.2 (the first regime extends in time from 0.01τ to 0.1τ and the second regime from 0.1τ to 1τ). In Fig. 4.4, the left peak, which corresponds to the slower structural relaxation, is much higher in the polymeric liquid than in the hard-sphere simple liquid. The positions of peaks in the $\bar{\eta}(\omega)$ plot (Fig. 4.4) depend on the properties of the liquid and these peaks could be used to design sensors based on high-frequency resonators for characterization of soft matter (especially thin films with large slip lengths).

4.3.4 Comparison to the earlier GK relation

Lastly, it is instructive to compare the numerical performance of our model to the one reported earlier by BB in Refs[17;21] and to discuss the differences and similarities between the models. In Fig. 4.5 we plot the behavior of the time integral of two friction force autocorrelation functions (FAFs). In Fig. 4.5(a) we plot $I_1(t) = \frac{1}{SkT(1-\alpha(0))}\int_0^t \sum_i \langle F_i(0)F_i(t')\rangle_{\mathrm{EC}}\,\mathrm{d}t'$, which is a time integral derived in our model to predict the coefficient of friction from EMD. In Fig. 4.5(b) we show $I_2(t) = \frac{1}{SkT}\int_0^t \langle F_{\mathrm{tot}}(0)F_{\mathrm{tot}}(t')\rangle_{\mathrm{EC}}\,\mathrm{d}t'$, which is the equivalent time integral proposed in

Ref.[17;21]. The results are compared to coefficients of friction predicted in NEMD simulations in the limit of low sliding velocities (red dashed lines). One can see that predictions from EMD calculations based on our Green-Kubo relation fall within the range of error bars (grey area) of NEMD calculations. In contrast, the EMD results in Fig. 4.5(b), although on the same order of magnitude, do not agree with the NEMD results very well. In addition, we see that the disagreement becomes worse as the size of the sampling interface increases (i.e., the decay of the integral of the correlation function decays faster). This is the opposite trend than expected given the fact that as the system size approaches the thermodynamic limit (i.e., the the sampling size is increased), the time integral that defines the transport coefficient should decay slower[53–55]. We shall also point out that our GK relation allows a high numerical efficiency. Despite the fact that our simulations based on Eq. 4.27 are one order of magnitude shorter than those based on BB theory and Eq. 4.3, the former approach provides a much smoother well-converged curve than the latter approach does. Specifically, data in Fig. 4.5(a) is obtained in 5,000 time steps, while it takes 50,000 time steps to obtain data in Fig. 4.5(b).

Although it is not the goal of our paper, one can speculate on the possible sources of the discrepancies between the BB model and the results of NEMD simulations. We find that there is a number of assumptions in the derivations of BB model that need to be further justified: (i) In the first derivation in the main text of Ref.[17], an external perturbation Hamiltonian defined with a shear rate and a reference position z_0 was constructed in order to apply the linear response theory and to calculate friction/slip length. As the slip length is constrained by the quantity $z_{wall} - z_0$, where z_{wall} is the position of the solid wall, such a choice of external perturbation could have overspecified the problem. (ii) In the second derivation in the appendix of Ref.[17], contributions from higher (more than 2) order terms of k in the normal direction to the solid wall are ignored, where k is the wave vector. This truncation of higher order terms relies on the assumption that any spatial inhomogeneities are smoothly varying in the hydrodynamic (long time-scale) limit. However, due to the presence of the solid wall, properties of the liquid (e.g., the liquid density and viscosity) can be have pronounced inhomogeneities at the nanometer length scales along the direction normal to the wall surface. Higher order terms with respect to k may be needed to capture such small inhomogeneities. Therefore the approximation of using only second-order terms in the expansion with respect to k needs to be carefully justified. (iii) In the third derivation of the BB formalism in Ref.[21], a Brownian model is utilized to describe the motion of the solid wall. The coefficient of friction between

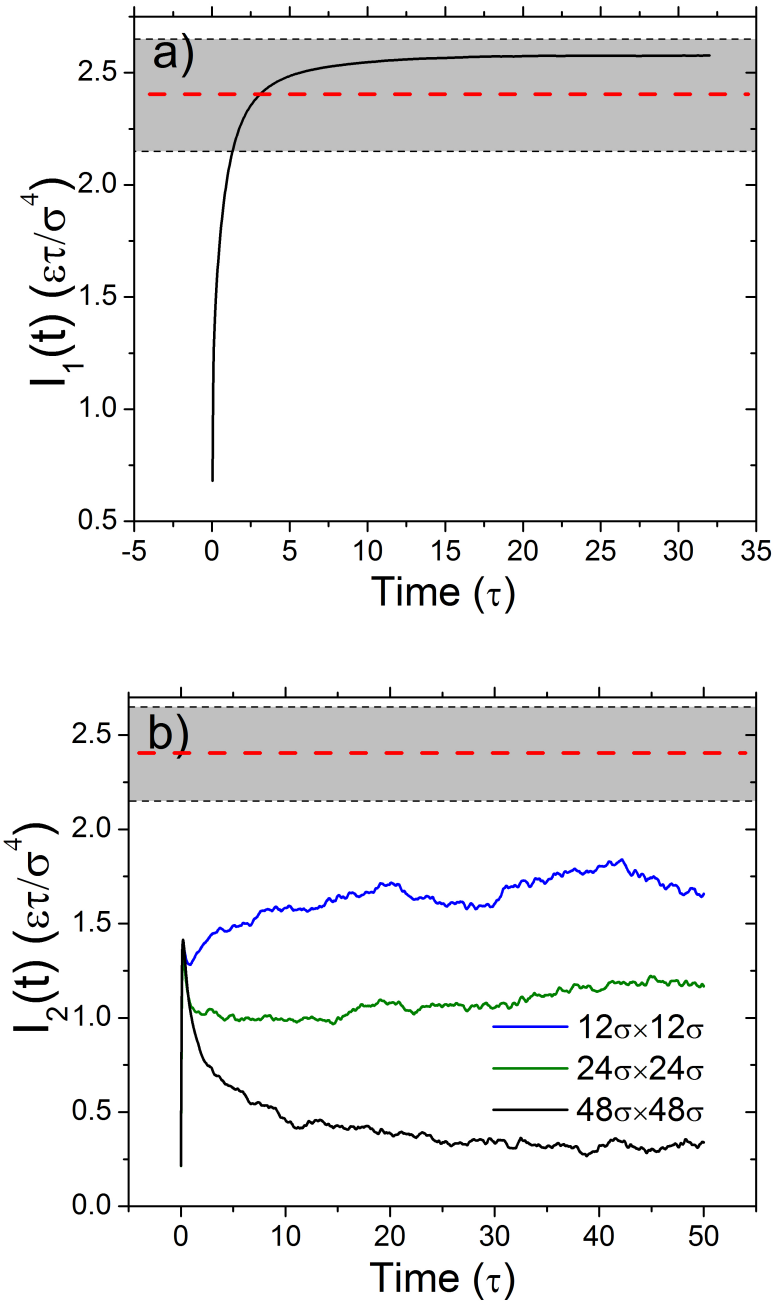

Figure 4.5: Convergence of the time integral of friction force time correlation function (a) proposed in this work and (b) defined in Refs.[17;21]. In Fig. (b), the total friction force is calculated on samples with surface areas of $12\sigma \times 12\sigma$ (blue), $24\sigma \times 24\sigma$ (green), and $48\sigma \times 48\sigma$ (black). The red dashed line represents NEMD prediction in the limit of low velocities. The height of the grey domain corresponds to the size of the error bar. Simulations were performed for a 12-bead polymer melt liqud with the bond strength between the liquid and the solid being 0.6ϵ.

the wall and the liquid is assumed to be equal to the integral of time correlation of the total force experienced by the solid. From the fluctuation-dissipation theorem, one can see that such a relation is only an approximation of the formal one between the friction constant and the random force (see the force correlation section of Ref.[56]). Further test is needed for the assumed approximation when replacing the random force autocorrelation function with the one of the total force.

4.4 Concluding remarks

In conclusion, we have developed a general GK relation for liquid-solid friction and verified its validity by numerical simulations based on the molecular dynamics technique. This new relation provides access to dynamic properties of the L-S friction and allows overcoming the challenge of limited time scales typical for NEMD simulations. We show that in the limit of low shear-rates, the coefficient of friction is not infinite (corresponding to no-slip boundary conditions), but instead it has a finite value. Consequently, the coefficient of friction is an intrinsic property of the system. Friction coefficient was also shown to be a tensor, which implies that in general it can be anisotropic. In addition, the friction coefficient has additive properties, which means it can be calculated locally. Finally, because calculations with the new method are significantly faster (2 to 3 orders of magnitude) than traditional NEMD simulations, our GK relation opens up a new opportunity for computational exploration of L-S friction at molecular level and for rational design of L-S interfaces optimized for their slip and friction.

Bibliography

[1] Navier, C. L. M. H., "Memoire sur les lois du mouvement des fluides," *Mem. Acad. R. Sci. Inst. France*, vol. 6, pp. 389–440, 1823.

[2] Granick, S and Zhu, YX and Lee, H, "Slippery questions about complex fluids flowing past solids," *NATURE MATERIALS*, vol. 2, pp. 221–227, APR 2003.

[3] Neto, C and Evans, DR and Bonaccurso, E and Butt, HJ and Craig, VSJ, "Boundary slip in Newtonian liquids: a review of experimental studies," *REPORTS ON PROGRESS IN PHYSICS*, vol. 68, pp. 2859–2897, DEC 2005.

[4] Ortiz-Young, Deborah and Chiu, Hsiang-Chih and Kim, Suenne and Voitchovsky, Kislon and Riedo, Elisa, "The interplay between apparent viscosity and wettability in nanoconfined water," *NATURE COMMUNICATIONS*, vol. 4, SEP 2013.

[5] Cottin-Bizonne, C and Cross, B and Steinberger, A and Charlaix, E, "Boundary slip on smooth hydrophobic surfaces: Intrinsic effects and possible artifacts," *PHYSICAL REVIEW LETTERS*, vol. 94, FEB 11 2005.

[6] Zhu, YX and Granick, S, "Limits of the hydrodynamic no-slip boundary condition," *PHYSICAL REVIEW LETTERS*, vol. 88, MAR 11 2002.

[7] Pit, R and Hervet, H and Leger, L, "Direct experimental evidence of slip in hexadecane: Solid interfaces," *PHYSICAL REVIEW LETTERS*, vol. 85, pp. 980–983, JUL 31 2000.

[8] Bocquet, Lyderic and Charlaix, Elisabeth, "Nanofluidics, from bulk to interfaces," *CHEMICAL SOCIETY REVIEWS*, vol. 39, no. 3, pp. 1073–1095, 2010.

[9] Schoch, Reto B. and Han, Jongyoon and Renaud, Philippe, "Transport phenomena in nanofluidics," *REVIEWS OF MODERN PHYSICS*, vol. 80, pp. 839–883, JUL-SEP 2008.

[10] Whitesides, George M., "The origins and the future of microfluidics," *NATURE*, vol. 442, pp. 368–373, JUL 27 2006.

[11] Kannam, Sridhar Kumar and Todd, B. D. and Hansen, J. S. and Daivis, Peter J., "How fast does water flow in carbon nanotubes?," *JOURNAL OF CHEMICAL PHYSICS*, vol. 138, p. 323, MAR 7 2013.

[12] Kong, Ling-Ti and Denniston, Colin and Mueser, Martin H., "The crucial role of chemical detail for slip-boundary conditions: molecular dynamics simulations of linear oligomers between sliding aluminum surfaces," *MODELLING AND SIMULATION IN MATERIALS SCIENCE AND ENGINEERING*, vol. 18, APR 2010.

[13] Priezjev, NV and Troian, SM, "Molecular origin and dynamic behavior of slip in sheared polymer films," *PHYSICAL REVIEW LETTERS*, vol. 92, JAN 9 2004.

[14] Thompson, PA and Troian, SM, "A general boundary condition for liquid flow at solid surfaces," *NATURE*, vol. 389, pp. 360–362, SEP 25 1997.

[15] Thompson, PA and Robbins, MO, "Shear-flow near solids - epitaxial order and flow boundary conditions," *PHYSICAL REVIEW A*, vol. 41, pp. 6830–6837, JUN 15 1990.

[16] Delhommelle, Jerome and Cummings, Peter T., "Simulation of friction in nanoconfined fluids for an arbitrarily low shear rate," *Phys. Rev. B*, vol. 72, p. 172201, Nov 2005.

[17] Bocquet, L and Barrat, JL, "Hydrodynamic boundary conditions, correlation-functions, and kubo relations for confined fluids," *PHYSICAL REVIEW E*, vol. 49, pp. 3079–3092, APR 1994.

[18] Petravic, Janka and Harrowell, Peter, "On the equilibrium calculation of the friction coefficient for liquid slip against a wall," *JOURNAL OF CHEMICAL PHYSICS*, vol. 127, NOV 7 2007.

[19] Hansen, J. S. and Todd, B. D. and Daivis, Peter J., "Prediction of fluid velocity slip at solid surfaces," *PHYSICAL REVIEW E*, vol. 84, JUL 25 2011.

[20] Kannam, Sridhar Kumar and Todd, B. D. and Hansen, J. S. and Daivis, Peter J., "Interfacial slip friction at a fluid-solid cylindrical boundary," *JOURNAL OF CHEMICAL PHYSICS*, vol. 136, JUN 28 2012.

[21] Bocquet, Lyderic and Barrat, Jean-Louis, "On the Green-Kubo relationship for the liquid-solid friction coefficient," *JOURNAL OF CHEMICAL PHYSICS*, vol. 139, JUL 28 2013.

[22] Hummer, G and Rasaiah, JC and Noworyta, JP, "Water conduction through the hydrophobic channel of a carbon nanotube," *NATURE*, vol. 414, pp. 188–190, NOV 8 2001.

[23] Majumder, M and Chopra, N and Andrews, R and Hinds, BJ, "Nanoscale hydrodynamics - Enhanced flow in carbon nanotubes," *NATURE*, vol. 438, p. 44, NOV 3 2005.

[24] Shenogin, S and Xue, LP and Ozisik, R and Keblinski, P and Cahill, DG, "Role of thermal boundary resistance on the heat flow in carbon-nanotube composites," *JOURNAL OF APPLIED PHYSICS*, vol. 95, pp. 8136–8144, JUN 15 2004.

[25] Leng, YS and Cummings, PT, "Fluidity of hydration layers nanoconfined between mica surfaces," *PHYSICAL REVIEW LETTERS*, vol. 94, JAN 21 2005.

[26] Priezjev, NV and Darhuber, AA and Troian, SM, "Slip behavior in liquid films on surfaces of patterned wettability: Comparison between continuum and molecular dynamics simulations," *PHYSICAL REVIEW E*, vol. 71, APR 2005.

[27] Denniston, C and Robbins, MO, "Molecular and continuum boundary conditions for a miscible binary fluid," *PHYSICAL REVIEW LETTERS*, vol. 87, OCT 22 2001.

[28] D. A. McQuarrie, *Statistical Mechanics*. University Science Books, 2000.

[29] Sun, Jie and Wang, Wen and Wang, Hua Sheng, "Dependence between velocity slip and temperature jump in shear flows," *JOURNAL OF CHEMICAL PHYSICS*, vol. 138, JUN 21 2013.

[30] Khare, Rajesh and Keblinski, Pawel and Yethiraj, Arun, "Molecular dynamics simulations of heat and momentum transfer at a solid-fluid interface: Relationship between thermal and velocity slip," *INTERNATIONAL JOURNAL OF HEAT AND MASS TRANSFER*, vol. 49, pp. 3401–3407, SEP 2006.

[31] Swartz, ET and Pohl, RO, "Thermal-boundary resistance," *REVIEWS OF MODERN PHYSICS*, vol. 61, pp. 605–668, JUL 1989.

[32] R. Zwanzig, *Nonequilibrium Statistical Mechanics*. Oxford University Press, 2001.

[33] I. Snook, *The Langevin and Generalised Langevin Approach to the Dynamics of Atomic, Polymeric and Colloidal Systems*. ELSEVIER, 2007.

[34] Franosch, Thomas and Grimm, Matthias and Belushkin, Maxim and Mor, Flavio M. and Foffi, Giuseppe and Forro, Laszlo and Jeney, Sylvia, "Resonances arising from hydrodynamic memory in Brownian motion," *NATURE*, vol. 478, pp. 85–88, OCT 6 2011.

[35] Huang, Rongxin and Chavez, Isaac and Taute, Katja M. and Lukic, Branimir and Jeney, Sylvia and Raizen, Mark G. and Florin, Ernst-Ludwig, "Direct observation of the full transition from ballistic to diffusive Brownian motion in a liquid," *NATURE PHYSICS*, vol. 7, pp. 576–580, JUL 2011.

[36] Schmidt, JR and Skinner, JL, "Hydrodynamic boundary conditions, the Stokes-Einstein law, and long-time tails in the Brownian limit," *JOURNAL OF CHEMICAL PHYSICS*, vol. 119, pp. 8062–8068, OCT 15 2003.

[37] Weiner, JH and Forman, RE, "Rate theory for solids .4. Classical brownian-motion model," *PHYSICAL REVIEW B*, vol. 10, no. 2, pp. 315–324, 1974.

[38] Huberman, BA and Sen, PN, "Dielectric response of a superionic conductor," *PHYSICAL REVIEW LETTERS*, vol. 33, no. 23, pp. 1379–1382, 1974.

[39] Stephen, M, "Noise in a driven josephson oscillator," *PHYSICAL REVIEW*, vol. 186, no. 2, pp. 393–397, 1969.

[40] Ambegaokar, V and Halperin, BI, "Voltage due to thermal noise in dc Josephson effect," *PHYSICAL REVIEW LETTERS*, vol. 22, no. 25, pp. 1364–1366, 1969.

[41] ERMAK, DL and MCCAMMON, JA, "BROWNIAN DYNAMICS WITH HYDRODYNAMIC INTERACTIONS," *JOURNAL OF CHEMICAL PHYSICS*, vol. 69, no. 4, pp. 1352–1360, 1978.

[42] B. Berne, *Modern Theoretical Chemistry 6. Statistical Mechanics, Part B, Time-Dependent Processes*. Plenum, 1977.

[43] Bazant, Martin Z. and Vinogradova, Olga I., "Tensorial hydrodynamic slip," *JOURNAL OF FLUID MECHANICS*, vol. 613, pp. 125–134, OCT 25 2008.

[44] Schmieschek, Sebastian and Belyaev, Aleksey V. and Harting, Jens and Vinogradova, Olga I., "Tensorial slip of superhydrophobic channels," *PHYSICAL REVIEW E*, vol. 85, JAN 27 2012.

[45] Priezjev, Nikolai V., "Molecular diffusion and slip boundary conditions at smooth surfaces with periodic and random nanoscale textures," *JOURNAL OF CHEMICAL PHYSICS*, vol. 135, NOV 28 2011.

[46] Tretyakov, Nikita and Mueller, Marcus, "Correlation between surface topography and slippage: a Molecular Dynamics study," *SOFT MATTER*, vol. 9, no. 13, pp. 3613–3623, 2013.

[47] Jamadagni, Sumanth N. and Godawat, Rahul and Garde, Shekhar, "Hydrophobicity of Proteins and Interfaces: Insights from Density Fluctuations," in *ANNUAL REVIEW OF CHEMICAL AND BIOMOLECULAR ENGINEERING, VOL 2* (Prausnitz, JM, ed.), vol. 2 of *Annual Review of Chemical and Biomolecular Engineering*, pp. 147–171, 2011.

[48] Chandler, D, "Interfaces and the driving force of hydrophobic assembly," *NATURE*, vol. 437, pp. 640–647, SEP 29 2005.

[49] Berne, Bruce J. and Weeks, John D. and Zhou, Ruhong, "Dewetting and Hydrophobic Interaction in Physical and Biological Systems," *ANNUAL REVIEW OF PHYSICAL CHEMISTRY*, vol. 60, pp. 85–103, 2009.

[50] Krim, J and Solina, DH and Chiarello, R, "Nanotribology of a kr monolayer - a quartz-crystal microbalance study of atomic-scale friction," *PHYSICAL REVIEW LETTERS*, vol. 66, no. 2, pp. 181–184, 1991.

[51] Dayo, A and Alnasrallah, W and Krim, J, "Superconductivity-dependent sliding friction," *PHYSICAL REVIEW LETTERS*, vol. 80, pp. 1690–1693, FEB 23 1998.

[52] Huang, Kai and Szlufarska, Izabela, "Friction and Slip at the Solid/Liquid Interface in Vibrational Systems," *LANGMUIR*, vol. 28, pp. 17302–17312, DEC 18 2012.

[53] ESPANOL, P and ZUNIGA, I, "FORCE AUTOCORRELATION FUNCTION IN BROWNIAN-MOTION THEORY," *JOURNAL OF CHEMICAL PHYSICS*, vol. 98, pp. 574–580, JAN 1 1993.

[54] Volz, SG and Chen, G, "Molecular-dynamics simulation of thermal conductivity of silicon crystals," *PHYSICAL REVIEW B*, vol. 61, pp. 2651–2656, JAN 15 2000.

[55] Sellan, D. P. and Landry, E. S. and Turney, J. E. and McGaughey, A. J. H. and Amon, C. H., "Size effects in molecular dynamics thermal conductivity predictions," *PHYSICAL REVIEW B*, vol. 81, JUN 21 2010.

[56] Kubo, R, "Fluctuation-dissipation theorem," *REPORTS ON PROGRESS IN PHYSICS*, vol. 29, no. 1, pp. 255–&, 1966.

5 Effect of interfaces on the nearby Brownian motion

5.1 Introduction

Near-boundary Brownian motion is a classic hydrodynamic problem of great importance in a variety of fields, from biophysics to micro-/nanofluidics. However, due to challenges in experimental measurements of near-boundary dynamics, the effect of interfaces on Brownian motion has remained elusive. Here, we discover this effect thanks to μs-long large-scale molecular dynamics (MD) simulations and our newly developed Green-Kubo relation for friction at the liquid-solid interface. Our computer experiment unambiguously reveals that the $t^{-3/2}$ long-time decay of the velocity autocorrelation function (VAF) of a Brownian particle in bulk liquid is replaced by a $t^{-5/2}$ decay near a boundary. We discover a general breakdown of traditional no-slip boundary condition at short time scales and we show that this breakdown has a profound impact on the near-boundary Brownian motion. Our results demonstrate the potential of Brownian-particle based micro-/nano-sonar to probe the local wettability of liquid-solid interfaces.

It is now well known that the VAF of a Brownian particle in a bulk liquid does not decay exponentially as predicted by the Einstein-Ornstein-Uhlenbeck theory[1;2], but instead it follows a $t^{-3/2}$ algebraic decay at the hydrodynamic long-time limit[3]. Such a $t^{-3/2}$ long-time tail, first discovered for neat liquid in the seminal computer experiment by Alder and Wainwright[4], has been recently observed experimentally for single Brownian particle trapped in optical tweezers experiments[5–8]. When the optical trap is stiff enough, the power spectral density (PSD) of the particle's position exhibits a hydrodynamic resonance[6]. The slow VAF decay in time and concomitant resonance in PSD are related to each other by Fourier transform and are both the result of the hydrodynamics coupling between the Brownian particle and bulk liquid. This

coupling is mediated by the vorticity generated by the particle. When the Brownian particle moves toward a boundary and when the particle-generated vortex reaches the boundary (see Fig. 5.1a), it is clear that the hydrodynamic coupling must change, but the question is how.

Since Lorentz[9], theorists have attempted to answer this question from hydrodynamic and lattice-Boltzmann calculations[10–12]. However, consensus has not been reached so far even for the simplest case in which a spherical particle is immersed in Newtonian liquid bounded by a flat surface with no-slip boundary condition (the slip length L_s defined in Fig. 5.1b vanishes). For instance, Berg-Sørensen and Flyvbjerg developed models for PSD, which when Fourier transformed predict a persistent $t^{-3/2}$ long-time tail in VAF near a boundary. This is the same functional form as in a bulk liquid, but with a reduced amplitude[11]. On the other hand, Felderhof derived a model that exhibits an algebraic decay of $t^{-5/2}$ (see Fig. 5.1c) for the same case of a near-boundary particle[12]. Comparisons of these predictions to experimental measurements have only been made in recent years. For instance, Jeney *et al*[13] measured the VAF of a near-boundary Brownian particle trapped with optical tweezers and reported a $t^{-5/2}$ long-time tail. However, a later optical tweezers experiment by Jannasch *et al*[14] observed a reduced magnitude of PSD in the low-frequency (long-time tail) limit and a suppression of a hydrodynamic resonance near a boundary (see Fig. 5.1d), which phenomenon was explained using Flyvbjerg's model with the $t^{-3/2}$ long-time decay of VAF. While contradicting each other, both experiments suffer from large statistical uncertainties in the long-time or low-frequency limit. Therefore so far, experimental findings on the asymptotic behavior of near-boundary Brownian particle have been inconclusive.

MD simulations provide a powerful tool for addressing the above questions, because they do not require *a priori* assumptions about molecular phenomena at the liquid-solid interface[3;15;16]. However, typical MD simulations of dynamic phenomena suffer from the limitations of accessible time scales. Here, we overcome this challenge by using μs-long large-scale MD simulation and our recently developed Green-Kubo (GK) relation for liquid-solid friction[17]. Thanks to this new technique, our simulations are able to measure the boundary condition at the zero shear-rate limit, consistent with the regime explored in the optical tweezers experiments. We study the Brownian motion of a near-boundary nano-particle immersed in approximately half a million solvent molecules. The use of such a large simulation system ensures that finite-size effects (e.g., the effect of the acoustic wave traveling through the entire simulation domain

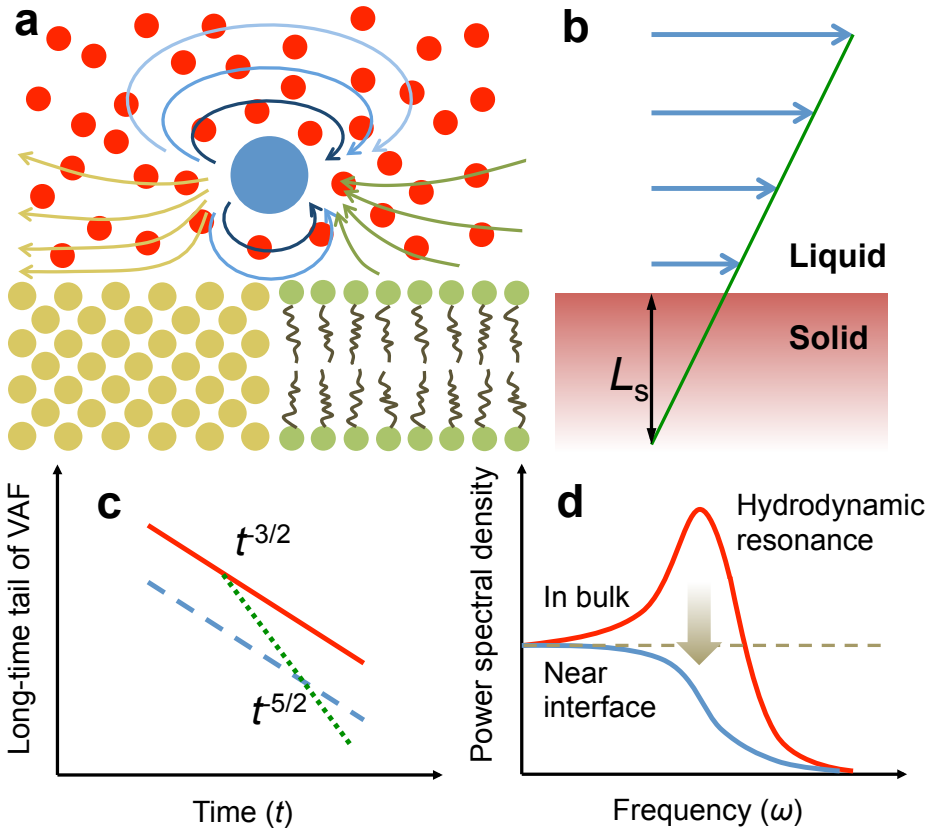

Figure 5.1: Schematic representation of near-boundary Brownian motion and the mysteries. **a**, The presence of the boundary affects the diffusivity of the Brownian particle and its hydrodynamic coupling to the solvent. This effect is expected to be surface-specific and understanding it is useful for advanced sensing applications. **b**, Slip length L_s defined to characterize the boundary condition of a partially wetted surface. **c**, Log-log representation of the long-time tails. According to different theories, the $t^{-3/2}$ long-time tail in bulk liquid (solid red) could be persistent but suppressed (dashed blue) near a boundary, or transition into a $t^{-5/2}$ decay (dotted green). **d**, The resonance peak due to the particle-solvent hydrodynamic coupling in bulk liquid is found to be suppressed as the particle approaches a boundary.

within the time of the measurement) can be excluded. Unlike the optical tweezers experiments that trap the Brownian particle in all three dimensions, we only constrain the particle in the direction perpendicular to the surface by applying a harmonic potential. Therefore the particle performs free Brownian motion parallel to the surface and its long-time tail in the lateral directions will not be truncated nor affected by parallel constraints, as it can happen in experiment[13]. By assigning strong interaction between solvent and solid atoms, we create a fully wetted surface that exhibits no slip in the long-time limit, which is consistent with typical experimental situations.

5.2 Simulation method

We construct a liquid box (see Fig. 5.2) with dimensions of $64\sigma \times 64\sigma \times 128\sigma$ confined between two identical solid walls, where σ is the unit of length in reduced Lennard Jones (LJ) units. Two-dimensional periodic boundary conditions are applied in the plane parallel to the interface. One spherical Brownian particle is immersed in the fluid near each interface and it is constrained by external harmonic potential along the direction normal to the interface. The average distance between the nano-particle and the solid wall is kept at 5σ. The nano-particles interact with the solvent with a shifted LJ potential:

$$\phi(r) = 4\epsilon\left[\left(\frac{\sigma}{r-a}\right)^{12} - \left(\frac{\sigma}{r-a}\right)^{6}\right], \tag{5.1}$$

where a is the shifted distance of the potential, which defines the size of the nano-particle. We choose $a = 2\sigma$ in our system which yields a hydrodynamic radius of $R = 3\sigma$ suggested by literature[18]. The solvent-interface interaction and solvent-solvent interaction employ the same potential but with $a = 0$. The interaction strength is set to 1ϵ for solute-solvent and solvent-solvent interactions. For no-slip boundary condition, we choose the liquid-solid interaction strength to be 0.8ϵ. A smaller value of 0.2ϵ is used for slip boundary condition. Since confinement effects may be more severe in the presence of large slip length, to avoid any such effects we use a box of size $48\sigma \times 48\sigma \times 200\sigma$ for the study of poorly wetted surfaces. A liquid cube with three-dimensional PBC is also built to study the unbounded Brownian motion as a reference. There are around 4×10^5 solvent particles in the bounded system and around 2×10^5 in the unbounded system.

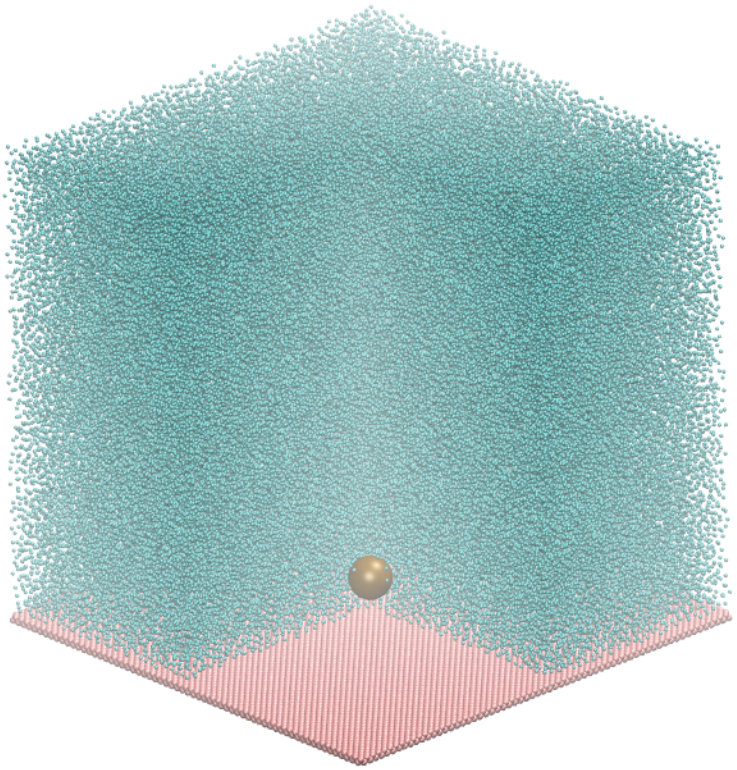

Figure 5.2: Simulation box. Half of the box is shown here. Red: solid wall atoms. Cyan: solvent particles. Brown: nano-particle.

In order to have sufficient statistics in estimating long-time tails, we choose solvent density of 0.693, which has a low shear viscosity of 1.1 in reduced units. The time step is set to be 0.005τ, where $\tau = (m\sigma^2/\epsilon)^{1/2}$ and m is the mass of the liquid particle in LJ units. To obtain a good signal/noise ratio, 5000 independent simulations with different starting configurations are carried out to obtain each near-boundary VAF curve. Each independent simulation consists of 10^5 timesteps in the production stage. A cumulative 5×10^8 timesteps corresponds to a total sampling time of $2.5 \times 10^6\tau$ in reduced units or around 5μs in real units for each VAF. Error bars are calculated as a standard deviation from an average over 5000 independent simulations. During the relaxation before data production, temperature is kept at 1.1 (in LJ units) and it is controlled with the Nose-Hoover thermostat. The thermostat is removed in the production stage. MD simulations are carried out using the LAMMPS software package[19].

5.3 Results

5.3.1 Effect of interface on diffusivity

Before studying the VAF of the Brownian motion, we first demonstrate that the hydrodynamic theories can quantitatively predict the diffusion coefficient for a motion of a nano-particle in our simulations. Although the functional form of the near-boundary VAF of Brownian motion remains controversial, it is generally agreed that near a fully wetted solid surface (which yields a no-slip boundary condition), the diffusion of a Brownian particle is slower than in bulk. Such boundary confinement was first demonstrated by Lorentz[9], who predicted a reduced diffusion constant $D_w = D_b(1 - \frac{9R}{16h})$, where R is the hydrodynamic radius of the particle[18] and h is the distance between the center of the particle and the solid wall. In this equation, $D_b = \frac{kT}{c\pi\eta R}$ is the Einstein-Stokes relation[1] for Brownian diffusion constant in bulk liquid, with kT being the thermal energy and η the viscosity of liquid. The constant c is equal to 4 when there is no friction between the nano-particle and the surrounding solvent[3;18] (as is the case in our simulations). In our simulations, we use mean-square-displacement (MSD) to calculate the diffusion coefficient of a nano-particle that is 125 times heavier than solvent and with $R = 3\sigma$, where σ is the reduced unit of distance employed in simulation and corresponds to a few angstroms in real units. To ensure that we truly test the effect of boundary confinement, we constrain our nano-particle's motion very close to the wall with $h = 5\sigma$. Diffusion coefficients (which are time integrals of VAF) calculated both in bulk and near a liquid-solid interface are shown in the inset of Fig. 5.3 and they are compared to the predictions of Lorentz and Eintstein-Stokes theories, respectively. In general, a good agreement is reached between simulations and theory, which demonstrates that our simulations of near-boundary motion capture correctly the physics that is already well established.

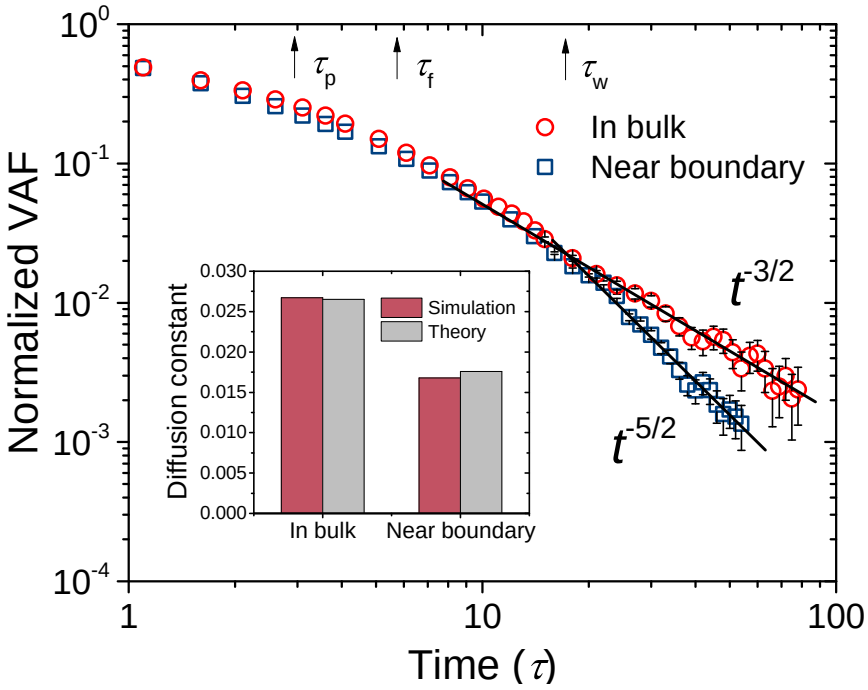

Figure 5.3: Diffusion constant and VAF of Brownian particle. Log-log plot of the VAFs (normalized by its value at time zero) of a nano-particle in bulk liquid (circles) and near a static no-slip boundary (squares). Solid black lines labeled $t^{-3/2}$ and $t^{-5/2}$ are added to guide the eye. In the inset the diffusion coefficients of the nano-particle in bulk and near boundary are compared to their theoretical predications at Brownian limit. τ_p is a characteristic time scale equal to m_p/γ, where m_p is the mass of the particle and γ is the Stokes friction coefficient. τ_f and τ_w are defined in the main text. Data points represent averages over 2000 independent simulations for bulk VAF and 5000 for near-boundary VAF. The error bars are obtained as a standard deviation from these averages and are not shown for VAF at short time scale as they are smaller than the symbol sizes.

5.3.2 Effect of interface on velocity autocorrelation function

We now focus on the highly debated VAF of the nano-particle, since this function encodes the full dynamic information about the Brownian motion. We first discuss the results in bulk liquid, shown with red circles in Fig. 5.3. After time $\tau_f = R^2\rho/\eta = 5.7$ (where τ_f is the time scale of developing a vortex comparable to the size of the particle and ρ is the liquid density) the VAF decays according to the functional form $A_b t^{-3/2}$ and it is the long-time tail behavior. According to theory[20], the amplitude A_b of the bulk $t^{-3/2}$ long-time tail depends only on the shear viscosity of the liquid

$$A_b = \frac{kT\rho^{1/2}}{12(\pi\eta)^{3/2}}. \tag{5.2}$$

By fitting the long-time tail measured in our simulations and using Eq. 5.2, we find the liquid shear viscosity of 1.0. This value is in a good agreement with $\eta = 1.1$ measured directly from simulations using the following GK relation[21]

$$\eta = \frac{V}{kT}\int_0^\infty \langle P_{xy}(t)P_{xy}(0)\rangle \mathrm{d}t, \tag{5.3}$$

where V is the volume of bulk liquid and P_{xy} represents off-diagonal (shear) components of the stress tensor.

When the nano-particle approaches a boundary, the VAF starts to deviate strongly from the bulk VAF after $\tau_w = h^2\rho/\eta = 15.8$, which is the time when particle-induced vorticity reaches the interface. As shown in Fig 5.3, in the long-time limit, the VAF of the near-boundary nano-particle exhibits a $t^{-5/2}$ behavior, instead of the $t^{-3/2}$ behavior observed in the bulk. Our finding conclusively demonstrates a transition from the bulk $t^{-3/2}$ long-time tail (red solid line in Fig. 5.1c) to a $t^{-5/2}$ one (green dotted line in Fig. 5.1c) near a boundary and excludes the possibility of a persistent but reduced $t^{-3/2}$ long-time tail (blue dashed line in Fig. 5.1c), previously proposed in literature[11].

In order for the VAF to serve as a local probe of the nano-particle's environment[6], it is important to understand not only the qualitative trend in VAF, but also the impact of the environment on VAF's amplitude. The amplitude A_w of the $t^{-5/2}$ long-time tail near a boundary has been recently derived by Felderhof using hydrodynamic theories[12]

$$A_w = CkT\frac{R^2}{\eta}\left(\frac{\rho}{4\pi\eta}\right)^{3/2}, \tag{5.4}$$

where $C = h^2/R^2 - 5/9 + 2\rho_p/9\rho + (1-\rho_p/\rho)R/8h$ with ρ_p being the density of the Brownian particle. Unlike A_b, which depends only on the liquid properties, A_w is also dependent on the density ρ_p of the particle. To test the predictive power of Eq. 5.4, we keep the size of our nano-particle constant and we increase its mass from 125 to 375 in reduced units (corresponding to solute-to-solvent density ratios of $1.6 - 4.8$). In Fig. 5.4, we plot the VAFs of the Brownian particles with varying masses and in the inset we compare the amplitudes of the $t^{-5/2}$ long-time tails to the theoretical predictions. While a reasonably good match between simulation and theory is achieved for the most massive particle, a remarkable deviation is found for the lightest particle. Specifically, the numerical result in the case of small nano-particle is

significantly suppressed compared to the theoretical value. Such discrepancy suggests that the time scale separation between the solute and solvent dynamics may not be sufficient for the lightest particle.

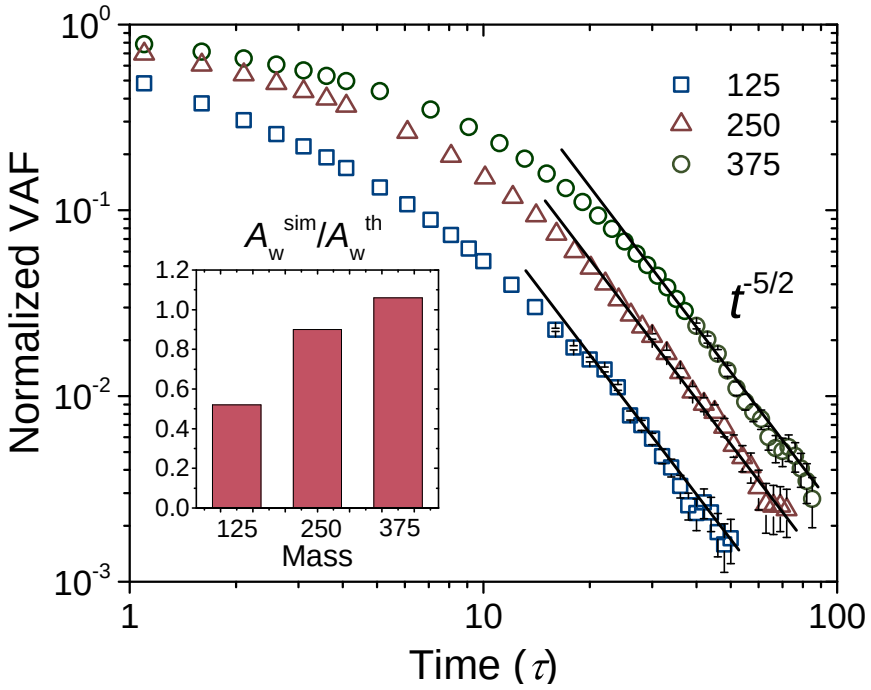

Figure 5.4: VAFs of nano-particles with varying masses. Log-log plot of the VAFs (normalized by its value at time zero) of nano-particles ($R = 3\sigma$) with different masses near a static no-slip boundary. Solid black lines are added to guide the eye for the $t^{-5/2}$ asymptotic behavior (see Appendix C for the quality of fittings). The inset shows the ratio of amplitudes of the $t^{-5/2}$ long-time tail measured in simulations (A_w^{sim}) and predicted by theory (A_w^{th}). Data points represent averages over 5000 independent simulations and error bars are obtained as a standard deviation from these averages.

5.3.3 Relaxation of boundary condition

An extreme separation of time scales between the fast relaxation of solvent transport coefficients and the slow Brownian motion of a nano-particle is a major assumption of hydrodynamic theories of simple viscous liquids (such as the theory underlying Eq. 5.4). We will test if this assumption holds for the case of the lightest nano-particle, for which the hydrodynamic theory was shown to break down (Fig. 5.4). First we calculate the relaxation of the fluid viscosity η using Eq. 5.3 in the absence of an interface. Specifically, the relaxation of η is characterized by the stress autocorrelation function (SAF). As shown in Fig. 5.5, the relaxation of SAF

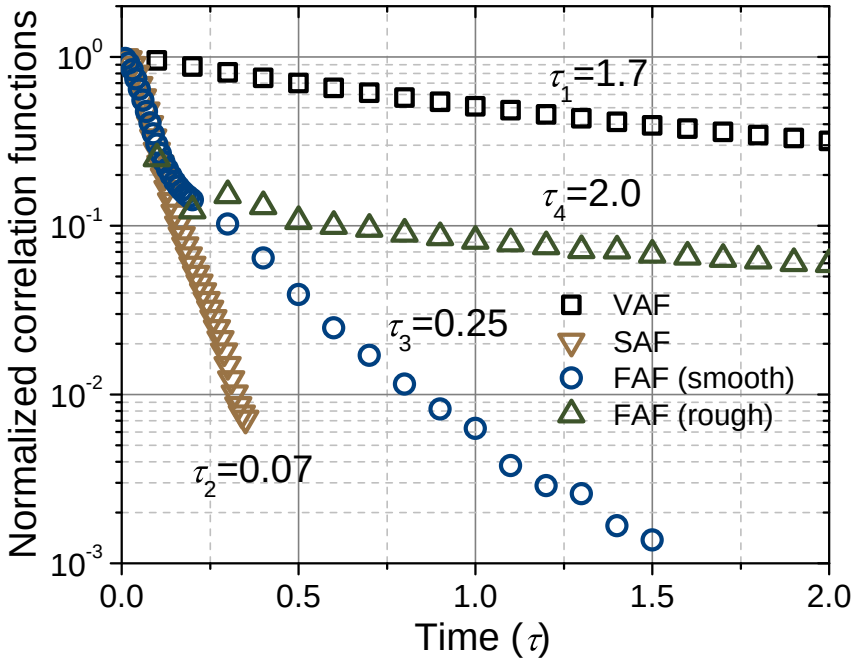

Figure 5.5: Correlation functions. he normalized correlation functions that characterize the memories of different transport coefficients: the VAF for diffusion (squares), the SAF (stress autocorrelation function) for viscosity (down triangles), the FAF (force autocorrelation function) for liquid-solid friction coefficient on atomically smooth surface (circles) and on rough surface (squares). Calculations are shown for $m_p = 125$.

is significantly faster than the velocity relaxation of the lightest nano-particle at short time scale. Fitted to simple exponential decays, the solute relaxation time $\tau_1 \approx 1.7$ is indeed well separated from the viscosity relaxation time $\tau_2 \approx 0.07$. This separation of τ_1 and τ_2 explains why simulation results agree well with theory for the Brownian motion of this nano-particle in bulk liquid (see Fig. 5.3). On the other hand, it suggests that there is some other physics that is responsible for the discrepancy observed near a boundary and reported in Fig. 5.4. One possibility is the relaxation of the boundary, which means that the boundary condition may be time-dependent. Although existence of such dynamic boundary has been hypothesized in literature[22–24], it has never been demonstrated before due to the challenges in calculating it theoretically and in measuring it experimentally. Consequently, a static boundary is assumed in most hydrodynamic theories.

Here, we can test the hypothesis of boundary relaxation directly by calculating the friction coefficient $\bar{\eta}$ at the liquid-solid interface. To do that, we use our recently developed GK

relation, which reads[17]

$$\bar{\eta} = \frac{1}{SkT(1-\alpha)} \int_0^\infty \sum_i \langle F(t)F(0)\rangle_i \mathrm{d}t. \tag{5.5}$$

where F is the friction force on the solvent particle i exerted by the solid surface, α is the ensemble-averaged ratio between F and the total force experienced by interfacial solvent particles, and the sum is taken over all solvent molecules above surface area S. Similarly to the viscosity, the boundary relaxation can be characterized by the friction force autocorrelation function (FAF) in Eq. 5.5. As shown in Fig. 5.5, the FAF initially follows the same relaxation trend as the SAF, but then it transitions to a slower exponential decay with a relaxation time $\tau_3 \approx 0.25$. The slow decay corresponds to a collective relaxation of structure of the first liquid layer near the surface. This result means that the onset of boundary conditions is not instantaneous, but instead it takes time to develop. More specifically, even in the case of atomically smooth and fully wetted liquid-solid interfaces with high friction at long time scales (a so-called static no-slip boundary), there can be a reduced friction and some slip present at shorter time scales. Consequently, a Brownian particle can experience a transition from partial-slip to no-slip boundary condition, which means that slip and the boundary condition are inherently dynamic properties. Such a dynamic picture of boundary condition is consistent with earlier observations of the dependence of slip length on shear rate[15;22;25] and frequency[17;26].

The presence of reduced friction (or partial slip) at short time scales means that the liquid-solid coupling is weaker and in this regime the VAF of a Brownian particle decays slower (i.e., has a higher amplitude) than expected for static no-slip boundary conditions. Since the calculated zero-frequency diffusion constant (equal to the time integral of VAF) is the same as theoretically predicted for static no-slip boundary (see the inset in Fig. 5.3), the amplitude of long-time VAF has to be reduced to compensate for the short-time increase of the amplitude. Note that the contribution of the long-time tail to the diffusivity is relatively small compared to the short-time VAF, and therefore a strong reduction at long-time scale is needed to compensate for the change in the short-time scale due to the boundary relaxation. In Ref.[24], by assuming a simple Debye relaxation of the boundary condition, Felderhof found that boundary relaxation at 0.1 μs can have a strong effect on the near-boundary VAF over the time scale of 10 μs. A large delay in the manifestation of a short-time boundary relaxation is also observed in our simulations. The suppression of VAF amplitude in the long-time regime (which we have shown to be due

to the dynamic nature of boundary conditions) is consistent with the idea that hydrodynamic resonance shown in Fig. 5.1d would be suppressed near an interface. Specifically, as shown in Ref.[27] PSD and VAF are related to each other via Fourier transform and the smaller the magnitude of VAF, the smaller the amplitude of the resonance. Since the magnitude of VAF is smaller near a boundary than in the bulk (see Fig. 5.3), it follows that the resonance will be suppressed for a particle near a boundary. This resonance suppression has been previously observed in experiments by Jannasch *et al*[14] and it was attributed as a reduction of VAF amplitude with $t^{-3/2}$. Future work is needed to include a dynamic boundary discovered in our study in hydrodynamic theories to determine if experiments of Jannasch *et al* agree with the $t^{-5/2}$ decay with reduced amplitude predicted by our study. On the other hand, our findings of the $t^{-5/2}$ decay in the long-time regime of VAF are consistent with optical tweezers experiments of Jeney *et al*[13].

When considering relaxation of boundary conditions for engineering surfaces one should take into account surface roughness, topology and even the possibility of forming air bubbles[24]. To shed light on this important issue, we introduce roughness by constructing a patterned surface with the pattern width of 8σ and height of 1σ and we investigate how this roughness impacts boundary relaxation. Surprisingly we find that although the roughness is very small in our simulations, it has a dramatic effect on relaxation time. As shown in Fig. 5.5, the boundary (FAF) relaxation time on a rough surface is much slower ($\tau_4 \approx 2.0$) than on a smooth surface ($\tau_3 \approx 0.25$). Since roughness of typical engineering surfaces can be often much higher than the one considered here, such roughness is expected to strongly affect nearby Brownian particles even with micrometer sizes. This sensitivity could be used as a potential probe of the local properties of liquid-solid interfaces, such as wettability and and slip length (see Appendix C).

5.4 Further discussion and conclusion

Here we briefly discuss the Lorentz approximation or point approximation. It is worth noting that Lorentz's calculation is based on the assumption of $a = R/h \ll 1$, where R is the hydrodynamic radius of the particle and h is the distance between the particle and the solid surface. Such calculation only deals with the first order perturbation from a on the diffusion constant. A more general theory taking into account higher order terms has been developed later by Faxén[28] who found that the near-boundary diffusion constant can be written as:

$D_w = D_b(1 - 9/16a + 1/8a^3 - 45/256a^4 - 1/16a^5 + \ldots)$. Interestingly, there is no second order term in this equation and the third and fourth order terms have opposite signs, which means it is possible for them to cancel each other. Indeed, we found that in our case (where $a = 0.6$) Faxén's exact solution with up to the fifth order term in a gives a result within 0.1% of the Lorentz's approximation. Therefore the good agreement between our simulations and Lorentz' theoretical prediction shown in Fig. 2 also holds for comparison with the more exact Faxén's theory.

Regarding the VAF of the Brownian particle, present theories including the one developed by Felderhof have not yet taken into account the higher order terms in a. Within the first order approximation, different theories predicted qualitatively different asymptotic behaviors ($t^{-3/2}$ vs $t^{-5/2}$ long-time tail near a boundary). For example, in the theory of Felderhof[12], the leading term of the VAF is $A_w t^{-5/2}$ with the coefficient A_w being a function of a. Including higher order terms in a will not change the order in the leading term of time (the power of the long-time tail), but it could modify the coefficient A_w (the amplitude of the tail). Nevertheless, it is possible that the contribution from higher order terms of a is small, as a similar cancellation could happen as in the case of diffusion constant. Our simulation result for the heaviest nano-particle also suggests that the Lorentz approximation (with only first order term in a) works reasonably well in predicting the VAF of Brownian motion close to the boundary.

So far our analysis have been restricted to the case of static no-slip boundaries. Here we show the effect of a partially-wetted surface on the nearby Brownian motion. Since partially-wetted surface exhibits slip at long-time scales when the interfacial solvents are fully relaxed, we refer to it as a static slip boundary condition. We simulate such a boundary condition by using weak liquid-solid interaction strength ϵ=0.2, which corresponds to a finite slip length L_s of 23σ. The VAF of a nano-particle near such a partially-wetted surface is shown in Fig. S2 and it is compared to the ones near wetted surface and in bulk. We find that although for partially-wetted surface the long-time tail of VAF still follows $t^{-5/2}$, the amplitude of VAF increases as compared to no-slip boundary conditions. In the limit of perfect slip ($L_s \to \infty$), some theories[10] predicted a $t^{-3/2}$ long-time tail. Our results suggest that there could be a transition from the $t^{-5/2}$ to $t^{-3/2}$ as the slip length increases.

In conclusion, our discovery of the long-time behavior of VAF directly from molecular simulations addresses a long-standing debate in the field regarding the nature of the long-time tail

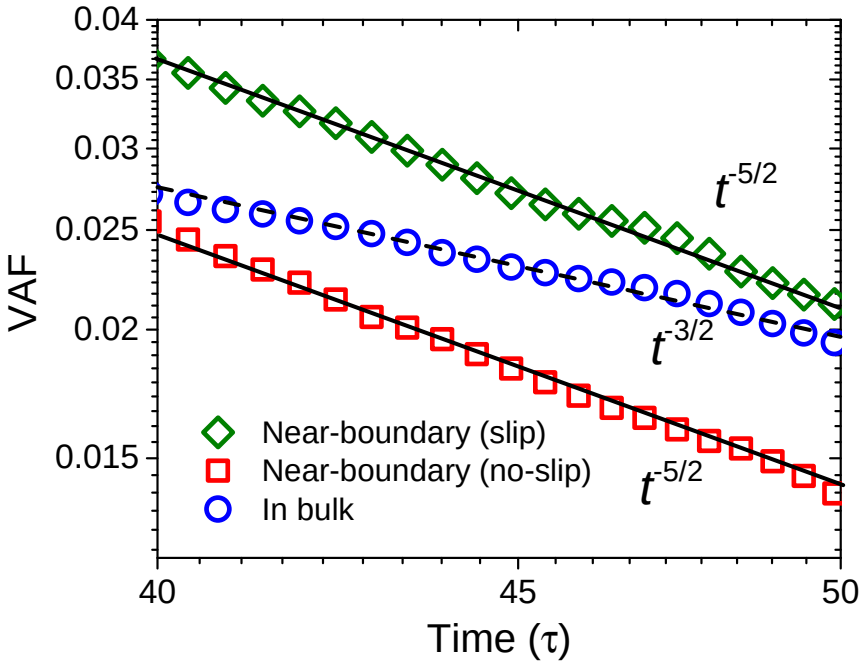

Figure 5.6: VAF Long-time tails of a nano-particle ($R = 3$, $M = 375$) near boundaries ($h = 5\sigma$) with different boundary conditions. Solid black line ($t^{-5/2}$ decay) and dashed black line ($t^{-3/2}$ decay) are added to guide the eye.

near interfaces. We demonstrate that liquid-solid boundary conditions are inherently dynamic and that relaxation of this boundary is important to account for in hydrodynamic theories and in models of micro-/nanoflow, even for perfectly smooth surfaces and even in the case of nominally no-slip boundaries. While it had been known that interfaces disrupt the vortex generated by a nearby Brownian particle, we have shown that interfacial relaxation hinders the vortex backflow even further and this effect is expected to be significant for submicron solutes such as nano-particles and biomolecules. The sensitivity of Brownian motion to the nearby L-S interface can enable advanced sensing applications, such as probing of local properties of L-S interfaces by monitoring the VAF of a single Brownian particle[6] or by measuring the two-point correlation function between two test particles.[29]

Bibliography

[1] Einstein, A., "Über die von der molekularkinetischen Theorie der Wärme geforderte Bewegung von in ruhenden Flüssigkeiten suspendierten Teilchen," *Annalen der Physik*, vol. 322, no. 8, pp. 549–560, 1905.

[2] Uhlenbeck, G.E. and Ornstein, L.S., "Theory of Brownian motion," *Physical Review*, vol. 36, pp. 823–840, 1930.

[3] J. P. Boon and S. Yip, *Molecular hydrodynamics*. Dover Publications, 2013.

[4] Alder, BJ and Wainwrig.TE, "DECAY OF VELOCITY AUTOCORRELATION FUNCTION," *PHYSICAL REVIEW A*, vol. 1, no. 1, p. 18, 1970.

[5] Li, Tongcang and Kheifets, Simon and Medellin, David and Raizen, Mark G., "Measurement of the Instantaneous Velocity of a Brownian Particle," *SCIENCE*, vol. 328, pp. 1673–1675, JUN 25 2010.

[6] Franosch, Thomas and Grimm, Matthias and Belushkin, Maxim and Mor, Flavio M. and Foffi, Giuseppe and Forro, Laszlo and Jeney, Sylvia, "Resonances arising from hydrodynamic memory in Brownian motion," *NATURE*, vol. 478, pp. 85–88, OCT 6 2011.

[7] Huang, Rongxin and Chavez, Isaac and Taute, Katja M. and Lukic, Branimir and Jeney, Sylvia and Raizen, Mark G. and Florin, Ernst-Ludwig, "Direct observation of the full transition from ballistic to diffusive Brownian motion in a liquid," *NATURE PHYSICS*, vol. 7, pp. 576–580, JUL 2011.

[8] Kheifets, Simon and Simha, Akarsh and Melin, Kevin and Li, Tongcang and Raizen, Mark G., "Observation of Brownian Motion in Liquids at Short Times: Instantaneous Velocity and Memory Loss," *SCIENCE*, vol. 343, pp. 1493–1496, MAR 28 2014.

[9] H. A. Lorentz, *Abhandlungen über Theoretische Physik*. Teubner Verlag, 1907.

[10] Pagonabarraga, I and Hagen, MHJ and Lowe, CP and Frenkel, D, "Algebraic decay of velocity fluctuations near a wall," *PHYSICAL REVIEW E*, vol. 58, pp. 7288–7295, DEC 1998.

[11] Berg-Sorensen, K and Flyvbjerg, H, "Power spectrum analysis for optical tweezers," *REVIEW OF SCIENTIFIC INSTRUMENTS*, vol. 75, pp. 594–612, MAR 2004.

[12] Felderhof, BU, "Effect of the wall on the velocity autocorrelation function and long-time tail of Brownian motion," *JOURNAL OF PHYSICAL CHEMISTRY B*, vol. 109, pp. 21406–21412, NOV 17 2005.

[13] Jeney, Sylvia and Lukic, Branimir and Kraus, Jonas A. and Franosch, Thomas and Forro, Laszlo, "Anisotropic memory effects in confined colloidal diffusion," *PHYSICAL REVIEW LETTERS*, vol. 100, p. 240604, JUN 20 2008.

[14] Jannasch, Anita and Mahamdeh, Mohammed and Schaeffer, Erik, "Inertial Effects of a Small Brownian Particle Cause a Colored Power Spectral Density of Thermal Noise," *PHYSICAL REVIEW LETTERS*, vol. 107, p. 228301, NOV 21 2011.

[15] Thompson, PA and Troian, SM, "A general boundary condition for liquid flow at solid surfaces," *NATURE*, vol. 389, pp. 360–362, SEP 25 1997.

[16] Kong, Ling-Ti and Denniston, Colin and Müser, Martin H., "The crucial role of chemical detail for slip-boundary conditions: molecular dynamics simulations of linear oligomers between sliding aluminum surfaces," *MODELLING AND SIMULATION IN MATERIALS SCIENCE AND ENGINEERING*, vol. 18, p. 034004, APR 2010.

[17] Huang, Kai and Szlufarska, Izabela, "Green-Kubo relation for friction at liquid-solid interfaces," *PHYSICAL REVIEW E*, vol. 89, p. 032119, MAR 18 2014.

[18] Schmidt, JR and Skinner, JL, "Hydrodynamic boundary conditions, the Stokes-Einstein law, and long-time tails in the Brownian limit," *JOURNAL OF CHEMICAL PHYSICS*, vol. 119, pp. 8062–8068, OCT 15 2003.

[19] http://lammps.sandia.gov/.

[20] Clercx, HJH and Schram, PPJM, "Brownian PARTICLES IN SHEAR-FLOW AND HARMONIC POTENTIALS - A STUDY OF LONG-TIME TAILS," *PHYSICAL REVIEW A*, vol. 46, pp. 1942–1950, AUG 15 1992.

[21] D. A. McQuarrie, *Statistical Mechanics*. University Science Books, 2000.

[22] Granick, S and Zhu, YX and Lee, H, "Slippery questions about complex fluids flowing past solids," *NATURE MATERIALS*, vol. 2, pp. 221–227, APR 2003.

[23] Lauga, E and Brenner, MP, "Dynamic mechanisms for apparent slip on hydrophobic surfaces," *PHYSICAL REVIEW E*, vol. 70, AUG 2004.

[24] Felderhof, B. U., "Hydrodynamic force on a particle oscillating in a viscous fluid near a wall with dynamic partial-slip boundary condition," *PHYSICAL REVIEW E*, vol. 85, APR 3 2012.

[25] Choi, CH and Westin, KJA and Breuer, KS, "Apparent slip flows in hydrophilic and hydrophobic microchannels," *PHYSICS OF FLUIDS*, vol. 15, pp. 2897–2902, OCT 2003.

[26] Huang, Kai and Szlufarska, Izabela, "Friction and Slip at the Solid/Liquid Interface in Vibrational Systems," *LANGMUIR*, vol. 28, pp. 17302–17312, DEC 18 2012.

[27] Felderhof, B. U., "Spectrum of position fluctuations of a Brownian particle bound in a harmonic trap near a plane wall," *JOURNAL OF CHEMICAL PHYSICS*, vol. 136, p. 144701, APR 14 2012.

[28] Faxén, H *Ark. Mat. Astron. Fys*, vol. 17, no. 27, p. 1, 1923.

[29] Zhang, Wei and Chen, Song and Li, Na and Zhang, Jia Zheng and Chen, Wei, "Correlated Diffusion of Colloidal Particles near a Liquid-Liquid Interface," *PLOS ONE*, vol. 9, JAN 20 2014.

6 Comparison between free and immobilized ion effects on hydrophobic interactions

6.1 Introduction

Hydrophobic interactions have been recognized as a key driving force for water-mediated self-assembly processes[1–6] such as protein folding and micelle formation. Because of the ubiquitous nature of ions in biological environments, much research has been dedicated to understanding the effects of specific ions on hydrophobic interactions[7]. While previous studies were mostly focused on the effects of soluble salts, a less explored effect (although of similar importance) is that of proximally immobilized ions. Immobilized charged or polar residues are often present on surfaces of macromolecules, where they are distributed within or are adjacent to nonpolar domains. The impact of these residues on hydrophobicity of the neighboring domains is key to understanding hydrophobic interactions in complex biological environments. Recent measurements based on the atomic force microscopy (AFM)[8;9] have revealed that the strength of hydrophobic interactions can be modulated by the presence of proximally immobilized ions. This effect was found to be sensitive to the three dimensional nano-patterning of the charged and non-polar groups[10] and the specific charge (ion) type. Interestingly, the measurable effects of proximally immobilized ions were interpreted to extend over one nanometer in distance, i.e., they are long-range. This finding is in contrast to the recently reported[11;12] short-range nature (i.e., limited to the first ionic hydration shell) of the specific ion effects of soluble salts. The above AFM experiments raise a number of new questions related to specific ions effects. Do the specific proximally immobilized ions follow the same ranking as a function of ion size (Hofmeister order)[13] as free ions? For the same type of ion, how does its influence change when it is transformed from a free ion to a proximally immobilized ion? Without the freedom for ion segregation or depletion from the non-polar domain, what is the molecular origin of the

effects of proximally immobilized ions on hydrophobic interactions?

As a first step towards providing insights into these questions, we report MD simulations of hydrophobic interactions between a non-polar surface and a non-polar or amphiphilic molecule in the presence of proximal charges or free ions. Inspired by the experimental studies that use oligo β-peptide[14–16] that exhibits a well-defined helical conformation, we perform our simulations with a model nano-rod that has a number of key features in common with the experimental system. Specifically, our nano-rod has a well-defined shape and side groups that can be arranged to mimic globally amphiphilic (GA) and non-gobally amphiphilic (*iso*-GA) oligo-β-peptides. In addition, we construct a reference hydrophobic (HP) nano-rod with all side groups being non-polar. There is no corresponding purely hydrophobic β-peptide studied in experiment as it would be impractical to purify such molecules due to their physical properties. Nevertheless, such HP nano-rods in simulation serve as a useful reference system, allowing us to evaluate the effects of proximally immobilized ions and soluble salts.

In the remainder of this paper, we present potential of mean force (PMF) calculations of the model nano-rods near a non-polar plate. We first explore the interaction between an HP nano-rod and the extended non-polar plate as a reference system. We discuss the structure of the PMFs and thermodynamics of the hydrophobic interaction. We then investigate the effect of free ions (dissolved salts) by adding alkali halide salts to modify the hydrophobic interaction involving the HP nano-rod. We analyze the water structure and dynamics near the nano-rod, in search for a potential descriptor of the specific free ion effect. We revisit the anomalous effect of lithium and use controlled simulations to investigate different hypotheses for molecular origin of this anomaly. To study the effect of immobilized ions, we replace some of the non-polar side groups of the HP nano-rod by ionic groups. We construct both *iso*-GA and GA nano-rods to explore the effect of surface nano-patterns. For the GA nano-rods, we further study the specific effects of immobilized ions which are long-ranged in nature. Finally, we compare the immobilized and the free ion effects and discuss the origins of their differences.

6.2 Molecular Model and Simulation Methodology

All MD simulations are performed using the GROMACS software package[17] with explicit solvent since the details of water structuring are key to accurate modeling of hydrophobic

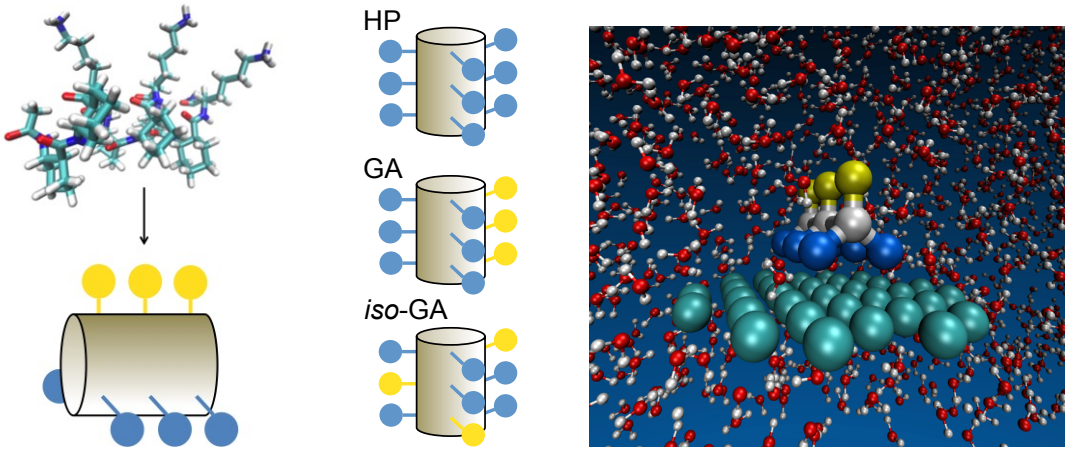

Figure 6.1: Coarse-graining of a β-peptide into a nano-rod with three surface nano-patterns: hydrophobic (HP), globally amphiphilic (GA) and non-globally amphiphilic (*iso*-GA). The nano-rod is immersed in water and interacts with an extended non-polar surface. Coarse-grained sites of the non-polar surface are shown in cyan. Non-polar side groups of the nano-rod are shown in blue, backbone in white, and the immobilized ions in yellow. The backbone refers to the coarse-grained residues to which the functional groups are attached.

interactions. We use the SPC/E force field[18] to model water. Long-range electrostatic interactions are calculated using the particle mesh Ewald (PME) method. All hydrogen bonds are constrained through the LINCS[19] algorithm to enable a simulation time step of 2 fs. The non-polar surface is modeled by 31 Lennard-Jones (LJ) particles arranged into a flat plate. The particles are arranged in a triangular lattice with a lattice constant of 0.32 nm. The same LJ particles (except for their different arrangement) are used to represent the non-polar groups of the nano-rod, whereas the ionic groups are modeled as monoatomic ions. Each of the nine side groups of the nano-rod is bonded to one of the three backbone residues of the molecule and the side group-backbone-side group angles are 120 degree. The backbone residues do not interact with water since they are buried inside the peptide, but their presence allows us to arrange the functional groups in a controlled manner, resembling the rigid helical structure of β-peptide.

As shown in Fig. 6.1, we construct nano-rods with three different nano-patterns: HP, GA and *iso*-GA. Each nano-rod resembles a triangular prism that is approximately 1 nm long. Each edge of the triangular side has a length of approximately 0.5 nm. Similar coarse-grained models have been used in earlier simulations of the self-assembly of β-peptides[20], but in that case implicit solvent was used. To model the proximal ion effects, we use hypothetical halide ions as ionic

Table 6.1: Parameters of the Lennard-Jones potential. H: hydrogen atom of water, O: oxygen atom of water, BB: coarse-grained backbone atom of nano-rod, NS: coarse-grained non-polar site of nano-rod, PC: coarse-grained immobilized ionic group of nano-rod, ES: coarse-grained hydrophobic atom of the extended surface. * symbol refers to atom types that are different from the ones before the hyphen symbol

Atom types	ϵ (kJ/mol)	σ(Å)
H-*	0.0	0.0
BB-*	0.0	0.0
NS-O	0.6	3.52
ES-O	0.6	3.52
NS-ES	0.1	4.0
PC-ES	0.1	4.0

side groups tethered to the coarse-grained backbone of the nano-rod. These immobilized halide ions have the same charge and size as the free halide ions to allow a better comparison between immobilized and free ion effects. We model both immobilized and free ions with the OPLS force field (parameters of this force field can be found in Ref [21]). Lorentz-Berthelot mixing rules are applied to generate LJ parameters between different types of atoms. Other LJ parameters used in our study are listed in Table 6.1. The cut-off distance for the LJ interaction and for short-range Coulomb interaction is 1.2 nm. The strength of the hydrophobic interaction between the nano-rod and the extended surface is largely determined by the parameter ϵ of the LJ potential for interactions between the non-polar site (NS) of the nano-rod and the oxygen atom of water, as well as between the extended nonpolar surface (ES) and the oxygen atom of water. We chose ϵ for NS-O and ES-O to be 0.6 kJ/mol, which represents a typical hydrophobicity of hydrocarbon molecules[22]. The nano-rod and non-polar surface are solvated in a 2.5 nm×2.5 nm×6 nm water box (around 1100 water molecules). By carrying out two sets of simulations (with three counter-ions added or absent from the solutions) we found that such counter-ions have a negligible effect on the calculated free energy, indicating that the effect of highly dilute counter-ions and their interaction with immobilized ions can be reasonably neglected. When investigating free ion effects, 1 molar concentration (approximately 80 ions) of various alkali halides is added to the solution. Such concentration has been used in previous simulation work to study the free ion effect and in past simulations the Hofmeister ordering of free ions was found to be independent of the concentration of ions for neutral non-polar hydrophobes[23;24].

We use the umbrella sampling method to calculate the PMF between each nano-rod and non-polar surface. We define the reaction coordinate to be the z projection of the distance be-

tween the second backbone atom (in the middle of the nano-rod) and the non-polar surface, where z direction is perpendicular to the surface. The separation between neighboring sampling windows is 0.05 nm and the spring constant of the external harmonic constraint is 4000 $\mathrm{kJ/mol \cdot nm^2}$. The PMF reported in the main text corresponds to nano-rods that can freely rotate. In addition we have carried out controlled simulations where the rotational degree of freedom is forbidden (details in Appendix D). We found that the rotation of the molecules does not impact the qualitative conclusions reported in this study. We have calculated uncertainties in PMF using the bootstrapping method[25]. Other methods for calculating uncertainties in PMF have also been reported in literature[26]. A 20 ns sampling time for each PMF calculation allowed us to reach an uncertainty smaller than 0.1 kcal/mol. In our simulations, the system is first relaxed for 1 ns at 300K and 1 atmosphere using constant pressure constant temperature ensemble with coupling constants τ=1 ps for both the thermostat and the barostat. The velocity rescaling thermostat is used for temperature coupling and the Berendsen barostat with the compressibility of 4.5×10^5 $\mathrm{bar^{-1}}$ is used for pressure coupling.

6.3 Results and Discussion

6.3.1 Hydrophobic interaction between HP nano-rod and non-polar plate

Before exploring the specific ion effects, we first study the hydrophobic interaction between a HP nano-rod and an extended non-polar surface as a reference system. Free ion effect can be studied by adding salts to the reference system, whereas proximal charge effect can be investigated by replacing some of the non-polar sites with ionic groups. The PMFs of the hydrophobic interactions for the reference system at different temperatures are plotted in Fig. 6.2. It is interesting that the overall free energy landscape shown here is more complicated than energy landscapes reported for the interactions between two non-polar solutes of simple shapes[22;23]. While there is only one contact minimum in the attractive part of the PMF in the case of simple solutes, our PMF has two minima (except at temperature higher than 325K). Specifically, in addition to the primary contact minimum near 0.5 nm, we have a weak secondary minimum near 0.76 nm. The two minima correspond to two energetically favorable configurations of the nano-rod/plate contacts as shown in the insets of Fig. 6.2. Since there is no electrostatic interaction between the nano-rod and the non-polar surface and the assigned

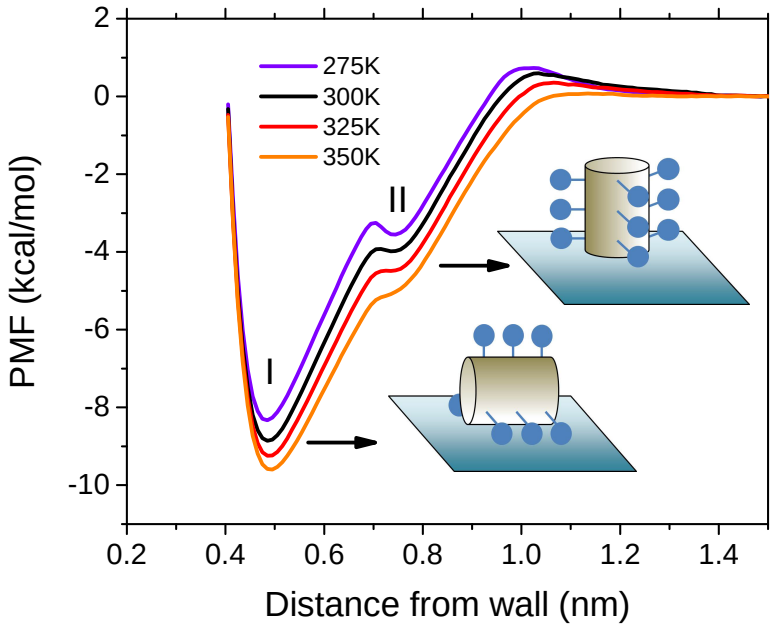

Figure 6.2: Hyrophobic interaction of HP nano-rod as a reference -rods at different temperatures.

van der Waals interaction is very weak (see Table 6.1), the attractive part of the PMF is largely due to the water-mediated hydrophobic interaction. Therefore, these two contact minima are both hydrophobic in nature.

It is known that the thermodynamics of the hydrophobic hydration is size dependent[27;28]. Since the hydrophobic interaction in our system is between a small molecule (nano-rod) and a large surface (non-polar plate), it is interesting to ask what is the thermodynamic driving force of such interaction. According to the partition of the free energy, $\Delta G = \Delta H - T\Delta S$ (where H is enthalpy, T is temperature and S is entropy), the temperature dependence in Fig. 6.2 is indicative of a positive entropy change during the process of association between the nano-rod and the non-polar wall. At $T = 300$K we estimate (based on the free energy difference between $T = 275$K and $T = 325$K) the contribution to the free energy ($-T\Delta S$) to be -5.4 ± 0.9kcal/mol, which is more than half of the total free energy change $\Delta G = -8.8$kcal/mol. The remainder of the free energy change is due to a reduction of enthalpy ($\Delta H = -3.4$kcal/mol) associated with the interaction. Therefore, the interaction between the HP nano-rod and the non-polar plate is favorable both in entropy and enthalpy. Recall that the association of two macroscopic non-polar surfaces is purely enthalpy driven and association of two small hydrophobes is purely driven by entropy. Our results demonstrate that both of these driving forces (entropy increase

and enthalpy reduction) can be present in a mixed system comprised of a small molecule and a large surface. Additional information on the thermodynamic driving force will be presented when discussing Fig. 6.5.

6.3.2 Free ion effects

We now investigate the specific ion effects on the interaction between the nano-rods and the non-polar plate, starting with free ions. The ordering of free ions with respect to their effect on hydrophobic interactions (the so-called Hofmeister series), have been extensively studied in literature[23;24] and can be used to test of our simulations. Simulations of free ion effects also allows a direct comparison with the immobilized ion effects that will be discussed later.

Here we investigate the free ion (dissolved salt) effect by carrying out simulations of the interactions between the HP nano-rod and the non-polar plate in the presence of alkali halide salts (NaF, NaCl, NaI, LiCl, CsCl) at modest molar concentration (1M). Before showing the results, we shall however emphasize that the ordering of the Hofmeister series is not trivially determined by the properties of the ions, but also depends on the solute surface[24]. For example, the ordering of ions that change the solubility of proteins with a net positive charge can be reversed if the protein becomes negatively charged. As in this paper we are dealing with hydrophobic interaction between charge neutral surfaces, we will use the term Hofmeister series to refer to ordering of ions in the presence of charge neutral hydrophobes. Such Hofmeister series for halide anions with respect to their salting-out ability is $I^- < Br^- < Cl^- < F^-$[24]. For alkali cations, the corresponding ranking is $Cs^+ < Li^+ < K^+ < Na^+$[24].

Figure 6.3 shows the PMFs of the interaction between the nano-rod and the hydrophobic plate in the presence of different salts. As Na^+ and Cl^- take positions in the middle of the Hofmeister series and the long-range cooperative ion effects are believed to be small at low and moderate concentrations[11;12], it is reasonable to assume that the effect of sodium halide (alkali chloride) mainly reflects the specific effect of the halide anions (alkali cations). Comparisons within the sodium halide series and alkali chloride series in Fig. 6.3 show that the strength of hydrophobic interaction follows the orders of NaI<NaCl<NaF and LiCl≈CsCl <NaCl. Therefore we can rank halide anions and alkali cations as $I^-<Cl^-<F^-$ and $Li^+\approx Cs^+<Na^+$ in their salting-out effects. Such orderings agree with previous reports of Hofmeister series for non-polar solutes ($I^-<Br^-<Cl^-<F^-$, $Cs^+<Li^+<K^+<Na^+$) very well[24].

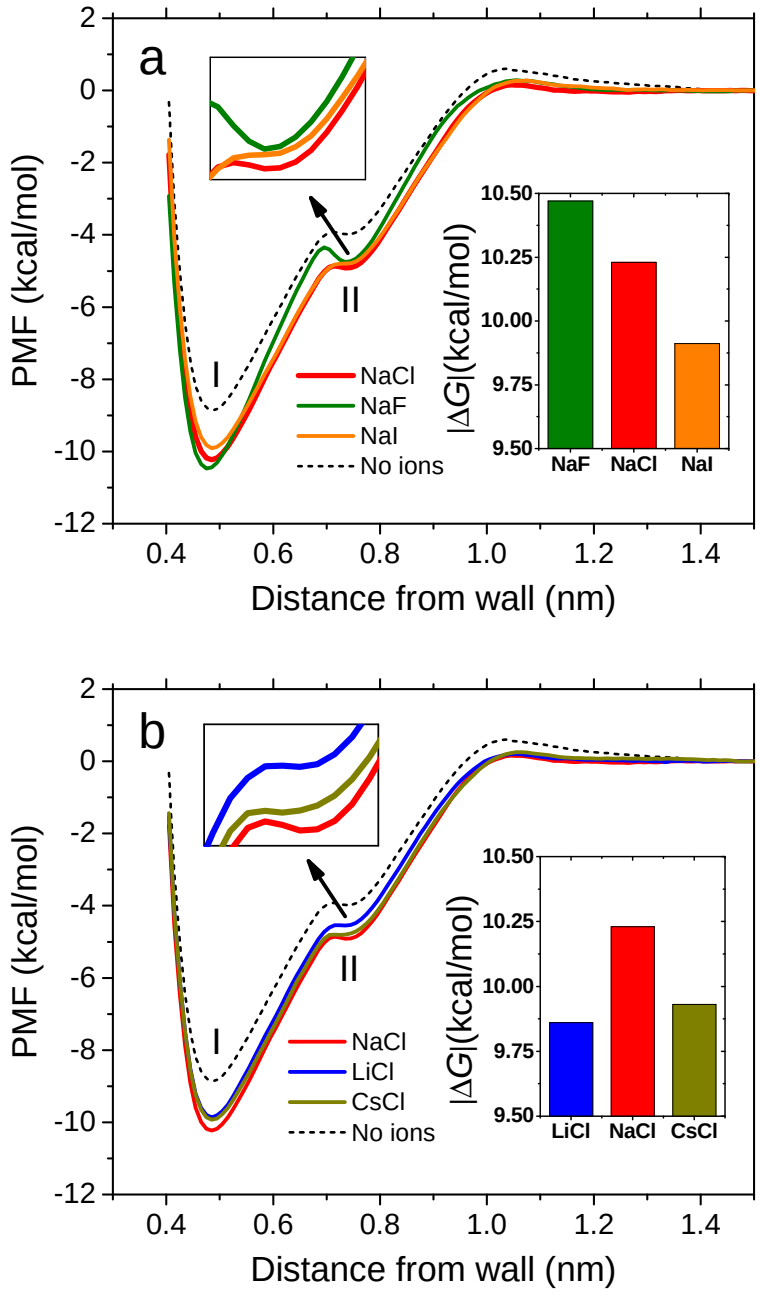

Figure 6.3: PMF curves of hydrophobic interaction in the presence of dissolved (a) sodium halide and (b) alkali chloride. The black curve represents the results from a reference system of a HP nano-rod in water in the absence of any free ions or immoblized ions. Primary contact depth plotted in the insets is defined as the absolute value of the difference in PMF between the depth of the primary contact minimum and the reference state where the nano-rod and the surface are separated from each other.

To shed more light on the molecular origin of the Hofmester ranking of free ions, and inspired by the work of Garde and coworkers[29], we examine the structure and dynamics of the hydrating water around the HP nano-rod by analyzing the water radial distribution function (RDF) and its time-dependent fluctuation in the presence of different salts (see Appendix D). Here, the fluctuation of the water density is not merely a measure of the uncertainty of density, but more importantly it is an indicator of the dynamics of water in the hydration shells. For all systems examined in our simulations, we found the RDF of water around the HP nano-rod to be insensitive to the identity of the salts. In contrast, the fluctuation of the RDF is strongly affected by salts. More interestingly, the ion-modulated RDF fluctuation is well correlated with the ion-modulated strength of the hydrophobic interaction ($|\Delta G|$) with an approximate linear relationship as shown in Fig. 6.4.

The only significant deviation from this linearity comes from the LiCl salt (see the point labeled LiCl(clustered) in Fig. 6.4). Anomalous behavior of Li^+ has been previously noted in literature. Specifically, while the positions of ions in the Hofmeister series can often be correlated with ion size, lithium ion was found to be an exception to this trend[23;24]. Two different ways to rationalize the anomaly of Li^+ have been proposed. Thomas and Elcock[23] postulated that this anomaly is primarily due to clustering between lithium atoms and counter-ions. On the other hand Schwierz *et al*[24] argued that the anomaly of lithium can be explained by its large effective size if one considers the rigid first hydration shell to be part of the ion. To determine the primary mechanism responsible for the lithium anomaly in our simulations, we carried out an additional calculation of $|\Delta G|$ for LiCl salt solution with a constraint on lithium cations such that Li^+ cannot form clusters with chloride anions. The result of this calculation is labeled in Fig. 6.4 as LiCl(dissolved). Interestingly, the salting-out effect (quantified by $|\Delta G|$) of dissociated LiCl is weaker than that of NaCl and NaF and it is stronger than the effect of NaI and CsCl. In other words, even for fully dissolved Li^+, its effect on hydrophobic interaction does not correlate with its bare ionic size. Instead, as shown in Fig. 6.4 the effect of dissociated LiC salt follows the same linear trend as other salts, demonstrating that the strength of hydrophobic interactions $|\Delta G|$ is correlated with RDF fluctuations of water around the nano-rod. These results reveal that while the clustering can contribute to the anomaly of lithium, the primary reason for this anomaly is the large effective size of this ion[24]. It has been shown in recent literature[11;12;30–33] that large ions (with low charge densities) tend to accelerate the reorientation of water. In this light, our simulation observation of the large RDF fluctuation of water in the presence of Li^+

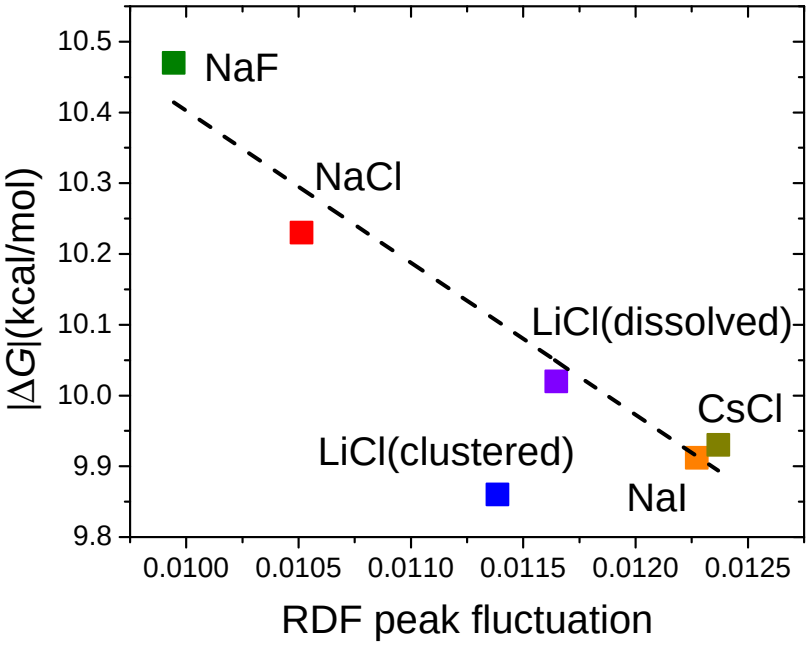

Figure 6.4: Correlation between the strength of hydrophobic interaction in the presence of salts and the RDF fluctuation in the hydration shell of a nano-rod. RDF peak fluctuation is defined as the maximum of the water density fluctuation near the nano-rod.

is consistent with the hypothesis that Li^+ has a large effective ionic size (see more details in Appendix D).

Our conclusion that water fluctuations are a better indicator of hydrophobicity align with the prior results reported by Garde and coworkers[29] for flat surfaces. We demonstrate that these conclusions apply to curved surfaces and more complex molecular structures.

6.3.3 Immobilized ion effects

Now we turn to the effects of immobilized ions. It has been reported that GA and *iso*-GA β-peptides self-assemble into different structures[10], which reflects interactions mediated by the different arrangements of functional groups on the two types of molecules[20;34–38]. Recent AFM single-molecule force spectroscopy measurements[8] revealed that the adhesive forces between β-peptides and non-polar surfaces depend on the nature of the nano-patterns formed by functional groups on the β-peptides. Inspired by these experiments, our first goal here is to understand how nano-scale chemical patterns affect intermolecular interactions and how these interactions can be modulated by immobilized ions. To this end, we calculate the PMF between a non-

polar plate and nano-rods with different nanoscale patterns. For amphiphilic nano-rods, we use hypothetical Cl^- ions (see method section) as the proximally immobilized ions in both GA and *iso*-GA patterns.

The PMF profiles for these two types of nano-rods are shown in Fig. 6.5a together with a reference PMF (without immobilized ions). All PMF curves are shifted so that the reference state (corresponding to the nano-rod not interacting with the surfaces) has zero free energy. The GA nano-rod interacts with the surface in such a way that six of the nano-rod's non-polar sites face the surface and three of its ionic sites point away from the surface, similarly to the contact type I of the HP nano-rod shown in Fig. 6.2. This arrangement minimizes the exposure of non-polar sites to water and thereby maximizes hydrophobic interaction. For nano-rod with the GA pattern, the primary contact minimum is still pronounced, but it is reduced as compared to the contact minimum for the HP nano-rod. The second minimum, which was observed for the HP nano-rod, disappears in the case of the GA pattern. In contrast, the PMF of the *iso*-GA pattern has a very shallow contact minimum of type II and is largely repulsive in the regime where the primary minimum (corresponding to configuration I) would occur. Although it is possible for the *iso*-GA nano-rod to align itself so that up to four of its non-polar sites face the surface, it is clear that the strength of hydrophobic interaction does not simply scale with the number of non-polar sites that face the surface. The striking difference in the PMF of the GA and the *iso*-GA nano-rods reflects the distinct hydration status of the two molecules in water. More specifically, we find that hydrophobic interaction can be effectively destroyed by adding proximally immobilized ions between non-polar sites. Consequently, our results demonstrate that the hydrophobic interaction is a result of the collective behavior of hydrating water molecules and it is not a simple function of the surface area of non-polar domains. This conclusion is generally consistent with the AFM measurement by Acevedo *et al*[8], although in the experiments a non-vanishing pull-off force persisted in the case of *iso*-GA β-peptide. This force was established to be electrostatic in nature due to the non-polar surface accumulating an excess negative charge when immersed in water. The immobilized ion effect in the *iso*-GA nano-rod is similar to the one recently reported in MD simulations by Acharya *et al*[39] where it was shown that polar groups in the middle of a flat non-polar domain can substantially modulate hydrophobic interactions. Our results extend Acharya *et al*'s conclusion for polar groups to immobilized ions, and from a flat geometry to a nano-rod.

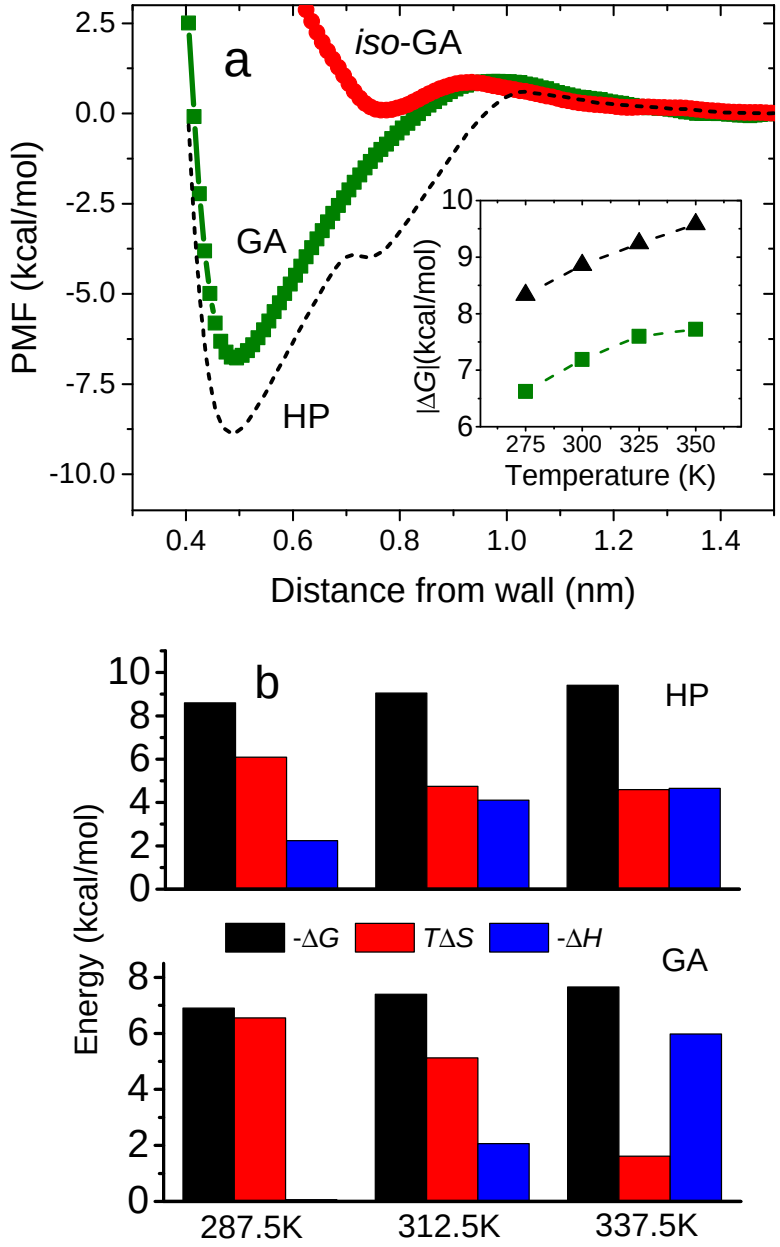

Figure 6.5: Effect of nano-pattern on hydrophobic interactions. (a) PMFs of hydrophobic interaction between a non-polar wall and different nano-rods: hydrophobic HP (dashed line), GA (green squares) and *iso*-GA (red circles). Inset: The PMF contact minimum at different temperatures: HP (black triangles) and GA (green squares). Contact minimum is defined as the lowest free energy in the PMF with the reference state where that the nano-rod and the surface are completely separated from each other. (b) The free energy decomposition at different temperatures for the interaction between the non-polar plate and the nano-rods (upper: HP, lower: GA).

To determine the thermodynamic origin of the hydrophobic interaction predicted by our MD simulations with the GA nano-pattern, we calculate the PMFs for hydrophobic interactions at a number of different temperatures as shown in the inset of Fig. 6.5a. Based on this temperature dependence, we partition the free energy into the entropy and enthalpy parts. As shown in the Fig. 6.5b, around room temperature, both the entropy and enthalpy driving forces are present in the interactions between the non-polar plate and the nano-rods (with and without immobilized ions). In other words, both the HP and GA nano-rods have a negative hydration entropy associated with their non-polar surfaces. The entropy driving force decreases with temperature as the hydrating water becomes more disordered.

Having verified that the hydrophobic interaction involving amphiphilic molecules can be turned on and off by choosing either the GA or *iso*-GA nano-pattern of the nano-rod, we now test the possibility of tuning the strength of the hydrophobic interactions by varying the size of the proximally immobilized ions of the GA nano-rod. We also investigate whether the effects of proximally immobilized ion follows the same Hofmeister order as the dissolved free ions, a question that is of practical importance for the rational design of hydrophobically driven self-assembly of materials[1–6].

To shed light on the question of the effect of the ionic size of a proximally immobilized ion on hydrophobic interaction, we calculate the PMF for the nano-rods with the proximally immobilized ions being halide anions. We choose halide anions for our test because their specific ion effects are known to be stronger than alkali cations, and their Hofmeister order in the case of free ions correlates well with the ionic sizes or, equivalently, charge densities. The PMF results are presented in Fig. 6.6a. Interestingly, we find that the strength of hydrophobic interaction between the nano-rod and the non-polar surface does not depend monotonically on the size of the proximally immobilized ion. Instead, the ranking of the interaction, from weak to strong, with different proximally immobilized ions follows $I^- < F^- < Cl^- \approx Br^-$. To ensure that the ordering of ions is not affected by the possibility of the nano-rod to reorient itself during simulations, we carried out additional simulations where the orientational freedom of the nano-rod is frozen out. In these constrained simulations, all nano-rods have their non-polar surface lying parallel to the plate during the sampling so that the reaction paths are identical for all ions. The results shown in the Appendix D show the same ordering of ions with the interaction strength, confirming that the rotational freedom of nano-rod (or its absence) does not alter the

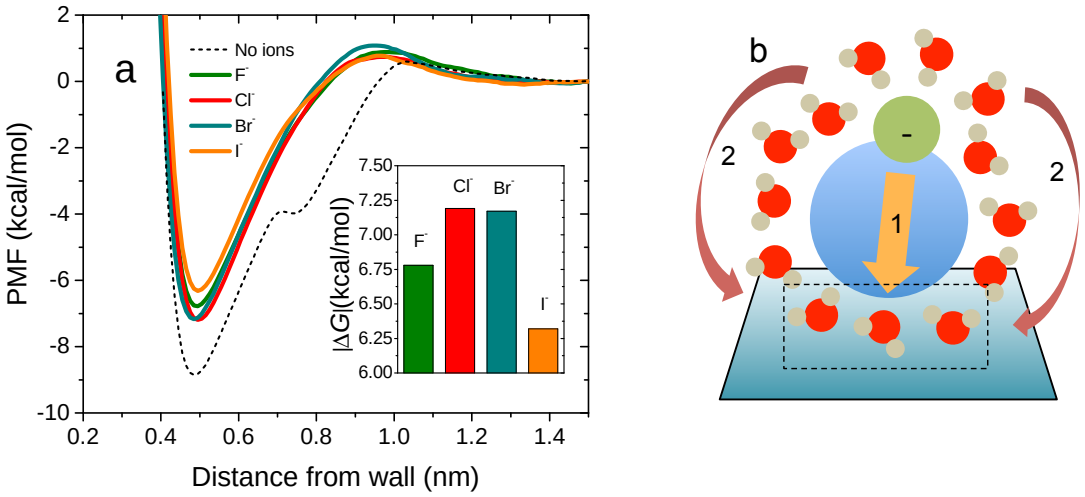

Figure 6.6: Hydrophobic interaction in the presence of proximally immobilized ions with different sizes. (a) PMF of hydrophobic interaction between a non-polar wall and the nano-rod with proximally immobilized ions with sizes that are comparable to halogen anions. The charge is constant at -1. The inset shows the depth of the contact minimum, which is defined as the absolute value of the difference in PMF between the contact minimum and the reference state where the peptide and the surface are separated from each other. (b) Schematic molecular picture of specific immobilized ion effect. Straight arrow (1) across the non-polar part of the nano-rod (blue) represents the direct electrostatic (charge-dipole) interaction between the immobilized ions (green) and the interfacial water molecules (in the dashed-line box). Curved arrows (2) represent the indirect long-range perturbation of the structuring of the water molecules by the immobilized ions.

order of the specific immobilized ion effects. In addition, we have calculated uncertainty of the PMF calculations (as explained in the Section Molecular Model and Simulation Methodology) and it was found to be smaller than 0.1 kcal/mol.

Two types of interactions can hypothetically contribute to the observed effects of immobilized ions on hydrophobic attraction and they are both illustrated by arrows in Fig. 6.6b. One contribution comes from the electrostatic interaction between the immobilized ion and water molecules residing at the nano-rod/non-polar surface interface. This interaction occurs across the diameter of the GA nano-rod. The second contribution comes from long-range perturbation of hydration shells by the immobilized ions. Both of these contributions can affect free energy of the interfacial water (between the nano-rod and the non-polar surface). The electrostatic (charge-dipole) contribution to interaction is sensitive to the charge of the ion and not to its size. On the other hand, the contribution from long-range perturbation of hydration shell can affect the entropy of interfacial water and it is sensitive to the size of the immobilized ion. The

overall specific proximal ion effect is expected to be a balance of these two mechanisms and further studies are needed to better understand the underlying molecular details.

Although many differences exist between the recent experiment studies using β-peptides and the models used in our simulations, our simulations do support the experimental finding that the immobilized ions can have a long-range effect on hydrophobic interactions.

6.3.4 Comparison between the effects of proximally immobilized ion and soluble salts

It is instructive to compare the effects from the same ion in different states, soluble and immobilized. In Fig. 6.7 we summarize the effects of immobilized ions and free ions. We choose the reference (a dashed line in Fig. 6.7) for both cases to be the hydrophobic interaction strength between the HP nano-rod and the extended non-polar surface without any ions. Inspection of Fig. 6.7 reveals that the immobilized ions tend to weaken the hydrophobic interaction while the free ones tend to strengthen it. This difference is related to the distinct spatial distributions of immobilized and free ions. One can think of the hydrophobic interaction as a dehydrating reaction accompanied by the release of water molecules from the surface of the solute to the bulk region, which can be symbolically written as

$$\text{Nano-rod} \cdot \text{H}_2\text{O} + \text{Surface} \cdot \text{H}_2\text{O} \xrightarrow{\text{dehydrate}} \text{Nano-rod}|\text{surface} + \text{H}_2\text{O(bulk)}, \tag{6.1}$$

where symbol $\cdot$ means hydrating and symbol | means in contact. The strength of hydrophobic interaction is determined by

$$\begin{aligned} \Delta G_{\text{dehydrate}} &= G_{\text{H}_2\text{O(bulk)}} - [G_{\text{Nano-rod} \cdot \text{H}_2\text{O}} + G_{\text{Surface} \cdot \text{H}_2\text{O}} - G_{\text{Nano-rod|surface}}] \\ &= G_{\text{H}_2\text{O(bulk)}} - G_{\text{H}_2\text{O(surface)}}. \end{aligned} \tag{6.2}$$

Here, we defined $G_{\text{H2O(surface)}}$, which qualitatively can be understood as the free energy of water near the non-polar surfaces (the non-polar domain of GA nano-rod and the flat non-polar surface) when they are far from each other. The specific ion effect on hydrophobic interaction can therefore be generally understood as the difference in the manners the ion modifies the free

energy of hydrating water and of bulk water

$$\Delta(\Delta G_{\text{dehydrate}}) = \Delta G_{\text{H}_2\text{O(bulk)}} - \Delta G_{\text{H}_2\text{O(surface)}}. \tag{6.3}$$

The sign of $\Delta(\Delta G_{\text{dehydrate}})$ determines whether the ion increases or decreases the strength of hydrophobic interaction. As we are interested in the immobilized ion effect, we here focus on the free energy of water hydrating the nano-rod. The free energy of water hydrating the non-polar plate is not sensitive to the proximally immobilized ions and can be treated as a constant reference because the plate is well isolated from the nano-rod in the non-interacting reference state. The distinct effects from an immobilized ion and a free ion result from their different spatial distributions with respect to the nano-rod, i.e., immobilized ions are immobilized near the nano-rod and absent in the bulk water whereas free ions are excluded from the nano-rod and remain in the bulk. Therefore in Eq 6.3, the $\Delta G_{\text{H}_2\text{O(bulk)}}$ term is important for free ions but it is negligible for immobilized ions. This means that an immobilized ion weakens the hydrophobic interaction solely by lowering the free energy of water hydrating the nano-rod. In contrast, the free ion effect is a result of the changes in both the hydrating free energy and bulk free energy. In our case, as the nano-rod is small in size and highly convex in curvature, free ions are generally excluded from it and mainly lower the free energy of bulk water. The exclusion of ions, including I^-, from small hydrophobes have been recently reported in experiments[40;41]. It is interesting to note that regardless of whether ions are immobilized or dissolved, the same ions have different rankings with respect to their modulations of strength of hydrophobic interactions.

6.4 Concluding remarks

We have used MD simulations to study the effects of proximally immobilized ions on hydrophobic interactions between a β-peptide inspired nano-rod and an extended non-polar surface. By comparing the effect of immobilized ions with different nano-patterns and ionic radii, we demonstrated that hydrophobic interaction can be largely eliminated by *iso*-GA patterning and can be modulated by proximally immobilized ions in the globally amphiphilic (GA) nano-rod. Several trends observed in our simulations agree with recent single-molecule AFM measurements[8;9] and we provide a molecular mechanistic understanding of these trends in the context of the

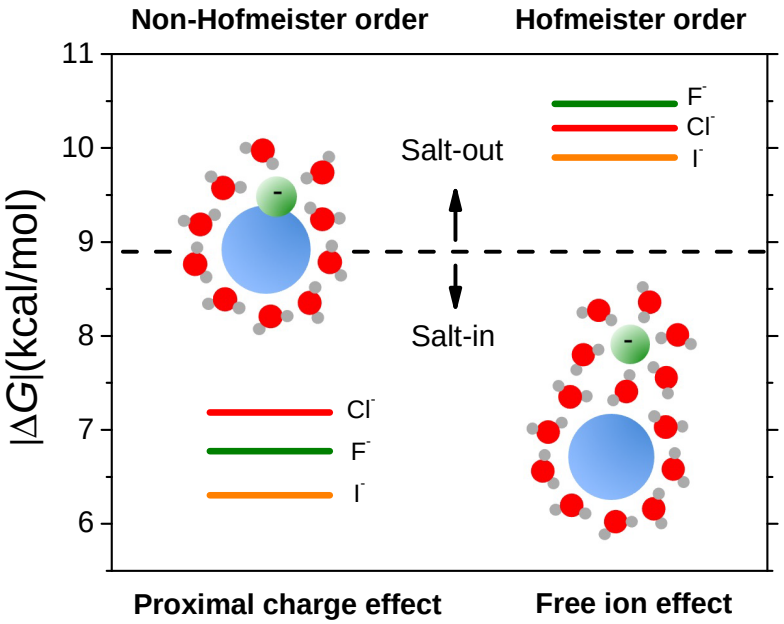

Figure 6.7: Comparison between immobilized and free ion effect.

models used in the MD simulation. In the broader context of specific-ion effects, we have shown that the immobilized ions do not necessarily follow the same ordering as the free ions. Our analysis of the structure and dynamics of water near the hydrophobic nano-rod shows that dynamics is a better indicator of the specific ion effect than the static water structure. This result extends prior results of Garde and coworkers[29]. Our results provide new insights into specific ion effects that may, in the long term, guide the rational design of hydrophobic interactions and self-assembly process driven by these interactions.

Bibliography

[1] G. Whitesides, J. Mathias, and C. Seto, "Molecular self-assembly and nanochemistry - a chemical strategy for the synthesis of nanostructures," *SCIENCE*, vol. 254, pp. 1312–1319, NOV 29 1991.

[2] R. Cheng, S. Gellman, and W. DeGrado, "beta-peptides: From structure to function," *CHEMICAL REVIEWS*, vol. 101, pp. 3219–3232, OCT 2001.

[3] S. Vauthey, S. Santoso, H. Gong, N. Watson, and S. Zhang, "Molecular self-assembly of surfactant-like peptides to form nanotubes and nanovesicles," *PROCEEDINGS OF THE NATIONAL ACADEMY OF SCIENCES OF THE UNITED STATES OF AMERICA*, vol. 99, pp. 5355–5360, APR 16 2002.

[4] N. Seeman, "DNA in a material world," *NATURE*, vol. 421, pp. 427–431, JAN 23 2003.

[5] Q. Chen, S. C. Bae, and S. Granick, "Directed self-assembly of a colloidal kagome lattice," *NATURE*, vol. 469, pp. 381–384, JAN 20 2011.

[6] J. Hartgerink, E. Beniash, and S. Stupp, "Self-assembly and mineralization of peptide-amphiphile nanofibers," *SCIENCE*, vol. 294, pp. 1684–1688, NOV 23 2001.

[7] P. Jungwirth and P. S. Cremer, "Beyond Hofmeister," *NATURE CHEMISTRY*, vol. 6, pp. 261–263, APR 2014.

[8] C. Acevedo-Velez, G. Andre, Y. F. Dufrene, S. H. Gellman, and N. L. Abbott, "Single-Molecule Force Spectroscopy of beta-Peptides That Display Well-Defined Three-Dimensional Chemical Patterns," *JOURNAL OF THE AMERICAN CHEMICAL SOCIETY*, vol. 133, pp. 3981–3988, MAR 23 2011.

[9] C. Ma, C. Wang, C. Acevedo-Velez, S. H. Gellman, and N. L. Abbott, "Modulation of the Strength of Hydrophobic Interactions by Proximally Immobilized Ions," *NATURE*, vol. 517, pp. 347–350, JAN 2015 2015.

[10] W. C. Pomerantz, V. M. Yuwono, R. Drake, J. D. Hartgerink, N. L. Abbott, and S. H. Gellman, "Lyotropic Liquid Crystals Formed from ACHC-Rich beta-Peptides," *JOURNAL OF THE AMERICAN CHEMICAL SOCIETY*, vol. 133, pp. 13604–13613, AUG 31 2011.

[11] S. Funkner, G. Niehues, D. A. Schmidt, M. Heyden, G. Schwaab, K. M. Callahan, D. J. Tobias, and M. Havenith, "Watching the Low-Frequency Motions in Aqueous Salt Solutions: The Terahertz Vibrational Signatures of Hydrated Ions," *JOURNAL OF THE AMERICAN CHEMICAL SOCIETY*, vol. 134, pp. 1030–1035, JAN 18 2012.

[12] G. Stirnemann, E. Wernersson, P. Jungwirth, and D. Laage, "Mechanisms of Acceleration and Retardation of Water Dynamics by Ions," *JOURNAL OF THE AMERICAN CHEMICAL SOCIETY*, vol. 135, pp. 11824–11831, AUG 14 2013.

[13] F. Hofmeister, "Concerning regularities in the protein-precipitating effects of salts and the relationship of these effects to the physiological behaviour of salts," *Arch. Exp. Pathol. Pharmakol.*, vol. 24, pp. 247–260, APR 1888.

[14] R. Cheng, S. Gellman, and W. DeGrado, "beta-peptides: From structure to function," *CHEMICAL REVIEWS*, vol. 101, pp. 3219–3232, OCT 2001.

[15] D. Appella, L. Christianson, I. Karle, D. Powell, and S. Gellman, "beta-peptide foldamers: Robust Helix formation in a new family of beta-amino acid oligomers," *JOURNAL OF THE AMERICAN CHEMICAL SOCIETY*, vol. 118, pp. 13071–13072, DEC 25 1996.

[16] T. Raguse, J. Lai, and S. Gellman, "Environment-independent 14-helix formation in short beta-peptides: Striking a balance between shape control and functional diversity," *JOURNAL OF THE AMERICAN CHEMICAL SOCIETY*, vol. 125, pp. 5592–5593, MAY 14 2003.

[17] B. Hess, C. Kutzner, D. van der Spoel, and E. Lindahl, "GROMACS 4: Algorithms for highly efficient, load-balanced, and scalable molecular simulation," *JOURNAL OF CHEMICAL THEORY AND COMPUTATION*, vol. 4, pp. 435–447, MAR 2008.

[18] H. BERENDSEN, J. GRIGERA, and T. STRAATSMA, "THE MISSING TERM IN EFFECTIVE PAIR POTENTIALS," *JOURNAL OF PHYSICAL CHEMISTRY*, vol. 91, pp. 6269–6271, NOV 19 1987.

[19] B. Hess, "P-LINCS: A parallel linear constraint solver for molecular simulation," *JOURNAL OF CHEMICAL THEORY AND COMPUTATION*, vol. 4, pp. 116–122, JAN 2008.

[20] J. Mondal, B. J. Sung, and A. Yethiraj, "Sequence dependent self-assembly of beta-peptides: Insights from a coarse-grained model," *JOURNAL OF CHEMICAL PHYSICS*, vol. 132, FEB 14 2010.

[21] W. Jorgensen, D. Maxwell, and J. TiradoRives, "Development and testing of the OPLS all-atom force field on conformational energetics and properties of organic liquids," *JOURNAL OF THE AMERICAN CHEMICAL SOCIETY*, vol. 118, pp. 11225–11236, NOV 13 1996.

[22] R. Zangi, M. Hagen, and B. J. Berne, "Effect of ions on the hydrophobic interaction between two plates," *JOURNAL OF THE AMERICAN CHEMICAL SOCIETY*, vol. 129, pp. 4678–4686, APR 18 2007.

[23] A. S. Thomas and A. H. Elcock, "Molecular dynamics simulations of hydrophobic associations in aqueous salt solutions indicate a connection between water hydrogen bonding and the Hofmeister effect," *JOURNAL OF THE AMERICAN CHEMICAL SOCIETY*, vol. 129, pp. 14887–14898, DEC 5 2007.

[24] N. Schwierz, D. Horinek, and R. R. Netz, "Anionic and Cationic Hofmeister Effects on Hydrophobic and Hydrophilic Surfaces," *LANGMUIR*, vol. 29, pp. 2602–2614, FEB 26 2013.

[25] B. Efron and R. Tibshirani, *An introduction to the bootstrap*. CRC Press, 1994.

[26] F. Zhu and G. Hummer, "Convergence and error estimation in free energy calculations using the weighted histogram analysis method," *JOURNAL OF COMPUTATIONAL CHEMISTRY*, vol. 33, pp. 453–465, FEB 5 2012.

[27] D. Chandler, "Interfaces and the driving force of hydrophobic assembly," *NATURE*, vol. 437, pp. 640–647, SEP 29 2005.

[28] W. Blokzijl and J. Engberts, "Hydrophobic effects - opinions and facts," *ANGEWANDTE CHEMIE-INTERNATIONAL EDITION*, vol. 32, pp. 1545–1579, NOV 1993.

[29] S. N. Jamadagni, R. Godawat, and S. Garde, "Hydrophobicity of Proteins and Interfaces: Insights from Density Fluctuations," in *ANNUAL REVIEW OF CHEMICAL AND BIOMOLECULAR ENGINEERING, VOL 2* (Prausnitz, JM, ed.), vol. 2 of *Annual Review of Chemical and Biomolecular Engineering*, pp. 147–171, 2011.

[30] D. Laage, G. Stirnemann, F. Sterpone, R. Rey, and J. T. Hynes, "Reorientation and Allied Dynamics in Water and Aqueous Solutions," in *ANNUAL REVIEW OF PHYSICAL CHEMISTRY, VOL 62* (Leone, SR and Cremer, PS and Groves, JT and Johnson, MA, ed.), vol. 62 of *Annual Review of Physical Chemistry*, pp. 395–416, 4139 EL CAMINO WAY, PO BOX 10139, PALO ALTO, CA 94303-0897 USA: ANNUAL REVIEWS, 2011.

[31] Y. L. A. Rezus and H. J. Bakker, "Observation of immobilized water molecules around hydrophobic groups," *PHYSICAL REVIEW LETTERS*, vol. 99, OCT 5 2007.

[32] K. J. Tielrooij, N. Garcia-Araez, M. Bonn, and H. J. Bakker, "Cooperativity in Ion Hydration," *SCIENCE*, vol. 328, pp. 1006–1009, MAY 21 2010.

[33] K.-J. Tielrooij, J. Hunger, R. Buchner, M. Bonn, and H. J. Bakker, "Influence of Concentration and Temperature on the Dynamics of Water in the Hydrophobic Hydration Shell of Tetramethylurea," *JOURNAL OF THE AMERICAN CHEMICAL SOCIETY*, vol. 132, pp. 15671–15678, NOV 10 2010.

[34] W. C. Pomerantz, N. L. Abbott, and S. H. Gellman, "Lyotropic liquid crystals from designed helical beta-peptides," *JOURNAL OF THE AMERICAN CHEMICAL SOCIETY*, vol. 128, pp. 8730–8731, JUL 12 2006.

[35] W. C. Pomerantz, K. D. Cadwell, Y.-J. Hsu, S. H. Gellman, and N. L. Abbott, "Sequence dependent behavior of amphiphilic beta-peptides on gold surfaces," *CHEMISTRY OF MATERIALS*, vol. 19, pp. 4436–4441, SEP 4 2007.

[36] W. C. Pomerantz, V. M. Yuwono, C. L. Pizzey, J. D. Hartgerink, N. L. Abbott, and S. H. Gellman, "Nanofibers and lyotropic liquid crystals from a class of self-assembling beta-peptides," *ANGEWANDTE CHEMIE-INTERNATIONAL EDITION*, vol. 47, no. 7, pp. 1241–1244, 2008.

[37] J. Mondal, B. J. Sung, and A. Yethiraj, "Sequence-Directed Organization of beta-Peptides in Self-Assembled Monolayers," *JOURNAL OF PHYSICAL CHEMISTRY B*, vol. 113, pp. 9379–9385, JUL 16 2009.

[38] J. Mondal, X. Zhu, Q. Cui, and A. Yethiraj, "Self-Assembly of beta-Peptides: Insight from the Pair and Many-Body Free Energy of Association," *JOURNAL OF PHYSICAL CHEMISTRY C*, vol. 114, pp. 13551–13556, AUG 19 2010.

[39] H. Acharya, S. Vembanur, S. N. Jamadagni, and S. Garde, "Mapping hydrophobicity at the nanoscale: Applications to heterogeneous surfaces and proteins," *FARADAY DISCUSSIONS*, vol. 146, pp. 353–365, 2010.

[40] B. M. Rankin, M. D. Hands, D. S. Wilcox, K. R. Fega, L. V. Slipchenko, and D. Ben-Amotz, "Interactions between halide anions and a molecular hydrophobic interface," *FARADAY DISCUSSIONS*, vol. 160, pp. 255–270, 2013.

[41] B. M. Rankin and D. Ben-Amotz, "Expulsion of Ions from Hydrophobic Hydration Shells," *JOURNAL OF THE AMERICAN CHEMICAL SOCIETY*, vol. 135, pp. 8818–8821, JUN 19 2013.

7 Summary and future directions

In this thesis, we have combined theory and computer simulations to explore the frictional and solvation forces at aqueous interfaces, which forces play an important fundamental role in small length scale hydrodynamics and solvent-mediated interactions, respectively.

On the hydrodynamic side, we have demonstrated that liquid boundary condition is an interfacial transport phenomenon and depends on the intrinsic nature of the liquid-solid (L-S) interface. By simulating vibrating L-S interfaces in non-equilibrium molecular dynamics (NEMD) simulations, we demonstrated and modeled the effects of slip boundary condition on the energy dissipation of the interfaces. The simulation uncovered a dynamic L-S slip (or alternatively friction), which is not a constant but depends on frequency. To enable equilibrium molecular dynamics (EMD) simulations of the L-S boundary conditions at experimentally relevant scales, we have developed a Green Kubo (GK) relation that relates the microscopic interfacial correlation functions to the macroscopic friction coefficient. This relation also allows one to effectively calculate mobility (or diffusion) of interfacial liquids. Using our GK relation, we have shown that boundary condition has a memory, which means that this boundary relaxes with time. Such boundary relaxation can strongly affect the near-boundary Brownian motion as we demonstrated from large-scale long-time molecular dynamics (MD) simulations. Near a boundary, the VAF of Brownian particle decays as a function of $t^{-5/2}$ with time t. While the general shape of such long-time tail is due to a universal geometry effect, the amplitude of the tail is sensitive to the properties of the L-S interface. Therefore the monitoring of near-boundary Brownian motion provides a method to probe the interfacial properties. Our current study is limited to simple (Newtonian) liquids and simple structured surfaces. One natural step further can be the study of near-boundary Brownian motion in viscoelastic fluids and the investigation of boundary relaxation on patterned and chemically functionalized surfaces.

On the solvation side, we have studied the effect of immobilized ions on hydrophobic interactions

in water. This effect is found to be distinct from a similar effect previously reported for free ions. Not only the surface arrangement but also the species of immobilized ions can play a role in modulating the hydrophobic interaction of amphiphic molecules on which the ions reside. In the case of free ions, such modulation of solute interaction is correlated with the hydration fluctuation near the solute. The knowledge of the effects of free and immobilized ions provides a foundation towards understanding of more complicated specific ion effects in biological systems, where immobilized and free ion effects could be strongly coupled.

Another future direction is the curvature effect on the hydration in alcohol. Compared to water, the solvation in the aqueous solution of alcohol has been much less studied. However, there is a merit to extend the investigations of solvation from water to alcohol for the following reasons. First of all, alcohol is an amphiphilic solvent in which both polar and non-polar solutes could be dissolved. The amphiphilic solvation effect is an interesting problem in itself with widespread industrial applications[1;2]. Secondly, alcohol mixes with water and can be used to suppress hydrophobic interactions[3;4]. While it is reasoned that alcohol can disrupt the hydrogen bond network in water, the underlying molecular mechanism is yet to be fully explored. Lastly, alcohol such as methanol is similar to water in structure with a substitution of H atom to a methyl group. A comparison between the solvation thermodynamics in water and alcohol can offer a more general understanding to the hydrophobic hydration.

Bibliography

[1] H. Gasteiger, N. Markovic, P. Ross, and E. Cairns, "Methanol electrooxidation on well-characterized Pt-Rn alloys," *JOURNAL OF PHYSICAL CHEMISTRY*, vol. 97, pp. 12020–12029, NOV 18 1993.

[2] K. Kreuer, "On the development of proton conducting polymer membranes for hydrogen and methanol fuel cells," *JOURNAL OF MEMBRANE SCIENCE*, vol. 185, pp. 29–39, APR 15 2001.

[3] C. Acevedo-Velez, G. Andre, Y. F. Dufrene, S. H. Gellman, and N. L. Abbott, "Single-Molecule Force Spectroscopy of beta-Peptides That Display Well-Defined Three-Dimensional Chemical Patterns," *JOURNAL OF THE AMERICAN CHEMICAL SOCIETY*, vol. 133, pp. 3981–3988, MAR 23 2011.

[4] C. Ma, C. Wang, C. Acevedo-Velez, S. H. Gellman, and N. L. Abbott, "Modulation of the Strength of Hydrophobic Interactions by Proximally Immobilized Ions," *NATURE*, vol. 517, pp. 347–350, JAN 2015 2015.

Appendices

Appendix A: Derivation of the mechanical model of vibrational liquid-solid interface at high frequencies

Here we provide details of derivation of our slip-boundary model that includes high-frequency effects. First of all, the equation of motion of a solid slab connected to elastic springs can be written as:

$$M\ddot{x} = -kx, \tag{A1}$$

where M is the mass of the solid slab per unit area and k is spring constant per unit area. The displacement x and velocity u_0 along the direction of vibration can be written, respectively , as:

$$x = Ae^{i\omega_0 t}, \tag{A2}$$

$$u_0 = \dot{x} = i\omega_0 x. \tag{A3}$$

ω_0 is the resonance frequency and it is equal to

$$\omega_0 = \sqrt{\frac{k}{M}}. \tag{A4}$$

When the solid slab is loaded with liquid as shown schematically in Fig. A1, there will be a friction force F_f exerted by the liquid on the solid surface, and the equation of motion will be correspondingly modified to:

$$M\ddot{x} = -kx - F_f. \tag{A5}$$

Assuming a new time dependence of the vibrational displacement, $x = Ae^{i\omega t}$, and including

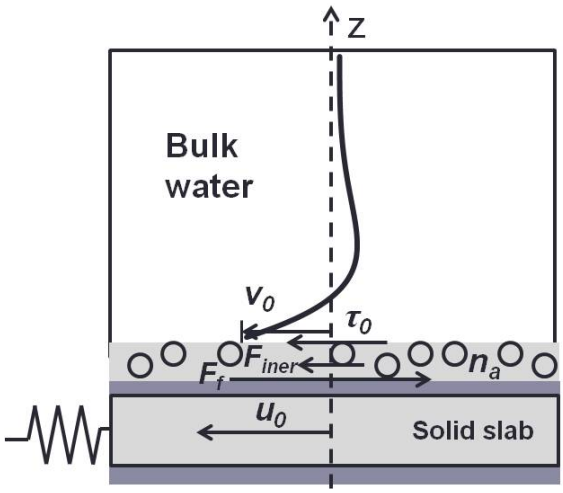

Figure A1: Schematic representation of the force balance on the interfacial liquid.

Eq. A4, we can rewrite A5 as:

$$M\omega^2 x = M\omega_0^2 x + F_f. \tag{A6}$$

The shift in the frequency $\Delta\omega = \omega - \omega_0$ is equal to:

$$\Delta\omega = \frac{F_f}{2M\omega_0 x}. \tag{A7}$$

$\Delta\omega$ is a complex number, which means that the shift in resonance frequency is accompanied by a dissipation of the mechanical energy of vibration. The displacement x can be therefore written explicitly:

$$x = Ae^{i(\omega_0+\Delta\omega)t} = Ae^{i[\omega_0+\mathrm{Re}(\Delta\omega)]t}e^{-\mathrm{Im}(\Delta\omega)t}. \tag{A8}$$

The friction force (per unit area) on the solid slab is the sum of shear stress of the liquid at the interface τ_0 and the inertia of the interfacial liquid F_{iner} (see Fig. A1):

$$F_f = \tau_0 + F_{iner}. \tag{A9}$$

Since friction in this case is viscous, it can be written as:

$$F_f = \overline{\eta}_d(u_0 - v_0), \tag{A10}$$

where $\overline{\eta}_d$ is dynamic friction coefficient and $u_0 - v_0$ is the slip velocity. Using the velocity profile of liquid along the z direction (perpendicular to the surface)

$$v(z) = v_0 e^{\frac{-1-i}{\delta}z}, \tag{A11}$$

we can write the shear stress term in Eq. A9 as

$$\tau_0 = -\eta \frac{\partial v}{\partial z}\Big|_{z=0} = (1+i)\frac{\eta v_0}{\delta}, \tag{A12}$$

where $\delta = (2\eta/\omega\rho_l)^{1/2}$ is the penetration length of the liquid. Finally, the inertia term in A9 is equal to

$$F_{iner} = n_a m \frac{\partial v_0}{\partial t} = i\omega n_a m v_0, \tag{A13}$$

where n_a is the surface number density of the interfacial liquid. By including Eq. A10, Eq. A12 and Eq. A13, Eq. A9 becomes

$$\overline{\eta}_d(u_0 - v_0) = (1+i)\frac{\eta v_0}{\delta} + i\omega n_a m v_0. \tag{A14}$$

Let us recall the definitions of the dynamic slip length and the adsorption length, respectively,

$$l_d(\omega) = \frac{\eta(\omega)}{\overline{\eta}_d(\omega)}, \tag{A15}$$

$$l_a = \frac{n_a}{n}. \tag{A16}$$

When normalized by the penetration length δ these properties become

$$b_d = \frac{l_d}{\delta}, \tag{A17}$$

$$a = \frac{l_a}{\delta}. \tag{A18}$$

Substituting A17 and A18 into A14 simplifies A14 to the following form:

$$\begin{aligned} u_0 - v_0 &= (1+i)\frac{l_d}{\delta}v_0 + i\frac{\omega\rho_l l_a}{\overline{\eta}_d}v_0 \\ &= (1+i)b_d v_0 + 2iab_d v_0 \\ &= [1+i(1+2a)]b_d v_0. \end{aligned} \tag{A19}$$

By rearranging terms, we arrive at a relation between the dynamic slip length and the slip velocity:

$$b_d = \frac{1}{\sqrt{2+4a+4a^2}}\left|\frac{u_0 - v_0}{v_0}\right|. \tag{A20}$$

In addition, v_0 can be determined based on u_0, b_d and a in the following way

$$v_0 = \frac{u_0}{(1+b_d)+i(1+2a)b_d}. \tag{A21}$$

The above expressions allow us to express the friction force F_f in terms of u_0, b_d and a, that is

$$F_f = \overline{\eta}_d(u_0 - v_0) = \frac{[1+i(1+2a)]b_d}{(1+b_d)+i(1+2a)b_d}\overline{\eta}_d u_0. \tag{A22}$$

Substituting F_f into Eq. A7 produces the expression for $\Delta\omega$ in terms of the normalized slip length b_d and the adsorption length a

$$\begin{aligned} \Delta\omega &= \frac{\overline{\eta}_d u_0 b_d}{2M\omega_0 x}\frac{1+i(1+2a)}{(1+b_d)+i(1+2a)b_d} \\ &= \frac{i\overline{\eta}_d b_d}{2M}\frac{1+i(1+2a)}{(1+b_d)+i(1+2a)b_d} \\ &= \frac{1}{2M}\sqrt{\frac{\rho_l\eta_d\omega}{2}}\frac{-(1+2a)+i}{(1+b_d)+i(1+2a)b_d} \\ &= \frac{1}{2M}\sqrt{\frac{\rho_l\eta_d\omega}{2}}\frac{-(1+2a)+i\{1+[1+(1+2a)^2]b_d\}}{1+2b_d+[1+(1+2a)^2]b_d^2}. \end{aligned} \tag{A23}$$

Recalling that $Z = \sqrt{kM}$ is the mechanical impedance in the spring model, we can obtain the frequency shift Δf and the damping rate shift ΔD ($D_0 = 0$ in this case):

$$\frac{\Delta f}{f_0} = \frac{\mathrm{Re}(\Delta\omega)}{\omega_0} = -\frac{1}{2Z}\sqrt{\frac{\rho_l\eta_d\omega}{2}}\frac{1+2a}{1+2b_d+[(1+2a)^2+1]b_d^2}, \tag{A24}$$

$$\frac{\Delta D}{2\pi} = \frac{\mathrm{Im}(\Delta\omega)}{\omega_0} = \frac{1}{2Z}\sqrt{\frac{\rho_l\eta_d\omega}{2}}\frac{1+[(1+2a)^2+1]b_d}{1+2b_d+[(1+2a)^2+1]b_d^2}. \tag{A25}$$

These equations can be written in terms of frequency shift ($\frac{\Delta f}{f_0}\Big|_{no-slip}$) and damping shift ($\frac{\Delta D}{2\pi}\Big|_{no-slip}$) in the absence of slip:

$$\frac{\Delta f}{f_0} = \frac{1+2a}{1+2b_d+[(1+2a)^2+1]b_d^2}\frac{\Delta f}{f_0}\Big|_{no-slip}, \tag{A26}$$

$$\frac{\Delta D}{2\pi} = \frac{1+[(1+2a)^2+1]b_d}{1+2b_d+[(1+2a)^2+1]b_d^2}\frac{\Delta D}{2\pi}\Big|_{no-slip}. \tag{A27}$$

In the case of shear-wave QCM model, Eq. A26 and Eq. A27 become

$$\frac{\Delta f}{f_0} = -\frac{1}{\pi Z}\sqrt{\frac{\rho_l\eta_d\omega}{2}}\frac{1+2a}{1+2b_d+[(1+2a)^2+1]b_d^2}, \tag{A28}$$

$$\frac{\Delta D}{2\pi} = \frac{1}{\pi Z}\sqrt{\frac{\rho_l\eta_d\omega}{2}}\frac{1+[(1+2a)^2+1]b_d}{1+2b_d+[(1+2a)^2+1]b_d^2}. \tag{A29}$$

It is straightforward to show that at low frequency when $a \approx 0$ and $b_d \approx b_0$, A28 and A29 can be simplified to the following:

$$\frac{\Delta f}{f_0} = -\frac{1}{\pi Z}\sqrt{\frac{\rho_l\eta\omega}{2}}\frac{1}{1+2b_0+2b_0^2}, \tag{A30}$$

$$\frac{\Delta D}{2\pi} = \frac{1}{\pi Z}\sqrt{\frac{\rho_l\eta\omega}{2}}\frac{1+2b_0}{1+2b_0+2b_0^2}. \tag{A31}$$

Appendix B: Derivation of the extended GLE based on the projection operator approach

In Chapter 4 we showed that Eq. 4.11 can be reformulated into Eq. 4.26 if the motion of interfacial liquid particle can be described by an extended GLE (Eq. 4.13). Here we construct an extended GLE using the projection operator technique for a diffusive particle moving in an external potential $U(\vec{r})$ with the resulted external force being $\vec{F} = -\nabla U(\vec{r})$. We show that under the condition $\langle \vec{F} \rangle = 0$, one can retrieve the properties in Eqs. 4.14-4.16.

Motivated by connecting different correlation functions, we extended the original GLE by keeping the F_i term out of the memory kernel and the random force. Therefore we first decompose the acceleration $\dot{\vec{u}}_i$ of an interfacial particle into to two parts: due to the external potential (the solid wall) and due to the surrounding liquid, that is

$$\dot{\vec{u}}_i = \mathrm{i}\mathbf{L}\vec{u}_i = \mathrm{i}\mathbf{A}\vec{u}_i + \mathrm{i}\mathbf{B}\vec{u}_i = \vec{F}_\mathrm{A} + \vec{F}_\mathrm{B}, \tag{B1}$$

where $\mathbf{L}$ is the Liouville differential operator, and $\vec{F}_\mathrm{A}$, $\vec{F}_\mathrm{B}$ are forces exerted on the particle by the surrounding liquid and the solid wall, respectively. Here we have normalized the mass to be 1. In this formulation, we use the symbol $\vec{F}_\mathrm{B}$, but the reader should be aware that its physical meaning is the same as of the symbol F used in the main text (here we are dealing with the generalized 3 dimensional case while the equations in the main text is one dimensional). At $t = 0$, the interfacial particle of interest i is at position $\vec{r}_i$ and has velocity $\vec{u}_i$. We now introduce projection operators $\mathbf{P} = |\vec{u}_i\rangle\langle\vec{u}_i|\langle\vec{u}_i\vec{u}_i\rangle^{-1}$ and $\mathbf{Q} = 1 - \mathbf{P}$, so that

$$\mathrm{e}^{\mathrm{i}\mathbf{L}t} = \mathrm{e}^{\mathrm{i}\mathbf{Q}\mathbf{L}t} + \int_0^t \mathrm{e}^{\mathrm{i}\mathbf{L}(t-t')}\mathrm{i}\mathbf{P}\mathbf{L}\mathrm{e}^{\mathrm{i}\mathbf{Q}\mathbf{L}t'}\,\mathrm{d}t', \tag{B2}$$

where the inner product between two vectors a, b in the Hilbert space $\langle ab \rangle$ is defined as the ensemble average at equilibrium. Since we are interested in the interfacial particle i, we only average the position $\vec{r}_i$ over the interfacial region we defined. In a three dimensional system in space, infinite dimensional vectore a and b in the Hilbert space are also three dimensional vectors in space, and $\langle ab \rangle$ is therefore a tensor in space.

Using the operator identity (Eq. B2), we can rewrite Eq. B1 as

$$\begin{aligned}\dot{\vec{u}}_i(t) = -\frac{1}{kT}\int_0^t \vec{u}_i(t-t')\langle \mathrm{i}\mathbf{L}\vec{u}_i \mathrm{e}^{\mathrm{i}\mathbf{Q}\mathrm{L}t'}\mathrm{i}\mathbf{A}\vec{u}_i\rangle \,\mathrm{d}t' \\ +\mathrm{e}^{\mathrm{i}\mathbf{Q}\mathbf{L}t}\mathrm{i}\mathbf{A}\vec{u}_i + \mathrm{e}^{\mathrm{i}\mathbf{L}t}\mathrm{i}\mathbf{B}\vec{u}_i.\end{aligned} \tag{B3}$$

We define $\vec{R}(t) = \mathrm{e}^{\mathrm{i}\mathbf{Q}\mathbf{L}t}\mathrm{i}\mathbf{A}\vec{u}_i$ to be the random force. Then $kT\boldsymbol{\gamma}(t) = \langle \mathrm{i}\mathbf{L}\vec{u}_i \mathrm{e}^{\mathrm{i}\mathbf{Q}\mathbf{L}t}\mathrm{i}\mathbf{A}\vec{u}_i\rangle = \langle \vec{R}(0)\vec{R}(t)\rangle + \langle \vec{F}(0)\vec{R}(t)\rangle$ defines the memory kernel tensor. More explicitly,

$$\langle \vec{R}(0)\vec{R}(t)\rangle = \langle \mathrm{i}\mathbf{A}\vec{u}_i \mathrm{e}^{\mathrm{i}\mathbf{Q}\mathbf{L}t}\mathrm{i}\mathbf{A}\vec{u}_i\rangle, \tag{B4}$$

$$\langle \vec{F}(0)\vec{R}(t)\rangle = \langle \mathrm{i}\mathbf{B}\vec{u}_i \mathrm{e}^{\mathrm{i}\mathbf{Q}\mathbf{L}t}\mathrm{i}\mathbf{A}\vec{u}_i\rangle. \tag{B5}$$

At equilibrium, we have $\langle \vec{u}_i\vec{F}_\mathrm{A}\rangle = \langle \vec{u}_i\vec{F}_\mathrm{B}\rangle = 0$ as the result of antisymmetries under time reversal. This means that $|\mathrm{i}\mathbf{A}\vec{u}_i\rangle$ and $|\mathrm{i}\mathbf{B}\vec{u}_i\rangle$ are both orthogonal to $|\vec{u}_i\rangle$. Applying the projection, we have $\mathbf{P}|\mathrm{i}\mathbf{A}\vec{u}_i\rangle = \mathbf{P}|\mathrm{i}\mathbf{B}\vec{u}_i\rangle = 0$ and $\mathbf{Q}|\mathrm{i}\mathbf{A}\vec{u}_i\rangle = |\mathrm{i}\mathbf{A}\vec{u}_i\rangle, \mathbf{Q}|\mathrm{i}\mathbf{B}\vec{u}_i\rangle = |\mathrm{i}\mathbf{B}\vec{u}_i\rangle$. Therefore the operator $\mathbf{QL}$ is Hermitian in the subspace of $|\mathrm{i}\mathbf{A}\vec{u}_i\rangle$ and $|\mathrm{i}\mathbf{B}\vec{u}_i\rangle$.

If $\langle \vec{F}(0)\vec{R}(t)\rangle = 0$, then $kT\boldsymbol{\gamma}(t) = \langle \vec{R}(0)\vec{R}(t)\rangle$ recovers the fluctuation-dissipation theorem. This assumption is not formal under all conditions. In fact, whether $\langle \vec{F}(0)\vec{R}(t)\rangle$ equals to zero or not depends on the properties of $\vec{F}_\mathrm{A}$ and $\vec{F}_\mathrm{B}$ or, equivalently, on the properties of the operators $\mathbf{A}$ and $\mathbf{B}$. In our case, we show that every element of $\langle \vec{F}(0)\vec{R}(t)\rangle$ is zero except $\langle F_z(0)R_z(t)\rangle$ (z is the norm direction of the wall) in the following way. Let us take the time derivative

$$\begin{aligned}\frac{\mathrm{d}}{\mathrm{d}t}\langle \vec{F}(0)\vec{R}(t)\rangle &= \frac{\mathrm{d}}{\mathrm{d}t}\langle \mathrm{i}\mathbf{B}\vec{u}_i \mathrm{e}^{\mathrm{i}\mathbf{Q}\mathbf{L}t}\mathrm{i}\mathbf{A}\vec{u}_i\rangle \\ &= \langle \mathrm{i}\mathbf{B}\vec{u}_i \mathrm{i}\mathbf{Q}\mathbf{L}\mathrm{e}^{\mathrm{i}\mathbf{Q}\mathbf{L}t}\mathrm{i}\mathbf{A}\vec{u}_i\rangle \\ &= -\langle \mathrm{i}\mathbf{L}\mathbf{Q}\mathrm{i}\mathbf{B}\vec{u}_i \mathrm{e}^{\mathrm{i}\mathbf{Q}\mathbf{L}t}\mathrm{i}\mathbf{A}\vec{u}_i\rangle \\ &= -\langle \mathrm{i}\mathbf{L}\mathrm{i}\mathbf{B}\vec{u}_i \mathrm{e}^{\mathrm{i}\mathbf{Q}\mathbf{L}t}\mathrm{i}\mathbf{A}\vec{u}_i\rangle \\ &= -\langle \mathrm{i}\mathbf{L}\vec{F}_\mathrm{B}(0)\mathrm{e}^{\mathrm{i}\mathbf{Q}\mathbf{L}t}\mathrm{i}\mathbf{A}\vec{u}_i\rangle \\ &= -\langle (\nabla\vec{F}_\mathrm{B}\cdot\vec{u}_i)\mathrm{e}^{\mathrm{i}\mathbf{Q}\mathbf{L}t}\mathrm{i}\mathbf{A}\vec{u}_i\rangle \\ &= -\langle [\nabla\vec{F}_\mathrm{B}][\vec{u}_i \mathrm{e}^{\mathrm{i}\mathbf{Q}\mathbf{L}t}\mathrm{i}\mathbf{A}\vec{u}_i]\rangle,\end{aligned} \tag{B6}$$

where $\nabla\vec{F}_\mathrm{B}$ and $\vec{u}_i \mathrm{e}^{\mathrm{i}\mathbf{Q}\mathbf{L}t}\mathrm{i}\mathbf{A}\vec{u}_i$ are tensors.

Since $\vec{F}_{\mathrm{B}}$ depends only on the position of the particle of interest $\vec{r}_i$ and $\mathrm{i}\mathbf{A}\vec{u}_i$ only on $\vec{r}_j - \vec{r}_i$ ($j \neq i$), we can take the ensemble average by first integrating over the subspace $\Gamma_{\vec{r}_i} = (\vec{r}_1, \vec{r}_2, ..., \vec{r}_{i-1}, \vec{r}_{i+1}, ..., \vec{r}_N, \vec{p}_1, \vec{p}_2, ..., \vec{p}_N)$, then integrating over $\vec{r}_i$. We introduce the following abbreviation for simplicity:

$$\langle ab \rangle_{\vec{r}_i} = \int \mathrm{d}\Gamma_{\vec{r}_i} f_{\vec{r}_i}(\Gamma_{\vec{r}_i}) a(\Gamma_{\vec{r}_i}) b(\Gamma_{\vec{r}_i}), \tag{B7}$$

where $f_{\vec{r}_i}$ is the equilibrium distribution of the system when particle i is fixed at $\vec{r}_i$. Thus the time derivitive reforms as

$$\frac{\mathrm{d}}{\mathrm{d}t}\langle \vec{F}(0)\vec{R}(t)\rangle = -\int \vec{r}_i f(\vec{r}_i)[\vec{\nabla}\vec{F}_{\mathrm{B}}(\vec{r}_i)]\langle \vec{u}_i \mathrm{e}^{\mathrm{i}\mathbf{Q}\mathbf{L}t}\mathrm{i}\mathbf{A}\vec{u}_i\rangle_{\vec{r}_i}. \tag{B8}$$

If we define $\mathbf{P}_{\vec{r}_i}|...\rangle = \langle \vec{u}_i ... \rangle_{\vec{r}_i}\langle \vec{u}_i\vec{u}_i\rangle_{\vec{r}_i}^{-1}|\vec{u}_i\rangle_{\vec{r}_i}$, where $|\vec{u}_i\rangle_{\vec{r}_i}$ is the subspace of $|\vec{u}_i\rangle$ with $\vec{r}_i$ fixed, we will have $\langle \vec{u}_i \mathrm{e}^{\mathrm{i}\mathbf{Q}_{\vec{r}_i}\mathbf{L}t}\mathrm{i}\mathbf{A}\vec{u}_i\rangle_{\vec{r}_i} = 0$ where $\mathbf{Q}_{\vec{r}_i} = 1 - \mathbf{P}_{\vec{r}_i}$. This is because $\mathbf{P}_{\vec{r}_i}|\vec{u}_i\rangle_{\vec{r}_i} = |\vec{u}_i\rangle_{\vec{r}_i}$ and $\mathbf{Q}_{\vec{r}_i}|\vec{u}_i\rangle_{\vec{r}_i} = 0$. Due to the property of the operator $\mathbf{Q}_{\vec{r}_i}$, $\mathrm{e}^{\mathrm{i}\mathbf{Q}_{\vec{r}_i}\mathrm{i}\mathbf{L}t}$ will keep the vector it operates on to be orthogonal with $|\vec{u}_i\rangle_{\vec{r}_i}$ if the vector is orthogonal with $|\vec{u}_i\rangle_{\vec{r}_i}$ at time zero, which is true for $|\mathrm{i}\mathbf{A}\vec{u}_i\rangle_{\vec{r}_i}$. Since $\mathbf{P}_{\vec{r}_{i1}}|\vec{u}_i\rangle_{\vec{r}_{i2}} = \delta(\vec{r}_{i1} - \vec{r}_{i2})|\vec{u}_i\rangle_{\vec{r}_{i2}}$ and $\mathbf{P} = \sum_{\vec{r}_i}\mathbf{P}_{\vec{r}_i}$, we have $\mathbf{P}|\vec{u}_i\rangle_{\vec{r}_i} = |\vec{u}_i\rangle_{\vec{r}_i}$. Based on the projection property of $\mathbf{P}$ on $|\vec{u}_i\rangle_{\vec{r}_i}$, one gets $\langle \vec{u}_i \mathrm{e}^{\mathrm{i}\mathbf{Q}\mathbf{L}t}\mathrm{i}\mathbf{A}\vec{u}_i\rangle_{\vec{r}_i} = 0$, which means that $\langle \vec{F}(0)\vec{R}(t)\rangle$ would remain constant as t goes to infinity. As in the infinite time limit $\vec{F}(0)$ is not correlated with $\vec{R}(t)$, $\langle \vec{F}(0)\vec{R}(t)\rangle = \langle \vec{F}\rangle\langle \vec{R}\rangle$. At equilibrium, the net force $\langle F_x\rangle$ ($\langle R_x\rangle$) and $\langle F_y\rangle$ ($\langle R_y\rangle$) that are parallel to the solid wall vanish, but $\langle F_z\rangle$ ($\langle R_z\rangle$) in general does not. Therefore except $\langle F_z(0)R_z(t)\rangle$, all the elements of $\langle \vec{F}(0)\vec{R}(t)\rangle$ are zero. Due to spatial symmetry under reversals in x and y axes, one can show that $\langle R_x(0)R_z(t)\rangle = \langle R_z(0)R_x(t)\rangle = 0$ and $\langle R_y(0)R_z(t)\rangle = \langle R_z(0)R_y(t)\rangle = 0$. As a result, one can decouple the motion equation norm direction z from the one parallel to the wall.

In summary, rearranging Eq. B1 using the projection operator we defined, we finally have an equation with the form of extended GLE:

$$\begin{aligned}\dot{\vec{u}}_i(t) = -\frac{1}{kT}\int_0^t \vec{u}_i(t-t')\langle \mathrm{i}\mathbf{A}\vec{u}_i \mathrm{e}^{\mathrm{i}\mathbf{Q}\mathbf{L}t'}\mathrm{i}\mathbf{A}\vec{u}_i\rangle\,\mathrm{d}t' \\ +\mathrm{e}^{\mathrm{i}\mathbf{Q}\mathbf{L}t}\mathrm{i}\mathbf{A}\vec{u}_i + \mathrm{i}\mathbf{B}\vec{u}_i(t),\end{aligned} \tag{B9}$$

with the fluctuation-dissipation relation generalized to be

$$kT\boldsymbol{\gamma}(t) = \langle \mathrm{i}\mathbf{A}\vec{u}_i \mathrm{e}^{\mathrm{i}\mathbf{Q}\mathbf{L}t}\mathrm{i}\mathbf{A}\vec{u}_i\rangle = \langle \vec{R}(0)\vec{R}(t)\rangle, \tag{B10}$$

and Eqs. 4.14, 4.15 generalized to be

$$\langle \vec{u}_i(0)\vec{R}_i(t)\rangle = \langle \vec{F}_i(0)\vec{R}_i(t)\rangle = 0,\ t > 0. \tag{B11}$$

One should be aware that the vectors and tensors in Eqs. B9, B10, B11 are two dimensional and parallel to the solid wall.

Appendix C: Fittings of the near-boundary long-time tails

In Chapter 5, we stated that in the long-time limit the velocity autocorrelation function (VAF) of near-boundary nano-particle decays with time t as $t^{-5/2}$ rather than $t^{-3/2}$. Here, we provide data to support this conclusion. Specifically, we fit the VAF long-time tails of the particles with a power-law function: $y = ax^b$. The fittings are presented in Figure C1 and the results are summarized in Table C1. The $t^{-5/2}$ decay fits the data better than the $t^{-3/2}$. Although physical models all predict an algebraic decay of the VAF, one can ask if an exponential fit would fit our data. Therefore, in addition we have fitted our data to exponential decays with two free fitting parameters (amplitude and relaxation time). As shown in Table C1, the qualities of these fits (quantified via R^2 values) lie between those for $t^{-3/2}$ and $t^{-5/2}$ and Figure C1 shows that exponential decays underestimate the VAFs at long time scales.

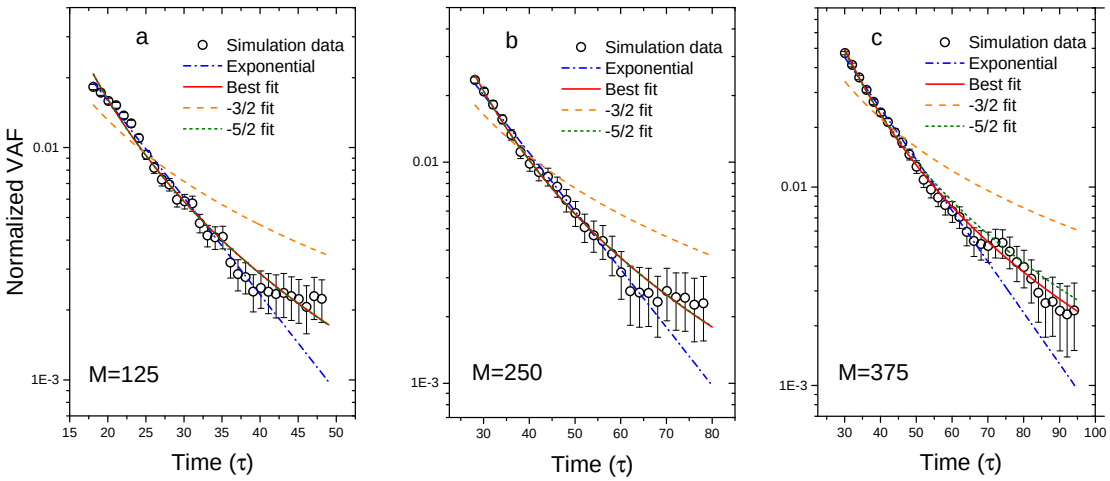

Figure C1: Fittings of the asymptotic behavior of the VAF of near-boundary nano-particles. From the left to the right: the mass of the particle M=125, 250 and 375 in reduced units. See Table S1 for parameters of the fits.

Table C1: Fitting results of the asymptotic behavior of near-boundary VAFs. The long-time tails of VAF are fitted to power law function $y = ax^b$. R^2 represents the quality of the fit. Exponential decay with two free fitting parameters can fit the data relatively well but the performance is not as good as for the $t^{-5/2}$ decay, which almost overlaps with the best power law fit.

Mass	Fit with b=-5/2	Fit with b=-3/2	Best fit	Exponential
125	$R^2 = 0.980$	$R^2 = 0.835$	$b = -2.49$, $R^2 = 0.980$	$R^2 = 0.976$
250	$R^2 = 0.996$	$R^2 = 0.849$	$b = -2.51$, $R^2 = 0.996$	$R^2 = 0.986$
375	$R^2 = 0.996$	$R^2 = 0.826$	$b = -2.64$, $R^2 = 0.996$	$R^2 = 0.990$

Appendix D: Supporting information for specific ion effects

Water density and its fluctuation in the hydrophobic hydration shell

We calculate the radial distribution function (RDF) and its fluctuation over time for hydrophobic group-water oxygen pairs. RDF is calculated in spherical bins (shells) with a width of 0.1 nm. We find that the bin width of 0.1 nm provides a balance between a relatively good spatial resolution of the hydration structure and a meaningful measure of the hydration dynamics over time. For a bin size that is too small to accommodate more than one water oxygen at the same time, the mean fluctuation of the density tends to lose the dynamic information. In fact, one can show that when the number of particles n in the bin at any time is either 0 or 1, the magnitude of the fluctuation Δn becomes determined by $\bar{n}(1-\bar{n})$, where $\bar{n}$ is the time averaged particle number in the bin. Therefore in the limit of small bins, a measurement of the magnitude of fluctuation is simply equivalent to a measurement of the time-averaged density or RDF. The fluctuations of the RDFs in various solutions are plotted in Fig. D1(b). Compared to the RDFs, the RDF fluctuations are more sensitive to the identities of free ions. The RDF fluctuation in NaCl is quite similar to the one in pure water, consistently with the location of NaCl at the border between kosmotropic and chaotropic salts. For large ions (I^- and Cs^+), RDF fluctuation is enhanced as compared to the case of pure water. On the other hand, small F^- is found to reduce the fluctuation of hydrophobic hydration. In addition, it is interesting to note that the irregular behavior of Li^+ is reflected in its effect on the RDF fluctuation as Li^+ occupies a position between Na^+ and Cs^+, analogous to its position in the Hofmester order for salting-out non-polar solutes. Therefore we find the water fluctuation in the hydrophobic hydration shell to be a good indicator of the specific free ion effect.

Proximally immobilized ion effects in constrained simulation

In the main text we mentioned that if nano-rods are constrained in such a way that the proximal charges are always pointing away from the hydrophobic surface, then the modulation of hydrophobic interactions by ions follows the same order as in unconstrained simulations. This is demonstrated in Fig. D2. It is worth pointing out that with the constraint, the contact minimum is in general systematically deeper than in the unconstrained system. It is because the reference state (corresponding to nano-rod being far away from the wall) is different for the two systems: the constrained nano-rod remains oriented normal to the wall after it is

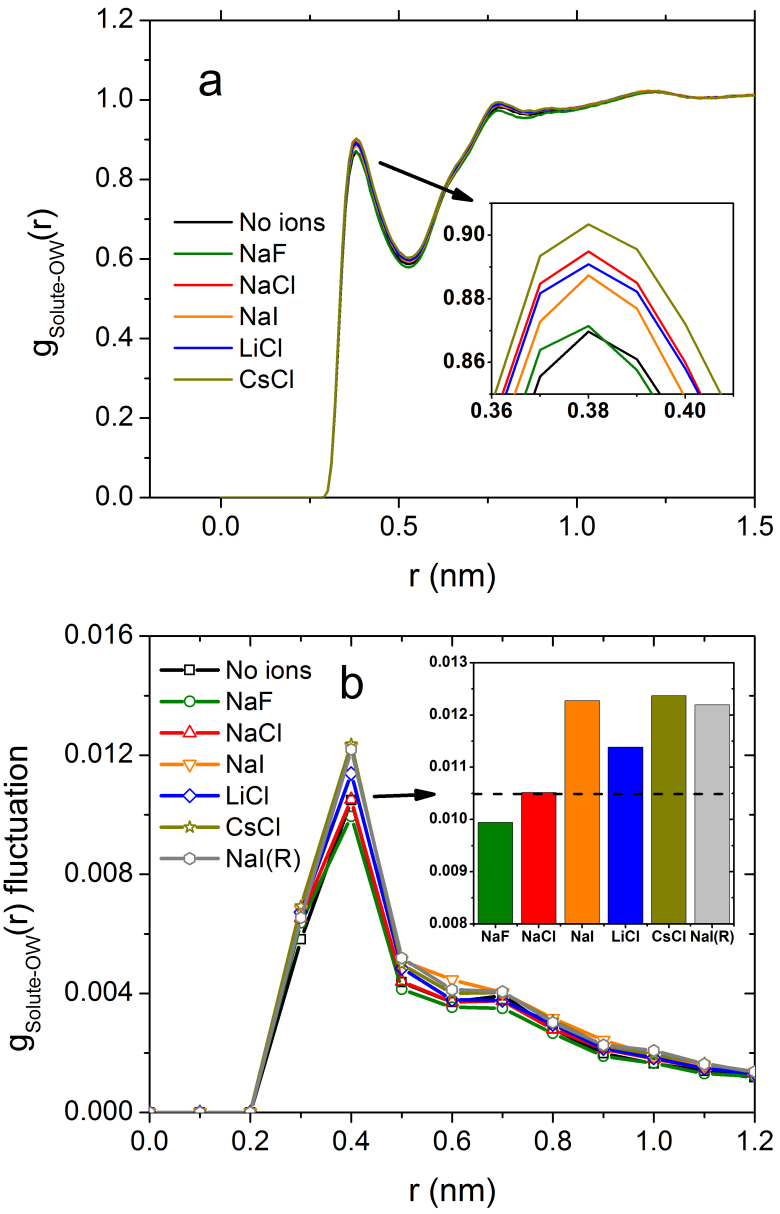

Figure D1: water density and its fluctuation. (a) Radial distribution function (RDF) for water oxygen around nano-rod. (b) Fluctuation in RDF for water oxygen around nano-rod. One should note that when calculating RDF, we keep the width of the spherical bin constant and therefore the number of atoms in each bin will increase with distance r. This issue has been accounted for in calculations of RDF by normalizing the data. However, RDF fluctuations will still be larger for bins corresponding to smaller values of r (because they contain fewer particles) and the large RDF fluctuation at $r = 0.4$ nm is the result of the small bin size. The important feature in the figure is the difference in the fluctuation for different types of ions.

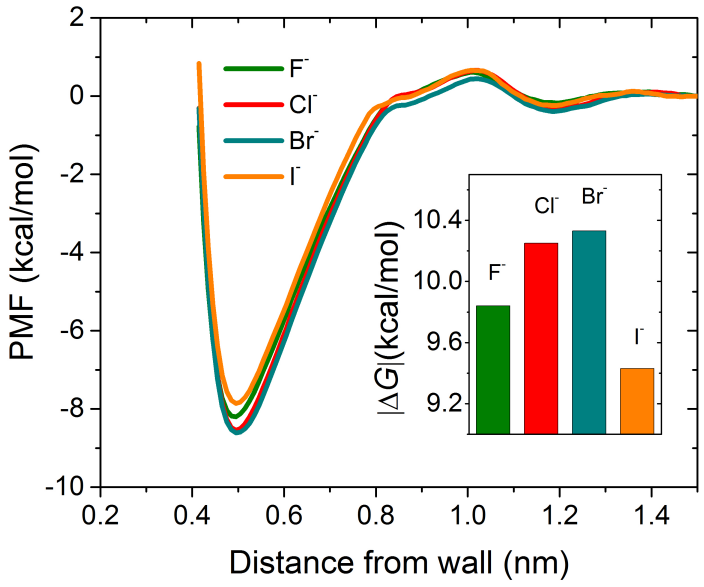

Figure D2: PMF of hydrophobic interaction between a hydrophobic wall and GA nano-rod under constraint. The inset shows the contact minimum depth, which is defined as the absolute value of the difference in PMF between the contact minimum and the reference state where the nano-rod and the surface are separated from each other.

completely detached whereas the unconstrained molecule can explore more orientations, which increases the entropy.

Anomaly of the lithium effect

To determine the primary mechanism responsible for the lithium anomaly, we carried out simulations of LiCl salt solution with a constraint on lithium cations such that Li^+ cannot form clusters with chloride anions. This lack of clustering is evidenced by RDF plotted in Fig D3(a). Figure D3b shows that with the full ionic hydration shell the salting-out effect of lithium becomes slightly stronger than in the case where lithium is allowed to cluster. However, the salting-out effect of dissociated lithium (LiCl(R)) is still weaker than that of sodium (Fig. D3b), and significantly weaker than that of fluoride. The structure of the PMF from the constrained simulation (not shown here) looks very similar to one without constraint. The RDF fluctuation is also hardly changed by the constraint, as shown in Fig D3c. Surprisingly, the depletion of fully hydrated lithium from nano-rod is even weaker than that of clustered lithium (Fig D3d). Such a weak depletion resembles the behavior of the large iodide. Consequently, our control simulation with a constraint suggests that while the clustering can contribute to the anomaly of lithium, the primary reason for this anomaly is the large effective size of this ion. Here, the

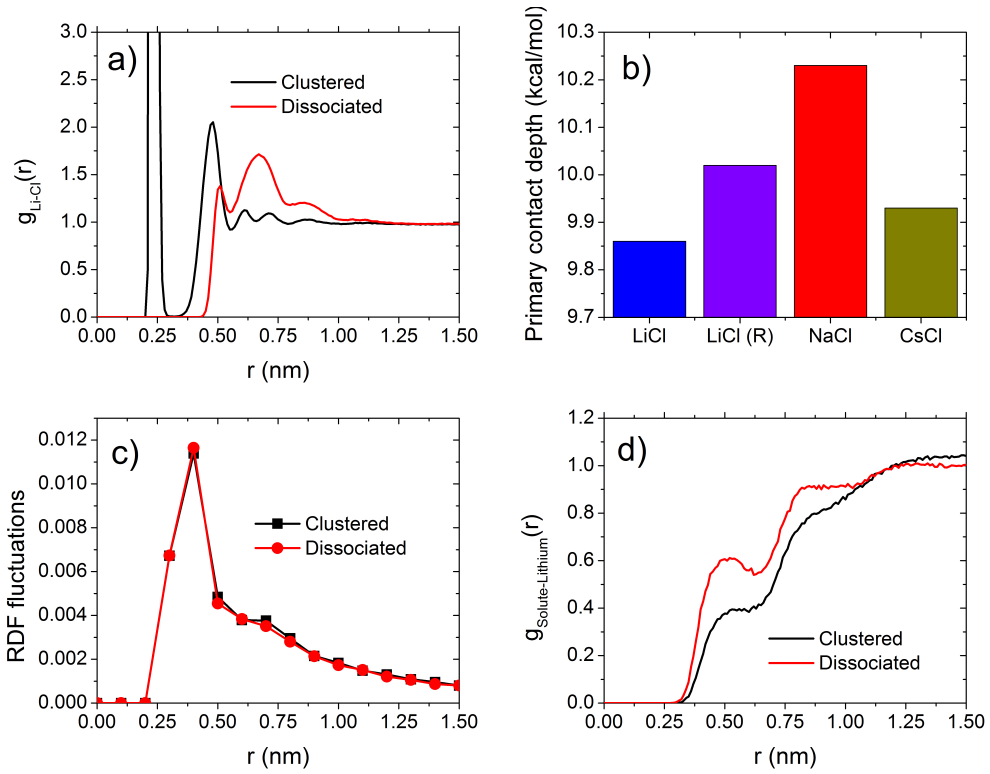

Figure D3: Anomalous lithium effects. (a) RDF for LiCl RDFs. (b) PMF for hydrophobic interaction. LiCl(R) means LiCl where constraints have been added to ensure a complete dissociation of ions. (c) RDF fluctuation for peptide-water oxygen interactions. (d) RDF for peptide-Li interactions.

effective size is large not only because of a strong first hydration shell, but also because of a labile second hydration shell which accelerates the reorientation of water, similarly as has been observed for large ions.